Scene Analysis and Interpretation by ICA Based Polarimetric Incoherent Target Decomposition for Polarimetric SAR Data

Leandro Guimaraes Figueroa Pralon

Communauté
UNIVERSITÉ Grenoble Alpes

THÉSE

pour obtenir le grade de

DOCTEUR DE DE LA COMMUNAUTÉ UNIVERSITÉ GRENOBLE ALPES

Spécialité : **Signal, Image, Parole, Télécoms**

Arrêté ministériel : 07 août 2006

Présentée par
Leandro Guimaraes Figueroa Pralon

Thèse dirigée par **Jocelyn CHANUSSOT**, **Gabriel VASILE** et **Mauro DALLA MURA**

préparée au sein du
Grenoble Image Parole Signal Automatique laboratoire (GIPSA-lab)
dans **l'école doctorale Electronique, Electrotechnique, Automatique, Traitement du Signal (EEATS)**

Scene Analysis and Interpretation by ICA Based Polarimetric Incoherent Target Decomposition for Polarimetric SAR Data

Thèse soutenue publiquement le **27 octobre 2016**,
devant le jury composé de:

Mme. Florence Tupin
Professeur, Telecom ParisTech, Examinateur, Présidente du jury
Mme. Marie Chabert
Professeur, National Polytechnic Institute of Toulouse, Rapporteur
M. Alejandro Frery
Professeur, Federal University of Alagoas, Rapporteur
M. Jocelyn CHANUSSOT
Professeur, Grenoble INP, Directeur de thèse
M. Gabriel VASILE
Chargé de recherche, CNRS, Encadrant de thèse
M. Mauro DALLA MURA
Maître de conférences, Grenoble INP, Encadrant de thèse

COMMUNAUTÉ UNIVERSITY OF GRENOBLE ALPES

Doctoral School EEATS

Doctoral School for Electronics, Power Systems, Automatic Control and Signal Processing

T H E S I S

for obtaining the

Doctorate Degree

of Communauté University of Grenoble Alpes

Speciality: Signal, Image, Speech, Telecommunications

Presented and defended by

Leandro Guimaraes Figueroa PRALON

Scene Analysis and Interpretation by ICA Based Polarimetric Incoherent Target Decomposition for Polarimetric SAR Data

Thesis supervised by Jocely CHANUSSOT, Gabriel VASILE and Mauro DALLA MURA

Prepared in the Grenoble Image Parole Signal Automatique laboratory (GIPSA-lab)

Defended in Grenoble, on 27th October 2016

Jury :

Supervisors :	Gabriel VASILE	-	Research Scientist, CNRS
	Mauro DALLAMURA	-	Maître de conférences, Grenoble INP
Directeur :	Jocelyn CHANUSSOT	-	Professor, Grenoble INP
President :	Florence Tupin	-	Professor, Telecom ParisTech
Examiners :	Alejandro Frery	-	Professor, Federal University of Alagoas
	Marie Chabert	-	Professor, National Polytechnic Institute of Toulouse

"There are no facts, only interpretation."
by Friedrich Nietzsche

Remerciements

This thesis was conducted entirely on the Grenoble-Image-sPeech-Signal-Automatics Laboratory (GIPSA-lab, Grenoble INP) and funded by the Brazilian Army.

First of all I would like to express my most sincere gratitude to my thesis directors Prof. Gabriel Vasile, Prof. Mauro Dalla-Mura and Prof. Jocelyn Chanussot for their support, guidance, patience and most important, for their technical advice provided unrestrictedly in the last three years.

I want to thank Prof. Marie Chabert and Prof. Alejandro Frery for agreeing to be reviewers of my thesis. Special thanks to Prof. Florence Tupin for accepting to preside the jury.

I would also like to thank the French Aerospace Lab (ONERA) and the German Aerospace Center (DLR-HR) for providing the high resolution POLSAR images used throughout this thesis.

A special thanks to my colleagues in the Brazilian Army who believed in me and made this work possible.

To the love of my life, my wife Barbara, for so many reasons that would be impossible to enumerate in a finite number of pages. My tenderest gratitude for walking beside me throughout this journey.

To my dear son Murilo, for unknowingly serving both as a constant inspiration as well as an unlimited source of inner peace, being the main reason for me to want to succeed.

To my parents and sister, for always being there for me, helping me in every moment I needed.

I would also like to thank all the members of GIPSA-lab for the nice atmosphere in which I was lucky to work.

Finally, I would like to thank God for placing all these people in my life.

Contents

List of Figures

List of Tables

Abbreviations and acronyms

SAR	*Synthetic Aperture Radar*
PRI	*Pulse Repetition Interval*
RF	*Radio Frequency*
SLC	*Single Look Complex*
PolSAR	*Polarimetric Synthetic Aperture Radar*
ICTD	*Incoherent Target Decomposition*
BSA	*Backscatter Alignment*
PolInSAR	*Polarimetric Interferometric Synthetic Aperture Radar*
SCM	*Sampled Covariance Matrix*
ICA	*Independent Component Analysis*
BSS	*Blind Source Separation*
PCA	*Principal Component Analysis*
SIRV	*Spherically Invariant Random Vector*
FP	*Fixed Point*
CES	*Complex Elliptically Symmetric Distributions*
CN	*Complex Normal Distribution*
TSVM	*Target Scattering Vector Model*

Chapter 1

Introduction

Remote sensing systems provide an unique way to perform large scale and non-intrusive observations of the Earth's surface [87, 34, 33]. Since its conception in the late 60s, the number of applications that benefit from the information acquired by such sensors have grown rapidly. Among many, it is possible to highlight the urban settlement analysis, environment and crops monitoring, damage assessment, biomass estimation and general surveillance related applications.

Optical systems and Synthetic Aperture Radars (SARs) have been sharing the spotlights of the research community when it comes to the most employed sensors for such purpose [87]. In general, optical imagery senses the reflectance of the Earth's surface on the visible and near infrared ranges of the electromagnetic spectrum [33]. Conversely, SAR sensors are active systems that characterize the surface by detecting the backscattering of electromagnetic pulses sent by the platform towards the former [34].

Optical and SAR images present completely different features due to distinct sensing geometry, way of acquisition and sensed physical characteristics of the surface. Typically, optical images present a better spatial and spectral resolution. SAR data on the other hand are independent on the weather condition (they can also be acquired in nighttime), depending on the operating frequency they can penetrate vegetation canopies and they allow unique analysis such as the estimation of the surface 3D geometry through interferometry [33]. Unlike optical images, which are construed in a straightforward manner, the correct interpretation of a SAR image is still an open challenge to the scientific community from both a methodological as well as an applicative perspective. Specific methods are still required to enhance the characterization of objects in the scene, land cover types, monitoring surface parameters and, in general, extracting information on the surveyed areas.

Polarimetric systems emerged as an attempt to fill this gap. Polarimetry theory relies on the analysis of the interaction between the illuminated area and the transmitted waveform, considering each polarimetric state of the latter. Compared to the univariate analysis of single polarization systems, the multivariate nature of Polarimetric SAR (PolSAR) data allows for a better prediction of the physical properties of the illuminated targets, leading to more effective classification, detection and geophysical parameter inversion algorithms. One of the most employed techniques for PolSAR image interpretation is the Polarimetric Target Decomposition, that enables the description of an image cell as a sum of canonical scattering mechanisms, making it more intuitive to understand the behaviour of the clutter and therefore

to analyse it [98].

There are key aspects that underpin effective PolSAR target decomposition techniques. Stochastic clutter modelling, in case of distributed targets (e.g. vegetation, forests and snow) and the correct retrieval of quantitative information from the estimated scattering mechanisms (parametrization) are examples of such topics that directly influence the performance of applied algorithms.

When distributed targets are under investigation, special care has to be taken. Unlike deterministic ones such as man made structures, the study of distributed targets is more challenging, requiring an analysis usually based on the stochastic properties of the SAR data. In general, when low-resolution multivariate SAR data is under investigation, the central limit theorem is taken into consideration and the data can be locally modelled by a multivariate zero-mean circular Gaussian stochastic process, which is completely determined by its covariance matrix. With the improved resolution of modern SAR platforms, the number of scatters within each resolution cell decreases considerably. Consequently, high scene heterogeneity may eventually lead to non-Gaussian clutter modelling.

Spherically Invariant Random Vectors (SIRVs) [107], have been frequently employed for modelling high-resolution PolSAR data [104, 7, 41, 105]. SIRV is a multiplicative model that expresses the SAR signal as a product between the square root of a scalar positive quantity (texture) and the description of an equivalent homogeneous surface (speckle) [102]. It is important to notice that in the SIRV definition, the texture probability density function is not explicitly specified. As a consequence, SIRVs describe a whole class of stochastic processes [85], including the Gaussian (multivariate) model (deterministic texture), KummerU distribution (Fisher texture) [7], the multivariate $\mathcal{K}$ distribution (Gamma texture) [74] and the $\mathcal{G}^0$ distribution (inverse Gamma texture) [73], the last two being special cases of the more general multivariate $\mathcal{G}$-family, specially suited for extremely heterogeneous clutters [44, 43].

The estimated covariance matrix of the speckle is the basis of many PolSAR classification algorithms [18]. Usually, optimal solutions rely on maximum likelihood estimators, which are highly dependent on the model adopted [76]. The assumption that the texture is polarization independent causes PolSAR data to present a spherical symmetry property, allowing for the usage of most of the algorithms present in the literature. Nevertheless, the existence of polarization dependant clutter has also been reported [35, 97], for which specific algorithms need to be derived. Therefore, it becomes clear that the first step in SAR data analysis should be the validation of the model employed. Within this context, in Chapter 3 we present a new methodological framework to assess the conformity of multivariate high-resolution SAR data with respect to the product model in terms of asymptotic statistics. More precisely, spherical symmetry is investigated by applying statistical hypotheses testing on the structure of the quadricovariance matrix.

The analysis with real data shows that a considerable portion of high heterogeneous data may not fit the Spherically Invariant Random Vector model (product model). Therefore, traditional detection and classification algorithms developed based on the latter become suboptimal when applied in such kind of regions. This assertion highlights for the need of either

updating the model to one that associates an individual texture variable with each polarimetric channel [35], or the development of model independent algorithms, like the Independent Component Analysis (ICA), proposed in [3].

The referred method is briefly summarised in three main steps: data selection, based on the statistical classification of the POLSAR image; estimation of independent components and parametrization of the derived target vectors. As stated in [3], the major drawback of the proposed method is the size of the observation dataset, which has to be somewhat larger than the size of the sliding window used in the well established methods. This constraint led the authors in [3] to use an unsupervised classification algorithm rather than relying on a very large sliding window, jeopardising the effectiveness of the method.

The use of a classification algorithm limits the performance of the method in the sense that the image is segmented in a priori defined number of classes with variable sizes, what can compromise the estimation of the target vectors parameters and, as a consequence, the correct interpretation of the scatters present in the area under study. One of the implications of the employment of a classification algorithm is that a class can contain more samples than it needs for a correct estimation of target's parameters, meaning that spatial resolution, highly degraded with the use of this approach, is worse than it could be. On the other hand, if a class does not contain enough samples, the estimation performed using this given set of pixels can be biased, i.e., the estimated parameters present a bias, either positive or negative, that drives the derived values away from the ground truth.

An additional drawback inherent to ICA described in the literature, that could limit its usage in PolSAR application, is the central principle of non-gaussianity of the sources that has to be assumed in the model [48]. Even though heterogeneous clutter models like [104] have gained notoriety, one single Gaussian source could jeopardise the performance of ICA, making its use inappropriate. Recent studies [37] proved that, under certain conditions, Gaussian sources can indeed be separable, indicating that the usage of ICA in PolSAR data analysis can occur in a larger number of scenarios.

Within this context, another contribution of the present work is a detailed analysis (described in Chapter 5) based on a Monte Carlo simulation approach to evaluate the aforementioned theoretical aspects of ICA based ICTD. The optimal size of a sliding window for various medias, simple ones composed by basic scatters such as helix, dipole, dihedral and trihedral and more complex ones like Surface, Double Bounce and Volume returns is addressed. The performance of the algorithm in the presence of Gaussian sources is also investigated, as well as in the assumption of scenarios that present spatial correlation, increasing the range of potential applications to this technique.

The final aspect of this thesis is the analysis of the potential new information provided by the ICA based ICTD. For that purpose, we take into consideration both Touzi Target Vector Scattering Model (TSVM) as well as Cloude and Pottier H/α feature space, two of the most employed methods for unsupervised PolSAR data classification based on Incoherent Target Decomposition. The combined use of ICA and Touzi TSVM is straightforward, indicating new, but not groundbreaking information, when compared to the Eigenvector approach. Nev-

ertheless, the analysis of the combined use of ICA and Cloude and Pottier H/α feature space revealed a potential aspect of the Independent Component Analysis based ICTD, which can not be matched by the Eigenvector approach.

The aforementioned parameterization method can be split in two stages, the retrieval of the canonical scattering mechanisms present in an image cell and their parameterization. The association of the coherence matrix eigenvectors to the most dominant scatters in the analysed pixel introduces unfeasible regions in the H/α plane. This constraint can compromise the performance of detection, classification and geophysical parameters inversion algorithms that are based on the investigation of this feature space. Not constrained to any orthogonality between the estimated scattering mechanisms that compose the clutter under analysis, ICA does not introduce any unfeasible region in the H/α plane, increasing the range of possible natural phenomena depicted in the aforementioned feature space. A detailed investigation of the characteristics of pixels that may fall outside the feasible regions in the H/α plane that arise when the Eigenvector approach is employed is performed in Chapter 4.

This thesis is organised as follows. In Chapter 2 we revisit Synthetic Aperture Radar principles, addressing its geometry of acquisition, basic image formation concepts, spatial resolution and the importance of the proper choice of system parameters. Still in Chapter 2, we introduce concepts related to the multivariate analysis of SAR datasets resultant from multiple acquisitions. Interferometry concepts used to retrieve the vertical profile of the scene under study as well as the polarimetric state of electromagnetic waveforms and how this feature can be explored to enhance SAR data interpretation are approached. In Chapter 3 we address the stochastic assessment of the clutter model. For that purpose, we introduce the SIRV stochastic model [104], highlighting the main differences with respect to the multivariate Gaussian model. Next, we detail the proposed method for quantitative assessment of the SIRV conformity, which relies on the spherical symmetry test of the multivariate PolSAR data and we verify its consistency from different aspects, including synthetic and real data analysis.

Chapter 4 addresses in more details Incoherent Target decompositions, reviewing both Touzi Target Scattering Vector Model (TSVM) as well as Cloude and Pottier decomposition (and consequently the H/α feature space), highlighting the constraint inherent to its combined use with the Eigenvector approach. Also in this chapter the Independent Component Analysis proposed in [3] as an ICTD method is presented. Chapter 5 addresses theoretical aspects of the ICA based ICTD approach, including its performance under a sliding window implementation and a discussion regarding its employment in Gaussian clutter scenarios and scenarios that exhibit spatial correlation. Taking into account the SIRV model addressed previously, a Monte Carlo simulation approach is conducted in order to evaluate its performance under a sliding window approach, enabling a more accurate comparison to the results obtained with the widespread Eigenvector based approach. Clutters composed by orthogonal and non-orthogonal scattering mechanisms are taken into consideration, evidencing the new information brought about the proposed technique.

In Chapter 6 practical aspects of the employment of the ICA as an ICTD technique are analysed. A detailed investigation of the characteristics presented by pixels classified by the ICA based ICTD outside the feasible regions of the H/α feature space that arise upon the

employment of the Eigenvector approach is performed. The new information brought about ICA based ICTD in tropical scenarios is also discussed, as well as its potential employment in PolInSAR experiments. Finally, Chapter 7 presents some general remarks regarding the proposed methodological framework for the clutter stochastic assessment and ICA based ICTD, as well as some conclusions and future works perspectives.

Throughout the present work, data from the P-band airborne dataset acquired by the Office National dÉtudes et de Recherches Aérospatiales (ONERA) over the French Guiana in 2009 in the frame of the European Space Agency campaign TropiSAR, a RAMSES X-band image acquired over Brétigny, France and a PolSAR dataset acquired in October 2006 by the E-SAR system over the upper part of the Tacul glacier from the "Chamonix - Mont Blanc" test site are taken into consideration in several analysis. Details on the referred data sets are presented in Appendix E.

Chapter 2

Synthetic Aperture Radar

Sommaire

Radars are electromagnetic systems originally conceived for detecting and estimating the radial distance of a reflecting object. Its basic principle consisted on the transmission of a waveform and the measurement of the time delay until the reception of the signal reflected on a given scatter. The advances in the fields of electronics during the last few decades considerably increased the range of applications where such kind of systems can be employed.

Several features of the illuminated targets/scene can now be derived based on the proper choice of the system parameters and the correct interpretation of the returned signal. This assertion is somehow intuitive, since each object on the Earth's surface scatters an incident electromagnetic wave in a unique fashion, generally as a function of its shape and composition. Therefore, changing the properties of the transmit waveform as well as the angle of illumination, directly affects the backscattered energy and the perception of the targets on the scene.

There are several different architectures of radar systems, each specially suited for a specific application. They are often classified either by their final purpose (e.g. meteorological, surveillance, remote sensing) or by the choice of their parameters (e.g. central frequency band, transmit waveform, bandwidth, antenna characteristics). The latter in turn, is directly related to the system performance. As an example, it is possible to highlight that the transmitted signal central frequency impacts directly the atmospheric transmittance[1], the penetration through vegetation, and the antenna size.

[1] Even though atmospheric effects are more critical for high frequency electromagnetic waves, the ionosphere can induce undesired behaviour (i.e. Faraday rotation) for frequencies lower than 1GHz [87].

In the present work, the focus relies on remote sensing radars, more precisely, imaging radars that sense the Earth's surface. Imaging radar research can be broadly divided in two areas: image formation and image interpretation. Image formation theory comprises the design of the system physical architecture, the proper choice of parameters, the transmission, the reception and specific signal processing algorithms target, for example, to correct phenomena related to the systems geometry or to enhance the system spatial resolution. Image interpretation, on the other hand is basically focused on better understanding the illuminated area on the ground, extracting both qualitative as well as quantitative information from it, that can lead to better detection and classification schemes of the objects and physical phenomena in the scene under study. In the present work, the main interest lies in enhancing Synthetic Aperture Radar image interpretation. Nevertheless, for the sake of completeness we briefly address a few SAR image formation concepts, that will be referenced throughout this thesis.

2.1 SAR basic principles

Generally, in remote sensing the area under analysis is large, inhibiting the usage of fixed antenna configurations for such kind of applications. Therefore, side looking antennas are embedded on a moving platform (airplane, satellite, UAV), producing large scale 2D images of areas on the ground with a considerable high spatial resolution, as illustrated in Figure 2.1. This architecture is referred in the literature to synthetic aperture radar (SAR), whose name will become clear later on this section, but for simplicity the nomenclature is already adopted henceforth.

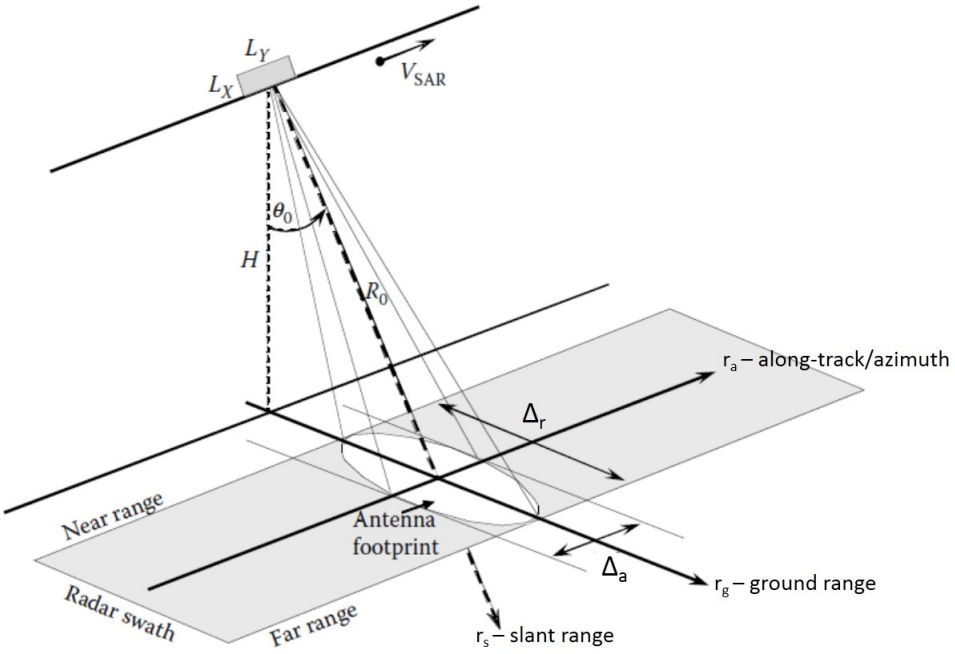

Figure 2.1: Synthetic Aperture Radar strip map geometry (modified from [57]).

In Figure 2.1, v_{sar} represents the platform velocity, H its height, θ_0 the illumination angle and L_x and L_y the antenna dimensions. The coordinate axes are represented by r_a, which is the along-track or azimuthal direction (as a heritage of classical rotational radar systems), r_g which is the ground range and r_s that represents the slant range direction, i.e. the radar line of sight. As the platform moves, the entire region indicated as the Radar swath is sensed.

Generally, SAR systems are pulsed monostatic systems, i.e. a single antenna is used for transmission and reception of time limited signals spaced in time by a pulse repetition period (PRI). Furthermore, it is a coherent system, i.e. the signal's phase is preserved throughout the RF and signal processing chain.

The image formation process starts by associating to each point on the illuminated surface a specific information. Note that, according to the system geometry presented in Figure 2.1[2], the transmit waveform, being a planar wavefront (see Section 2.2.1) hits each point on the surface at a different time. Therefore, it is possible to associate to each point P on the surface a given received signal corresponding to its backscatter.

One of the relevant information that can be extracted from the received signal is its mean power. Being a function of both the system parameters as well as the surface's, it can reveal much of the targets characteristics. The mean power of the signal received by the antenna, P_r, relative to the backscatter of a given point on the surface (henceforth also addressed as a target) located at a distance R_0 from the radar (in slant range direction) is given by the so called radar equation [91], and is written as

$$P_r = \frac{P_t G_t G_r \sigma \lambda}{(4\pi)^3 R_0^4} \tag{2.1}$$

where σ is the target radar cross section which represents a mean measure of how much of the incident energy it backscattered to the radar, P_t is the mean power of the transmitted signal, G_t and G_r are the transmit and receive antenna gain, respectively, and λ is the transmitted signal wavelength.

Aside from the target radar cross section, all parameters in (2.1) are somehow under the radar designer control. Therefore, manipulating them, can lead to more effective detection algorithms, since it will directly affect the signal to noise ratio throughout the processing chain. Note that (2.1) represents the received signal power, therefore, the system losses and processing gains are not taken into consideration. Furthermore, it can be considered extremely optimist since it does not account for the stochastic nature of its parameters, specially the target radar cross section.

Another information of interest to most SAR applications is the received signal's phase. In order to exploit this parameter, its a common practise to extract the received signal complex envelope (through a Hilbert transform [45]) and perform all signal processing algorithms (image formation and image interpretation) considering the latter. Let us now briefly address

[2]The geometry is a key factor in SAR systems, and it is directly related to the final application. Even though other geometries are also feasible under the Synthetic Aperture Radar concept, throughout this work, only the Strip map configuration is addressed.

the mathematical model of the involved signals.

Assume that $\tilde{s}_i(t), 0 < t < \tau_s$ is the complex envelope (with respect to a given reference frequency) of the time limited signal emitted by the radar at the beginning of the ith interval, $(i\Delta, (i+1)\Delta]$, with t denoting time with respect to the beginning of the interval, and Δ is the Pulse Repetition Interval. The complex envelope of the received signal, during the ith interval, corresponding to the backscatter of each point on the surface can be written as

$$\tilde{r}_i(t) = \tilde{x}_i(t) + \tilde{n}_i(t) \tag{2.2}$$

where $\tilde{n}_i(t)$ corresponds to the filtered complex envelope of the corrupting thermal noise inherent to the receiver, assumed to be Gaussian with zero mean and a flat power spectral density over the signal component bandwidth and $\tilde{x}_i(t)$ denotes the complex envelope of the signal component, given by

$$\tilde{x}_i(t) = A_i e^{\frac{-4\pi R_0}{\lambda}} e^{\phi_r} \tilde{s}_i(t - T_0) \tag{2.3}$$

with A_i being an amplitude that reflects channel fading and the gains and distortions introduced by the receiver RF chain (assumed to be constant during the ith interval with no loss of generality), T_0 being the time spent by the emitted signal to echo on a given point on the surface and return to the radar, which is given by $T_0 = 2R_0/c$, with c being the vacuum light speed and ϕ_r representing a possible phase rotation introduced by specific type of scatters.

At this moment it is relevant to introduce the range resolution concept. Range resolution describes the radar ability in disguising the scatters of two points on the surface close to each other in range. If the transmitted signal duration is τ_s, then it spreads in space by a distance $R_{\tau_s} = c\tau_s$. Therefore, two points could only be interpreted as such, i.e., without being mistaken as a single point on the surface (due to their backscatter overlap) when separated by a distance equal to or greater than $\Delta R_{\tau_s} = \frac{R_{\tau_s}}{2} = \frac{c\tau_s}{2}$.

Equipments capable of generating short pulses with high energy (necessary to enhance system performance, see (2.1)) are difficult to achieve [57], constraining the transmission of long pulses. Therefore, in order to enhance range resolution, without compromising system's performance, the pulse compression technique is generally employed. Pulse compression at the receiver is implemented by a matched filter [91] (matched to the transmitted signal), having an impulse response (low-pass equivalent) $\tilde{h}_i(t) = \tilde{s}_i^*(-t)$. There are several works in radar literature that evaluate the performance of different filters with respect to varied aspects [15]. The matched filter is often preferred over the others because it maximises the signal to noise ratio at its output, enhancing detection. The output $\tilde{y}_i'(t)$ of this filter is written as

$$\tilde{y}_i'(t) = \tilde{x}_i'(t) + \tilde{n}_i'(t) \tag{2.4}$$

where

$$\tilde{x}_i'(t) = \int_0^{T_{int}} A_i e^{\frac{-4\pi R_0}{\lambda}} e^{\phi_r} \tilde{s}_i(\tau + t - T_0)\tilde{s}_i^*(\tau)d\tau \tag{2.5}$$

$$\tilde{n}_i'(t) = \int_0^{T_{int}} \tilde{n}_i(\tau + t)\tilde{s}_i^*(\tau)d\tau \tag{2.6}$$

with T_{int} being the upper limit of the convolution integration, referred to as "integration time" ($T_{int} \leq \tau_s$). T_{int} is an intrinsic parameter of the pulse compression process. In remote sensing applications, where the targets are located outside the blind zone and the entire returned signal is received, $T_{int} = \tau_s$.

The signal to noise ratio at the matched filter output is given by

$$SNR'_i(T_0) = \frac{E_{\tilde{x}_i}}{N_0} \tag{2.7}$$

where $E_{\tilde{x}_i}$ is the signal component energy and N_0 is the noise power spectral level at the input of the matched filter. Finally, the pulse compression gain is given by $G_c = B_{\tilde{s}}\tau_s$, where $B_{\tilde{s}}$ is the bandwidth of the transmitted signal complex envelope. The aforementioned gain is also referred to, within the radar community, as the time-bandwidth product.

It is counter-intuitive to name this operation as "pulse compression" since the output signal $\tilde{y}'_i(t)$ has twice the size of the input signal. Nevertheless, the signal's energy is concentrated in a smaller time interval, increasing the ability of radars that employ such technique to discriminate between two targets located close to each other. In such systems, the range resolution is then derived considering τ_s equal to the 3dB width in time, τ_{3dB}, of the matched filter output. This parameter is an intrinsic property of the transmit waveform. Likewise the filter design, many works have been published in the literature proposing different waveforms in order to improve the range resolution [79]. Nevertheless, linear frequency modulation have been employed more than any other in radar applications [91][3], being the most widespread signal generation method in radar community.

Carriers modulated in frequency are generically given by

$$s(t) = \sqrt{2P_s}\cos(2\pi f_c t + K_p \int_{-\infty}^{t} a(\alpha)d\alpha + \nu) \tag{2.8}$$

where ν is a phase deviation inserted by local oscillators, inherent to most communications systems [14], f_c is the transmitted signal central frequency P_s is the signal's mean power, K_p is the modulation constant and $a(t)$ is the modulating signal. Chirps modulating signals are given by

$$a(t) = t - \frac{\tau_s}{2} \quad ; 0 < t < \tau_s \tag{2.9}$$

The transmitted signal complex envelope (with respect to the transmit central frequency) is then written as

$$\tilde{s}(t) = \sqrt{2P_s}e^{j\left[\frac{K_p t^2}{2} - \frac{K_p \tau_s t}{2} + \lambda\right]} \quad ; 0 < t < \tau_s \tag{2.10}$$

[3]The basic concept of pulse compression radars that employ linear frequency modulated signals (also referred to as chirps) was initially introduced by Dicke in 1945 [29].

Its bandwidth is $B_{\tilde{s}} = K_p \tau_s$ and the complex envelope of the signal component at the pulse compression output when such kind of waveform is employed is given by

$$\tilde{x}_i'(t) = Ae^{\frac{-4\pi R_0}{\lambda}} e^{\phi_r} \left[2P\tau_s e^{-j\frac{K_p t^2}{2}} sinc\Big(\frac{K_p \tau_s t}{2}\Big) \right] \tag{2.11}$$

The slant range resolution, estimated from the 3dB width in time of (2.11) is $\Delta R_s \approx \frac{c\,0.9}{2B_{\tilde{s}}}$ [69]. Finally, applying basic geometry (see Figure 2.1), the ground range resolution is given by

$$\Delta R_g = 0.9 \frac{c}{2B} \frac{1}{\sin\theta_0} \tag{2.12}$$

Note that the ground range resolution, being a function of θ_0 varies along the radar operation ranges. Observing Figure 2.1, it is possible to see that the resolution cell[4], i.e. the smallest fraction of the observed scenario liable of being analysed, comprises a range component and an azimuth component. If no signal processing technique is performed, the along-track or azimuth resolution is given as a function of the antenna 3dB width, θ_a, as illustrated in Figure 2.2.

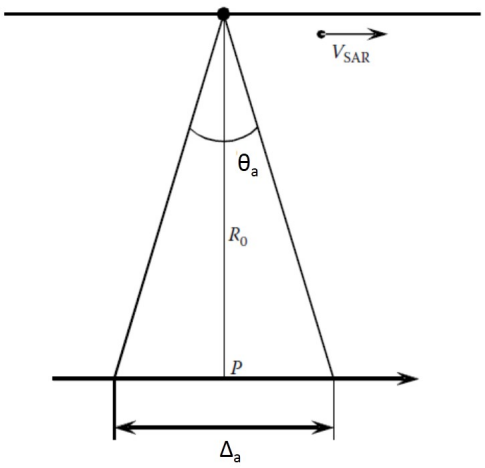

Figure 2.2: SAR strip map geometry - azimuthal view.

All signals reflected on scatters located within the azimuth resolution, for the same range, will be received at the same time. Therefore, with no additional signal processing this parameter is written as

$$\Delta R_a = R_0 \theta_a \approx R_0 \frac{\lambda}{L_y} \tag{2.13}$$

Note that higher resolution demands bigger antennas. Unfortunately, this constraint can not be fulfilled in an embedded architecture like the one presented in Figure 2.1. Therefore, it is necessary to synthesize a narrower antenna aperture through signal processing techniques.

[4]The resolution cell is also referred to as a pixel, following the idea that the final output of remote sensing radars corresponds to an image

In order to enhance the along-track resolution, it is first necessary to note that a given fixed point on the surface is illuminated several times by the radar as the platforms moves. Therefore, all pulses reflected on this given point on the surface, starting from the moment it enters the antenna main lobe, until the moment it leaves, can be jointly exploited. The outputs $\{\tilde{y}'_1(t), \ldots, \tilde{y}'_{n_p}(t)\}$ generated by the radar processing chain during a sequence of n_p transmission intervals are stored in a buffer and passed to an *azimuth compression* processing block. The azimuth compression operation takes into consideration that the slant range of this given point varies as a function of the platform position and, consequently, as a function of time.

First, let us write the slant range corresponding to the ith transmission as a function of the r_a coordinate of the platform and the minimum slant range, R_0, as

$$R_i = \sqrt{R_0 + (r_a - r_{a_0})} \tag{2.14}$$

with r_{a_0} being the value of r_a when $R_i = R_0$. It can be shown that (2.14) is approximately

$$R(r_a) = R_0 + \frac{v_{\text{sar}} t^2}{2R_0} \tag{2.15}$$

Considering that the slant range is directly related to the phase of the returned signal (see (2.3)), the variation with time reported in (2.15) induces a linear frequency modulation on the returned pulses, if analyzed in the azimuthal direction. Therefore, a similar procedure as the one performed in pulse compression for increasing range resolution can be employed in the azimuthal direction and the azimuth resolution can be shown to be given, independently of the range, by

$$\Delta R_a = \frac{L_y}{2} \tag{2.16}$$

The spatial resolution, defined trough (2.12) and (2.16), plays a key role in Synthetic Aperture Radars performance. The basic principle underpinning microwave remote sensing is that all scatters within a resolution cell contribute to the returned signal, i.e., when there are N_a multiple scatters within a single resolution cell, the received signal can be written as

$$r_i(t) = \sum_{j=1}^{N_a} r_{ij}(t) \tag{2.17}$$

Figure 2.3 illustrates the above mentioned scenario with multiple scatters within a single Strip-map SAR resolution cell, considering the antenna elevation aperture. Note further that the number of scatters N_a increases when the area under analysis presents an elevation profile, like in forested or urban scenarios.

It is important to highlight that (2.17) is a vectorial summation, meaning that the r_{ij} signals are added considering both their amplitude as well as their phase. Therefore, (2.17) can result in either a constructive or a destructive operation, improving, or deteriorating, the characterization of the illuminated scene.

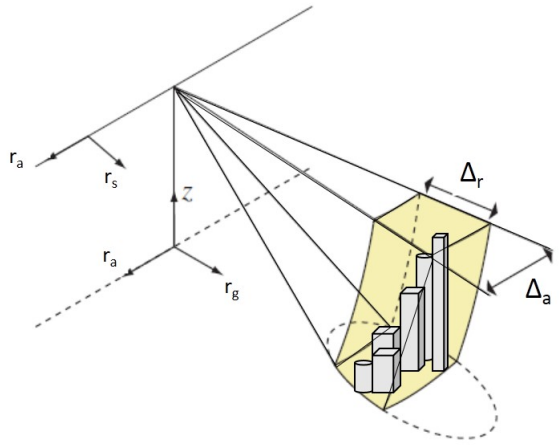

Figure 2.3: Volume within which all scatters returns are superposed (modified from [71]).

Multiple targets are always present in remote sensing data. Knowing how to properly address them is a key aspect of high performance remote sensing radars since they can be either wanted or unwanted. In other words, depending on the application, it can either be necessary to remove the contribution of the distributed scatters or to enhance it, in order to exploit the information provided by them, which will allow a better characterization of the scene under analysis.

When strong elementary scattering mechanisms are present, they will generally stand out, being easily identified. The behaviour of such scattering mechanisms are well known and many objects on the Earth's surface are precisely modeled as being one or a composition of a few of them. Among the elementary scattering mechanisms most present in SAR data it is possible to point out plates, dihedrals, trihedrals, helix and spheres, just to cite a few. Their characteristic electromagnetic behaviour comprises the target radar cross section (related to the backscattered signal power) and the phase shift induced on the backscattered signal (see (2.2)). Furthermore, this behaviour is a function not only of the scattering mechanisms own properties, but also the systems parameters, like the angle of incidence and the transmit frequency.

When the resolution cell does not contemplate a strong elementary scatter, the clutter is said to be distributed and its characterization has to be performed based on the mean behaviour of the several scattering mechanisms present in its composition. This type of clutter is addressed in more detail in Chapter 3. For the present moment, it is sufficient to state that its analysis is not straightforward, comprising the employment of probabilistic tools derived based on asymptotic statistics and stochastic models.

Prior to moving on, it is important to highlight that in the present work, other concepts related to image formation like terrain correction, foreshortening, layover, shadowing and platform motion compensation will not be addressed and are assumed to have been taken care of. For that purpose the reader is advised to go to the extensive specific literature, like [57, 87].

2.2 Multiple Acquisitions

The outcome of the procedure described in the previous section is a single look complex (SLC) image. The image interpretation stage can be performed on the latter, taking into consideration the amplitude and phase of the received signal corresponding to each pixel (resolution cell), or multiple images (originated from several acquisitions) can be jointly analysed. As already mentioned in the preamble of this Chapter, changing the properties of the transmit waveform as well as the angle of illumination, directly affects the backscattered energy and the perception of the targets on the scene. Therefore, not only it is possible to use this information to optimize a single acquisition, but also it is possible to change properties between acquisitions and combine the results in a multivariate analysis.

Generally, in remote sensing, the parameters that are most interesting to be modified between acquisitions are the central transmit frequency, the angle of illumination, or the antenna position, and the polarization state of the transmit waveform. In the present work, images acquired with different antenna positions are employed under the iterferometric context, while images acquired with different polarization states are addressed under the polarimetric principles. Next, these two fields of SAR image interpretation are closer analysed.

2.2.1 Polarimetry

In free space, the polarization state of the electromagnetic wave does not change the propagation properties of the latter. Nevertheless, as previously mentioned, different objects/materials backscatter the incident electromagnetic wave in a unique fashion, as a function of both their properties as well as the wave's. The latter also holds for the polarization state of the transmit waveform. Therefore, additional information can be extracted when analysing the dependence of the reflecting signal to this feature. In the present section we revisit a few theoretical principles related to the electromagnetic properties of the waves involved in radar systems as well as how they can be taken into consideration to enhance the study of a given sensed area.

Polarization background

The concept of polarization is related to the orientation of the electrical field with respect to the direction of propagation of the electromagnetic wave. It is important to highlight that, in remote sensing SAR systems, the assumption that the illuminated targets are in the antenna far field is generally accepted. Therefore, not only we can consider the wavefront planar (independently of the antenna properties), but also it is possible to assume that we are dealing with transverse electromagnetic (TEM) waves. Hence, the orientation of the magnetic field is always perpendicular to the one of the electric field. Thus, and still considering their dependence characterised by the impedance of the free space, we neglect the behaviour of the magnetic field throughout this thesis, focusing only on the electric filed properties.

Suppose **u** and **t** form an orthonormal basis in a plane perpendicular to the direction of propagation. The electrical field vector of a given electromagnetic wave is then given by

$$\mathbf{E} = \begin{bmatrix} E_u \\ E_t \end{bmatrix} = \begin{bmatrix} e_u \cos(2\pi f t - kR + \delta_u) \\ e_t \cos(2\pi f t - kR + \delta_t) \end{bmatrix} \tag{2.18}$$

where f is the central frequency, k is the wave number, R is the distance travelled by the wave (slant range, see Figure 2.1) and δ_i, $i = u, t$, are phase terms.

With no loss of generality and for the sake of simplicity, throughout this section we consider **u** and **t** to be, respectively, unitary vectors on the incident plane and on the plane perpendicular to the latter. As a heritage of communication systems, the polarization state corresponding to each of the aforementioned vectors solely are respectively called horizontal and vertical, as a reference to their position with respect to the Earth's surface. Therefore, the unitary vectors are assigned the nomenclature **h** and **v** and the resultant basis is referred to as linear. Note that the phase difference between the two components (horizontal and vertical), combined with their time dependence causes the Electric field vector to move according to an ellipse (in the most general case). The equation of the ellipse is given by [87]

$$\left(\frac{E_v}{e_v}\right)^2 + \left(\frac{E_h}{e_h}\right)^2 - 2\frac{E_h E_v}{e_h e_v}\cos(\delta) = \sin^2(\delta) \tag{2.19}$$

where $E_h = e_h \cos(2\pi f t - kR)$, $E_v = e_v \cos(2\pi f t - kR + \delta)$ and $\delta = \delta_v - \delta_h$.

Figure 2.4 presents an illustration of the propagation path of an electromagnetic wave along with the Electric field vector.

Note that the derivation made considering the linear polarization basis (horizontal/vertical), can be easily extended for other basis with no additional measurement [57]. Left and right circular polarization basis is the most employed one following the linear. These two components are easily derived from the polarization ellipse formulation (see (2.19)) and they occur when $a_h = a_v$ and $\delta = \pm\pi/2$. In a matrix format, it is possible to write

$$\begin{bmatrix} E_l \\ E_r \end{bmatrix} = \frac{1}{\sqrt{2}} \begin{bmatrix} 1 & -j \\ 1 & j \end{bmatrix} \begin{bmatrix} E_h \\ E_v \end{bmatrix} \tag{2.20}$$

where E_l and E_r are the Electric field vectors representing a purely left circular and right circular polarization sate, respectively.

A simpler representation of the Electric field described in (2.18) is given by the Jones vector [87] as a function of the polarization ellipse parameters as follow

$$\mathbf{E} = Ae^{j\alpha} \begin{bmatrix} \cos\tau & -\sin\tau \\ \sin\tau & \cos\tau \end{bmatrix} \begin{bmatrix} \cos\epsilon \\ j\sin\epsilon \end{bmatrix} \tag{2.21}$$

where δ is the inclination of the ellipse with respect to the horizontal direction and ϵ is the ellipticity. The amplitude A and the total phase term α are parameters generally neglected, therefore we will not address their formulation. For that purpose the reader is advised to go to [87, 57].

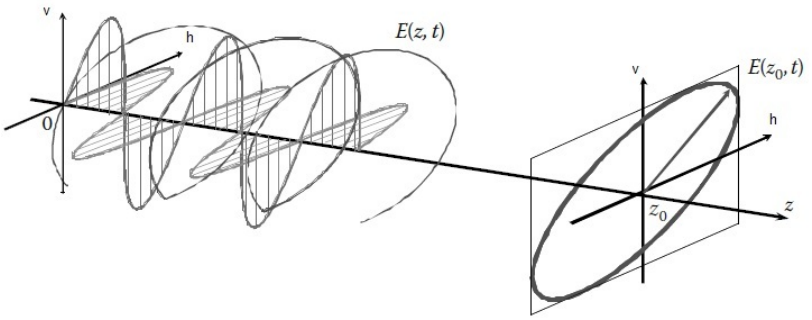

(a)

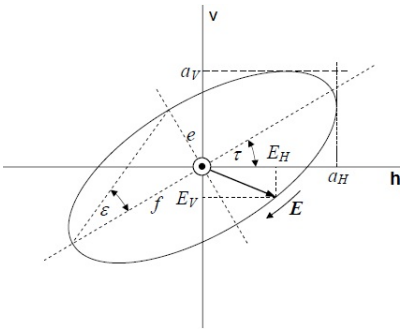

(b)

Figure 2.4: (a) Electromagnetic wave propagation; (b) Propagation ellipse.

Alternatively, a convenient way of describing the polarimetric state of the wave is through the Poincaré sphere. The latter is a geometric representation that takes into consideration the Stokes parameters, which, in turn, are given as function of the polarization Ellipse (see (2.19)) as follows

$$\mathbf{s} = \begin{bmatrix} s_0 \\ s_1 \\ s_2 \\ s_3 \end{bmatrix} = \begin{bmatrix} a_h^2 + a_v^2 \\ a_h^2 - a_v^2 \\ 2a_h a_v \cos\delta \\ 2a_h a_v \sin\delta \end{bmatrix} \tag{2.22}$$

In (2.22), $\mathbf{s}$ is referred to as the Stokes vector whose components present the following interesting property

$$s_0^2 = s_1^2 + s_2^2 + s_3^2 \tag{2.23}$$

with s_0 being the total power density of the electromagnetic wave.

Note that (2.23) describes the equation of a sphere (Poicaré sphere) with radius s_0, whose surface comprises all possible polarization states of an electromagnetic wave. Figure 2.5 presents the referred sphere.

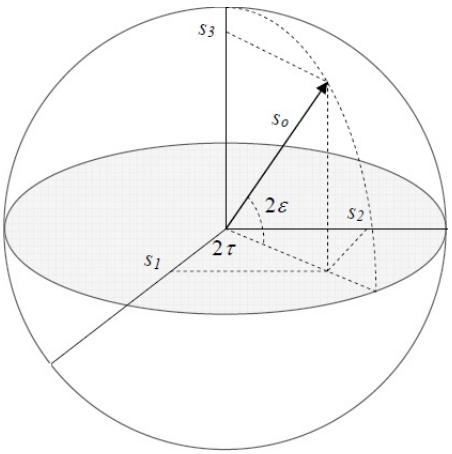

Figure 2.5: Poicaré sphere representation of the Electromagnetic wave polarization state.

Depending on the stationarity of the scattering surface, the returned electromagnetic wave can be partially polarized or even unpolarized. These phenomena generally occur when the illuminated targets are distributed, i.e. multiple scatters within a single resolution cell (see Section 2.1). For these special cases, the Stokes parameters are estimated using the concept of statistical expectancy, which, assuming the ergodicity property are evaluated as the spatial averages of neighbouring pixels. In these cases, the polarization state of the reflected waveform will be represented by a point inside the Poincaré sphere. The Jones coherency matrix **J** is generally taken into consideration when addressing such scatters. It is given by

$$\mathbf{J} = E\left[\mathbf{E}\mathbf{E}^H\right] \tag{2.24}$$

where $E[\cdot]$ is the expectation operator.

In the present section the basic principles of electromagnetic wave polarization were presented. Next, we address how SAR systems can exploit the polarimetric properties of the signals involved (both in transmission and reception) in order to enhance the characterization of the area under study.

Polarimetric Radar

In order to better interpret geophysical behaviors, Synthetic Aperture Radars gave rise to Polarimetric SAR (PolSAR) systems. PolSAR data describes the interaction between the electromagnetic waves and the scatters within a resolution cell, for each polarimetric state of the former. Compared to the univariate analysis of single polarization systems, the multivariate nature of Polarimetric SAR (PolSAR) data allows for a better prediction of the physical properties of the illuminated targets, leading to more effective classification, detection and geophysical parameter inversion algorithms.

With respect to the system described in Section 2.1, the only difference is that the waveforms are transmitted horizontally and vertically polarized, alternatively, and signals are re-

ceived in both antennas simultaneously. Therefore, four SLC images are formed, one for each pair of transmit/received polarization state. The image formation procedure is performed in an unchanged manner as previously described, and the spatial resolution formulation is the same as the one derived in Section 2.1.

In order to properly address the dependence of the scattering mechanisms characterization with the polarization state of the waveforms, let us first revisit the target radar cross section concept introduced in (2.1). This parameter is a function of the incident and backscattered waves electric field, $\mathbf{E^i}$ and $\mathbf{E^b}$, respectively, and is written as

$$\sigma = 4\pi R_0^2 \frac{|\mathbf{E^b}|}{|\mathbf{E^i}|} \tag{2.25}$$

Furthermore, since the backscatter of a given object/material is a function of the polarization state of the incident (and consequently the transmit) waveform, it is reasonable to say that for each of the four combination of polarization states previously mentioned, there is a target radar cross section associated. In the present work, they are uniquely addressed as σ_{qp}, where q and p represent the polarization state of the scattered and incident wave, respectively.

It is clear from (2.25) that the way the electric fields of the incident and backscattered waves interact with one another as a function of their polarization state is a key factor in PolSAR data analysis. The Sinclair (or Scattering) matrix, $\mathbf{S}$, describes these relations as follow

$$\mathbf{E^b} = \mathbf{S}\mathbf{E^i} \tag{2.26}$$

where

$$\mathbf{S} = \begin{bmatrix} S_{hh} & S_{hv} \\ S_{vh} & S_{vv} \end{bmatrix} \quad \text{and} \quad \mathbf{E^j} \begin{bmatrix} E_h^q \\ E_v^q \end{bmatrix} \tag{2.27}$$

where $j = b, i$

The same nomenclature, with respect to the indexes, described above is adopted in (2.27), i.e. given a component of the Sinclair matrix, S_{qp}, q and p represent the polarization state of the scattered and incident wave, respectively. Finally, each target radar cross section,σ_{qp}, can be shown to be

$$\sigma_{qp} = 4\pi |S_{qp}|^2 \tag{2.28}$$

It is clear, from (2.28) and (2.1), that the power of the received signal is polarization dependent and, consequently, each of the PolSAR images presents complementary information. Nevertheless, it is important to highlight that the elements of the Sinclair matrix, S_{qp}, are complex quantities, therefore there are also additional information related to the phase of the received signals. In summary, instead of having just an amplitude and phase associated to a given resolution cell, in PolSAR systems there are four amplitudes and four phases that

can be jointly exploited to better characterize the targets. Prior to continue, it is important to mention that the system coordinates used throughout the present work is the backscatter alignment (BSA).

The abovementioned polarization dependent information can be also represented in a vector format, characterizing what is called the target vector. The four components of the multivariate PolSAR target vector, $\mathbf{k}$, describing the polarimetric characteristics of a single coherent scattering mechanism within each resolution cell are the elements of the Sinclair matrix: S_{hh}, S_{hv}, S_{vh} and S_{vv}. For monostatic configurations, where the reciprocity theorem applies (i.e., $S_{hv} = S_{vh}$)[5] only three components remain: S_{hh}, S_{hv} and S_{vv}. In this case, the dimension of the target vector $\mathbf{k}$ becomes $m = 3$ and it is written as

$$\mathbf{k} = [S_{hh} \quad S_{hv} \quad S_{vv}]^T \tag{2.29}$$

Alternatively, it can be represented in Pauli basis as follow

$$\mathbf{k} = \frac{1}{\sqrt{2}}[S_{hh} + S_{vv} \quad S_{hh} - S_{vv} \quad 2S_{hv}]^T \tag{2.30}$$

The Pauli basis is generally preferred over the lexicographic representation for two reasons: it is closely related to the physics of wave scattering [20] and it has a straightforward manner of indicating a rotation around the radar line of sight in matrix form [49].

Polarimetric Target Decomposition

As previously mentioned, a resolution cell is the smallest fraction of the observed scenario liable of being analysed. Due to system limitations or to intrinsic characteristics of the reflecting objects, several different scattering mechanisms can be comprised within a single resolution cell. In such cases the target is said to be distributed (instead of point) and the electromagnetic behaviour of the returned signal is a mixture of multiple sources. Depending on the application, the correct retrieval of the canonical scatters within a resolution cell becomes imperative for a precise interpretation of the illuminated targets/scene and the estimation of quantitative information from them.

The Polarimetric Target Decomposition is a PolSAR image interpretation technique that enables the description of an image cell as a sum of canonical scattering mechanisms (each represented by a specific target vector) making it more intuitive to understand the behaviour of the clutter and therefore to analyse it [98]. Target decompositions are mainly classified in coherent, if their interest lies on the scattering matrix analysis for each resolution cell, like the ones proposed by Cameron [12, 11] and Krogager [52], or incoherent, if they are based on a statistical analysis of neighbouring pixels. Coherent decompositions are better suited for deterministic clutter analysis, not being appropriate for high resolution systems imaging

[5] When the Faraday rotation phenomenon is observed in SAR systems the reciprocity theorem may not apply [87].

distributed heterogeneous clutters. Therefore, we will not address such techniques throughout this thesis.

Incoherent target decomposition (ICTD) theory on the other hand assumes that the scattering process in most natural media is a combination of coherent speckle noise and random vector scattering effects. Therefore, a stochastic approach is required and the concept of average or dominant scattering mechanisms is associated to each imaging cell [18]. Most methods described in the literature focus on the Hermitian, semidefinite positive coherence or covariance matrix [18, 98]. Assuming that the reciprocity theorem is valid (see (2.29)), the covariance matrix $[M]$ is defined as

$$[M] = E\left[\mathbf{k}\mathbf{k}^H\right] = \begin{bmatrix} E\left[S_{hh}S_{hh}^H\right] & E\left[S_{hh}S_{hv}^H\right] & E\left[S_{hh}S_{vv}^H\right] \\ E\left[S_{hv}S_{hh}^H\right] & E\left[S_{hv}S_{hv}^H\right] & E\left[S_{hv}S_{vv}^H\right] \\ E\left[S_{vv}S_{hh}^H\right] & E\left[S_{vv}S_{hv}^H\right] & E\left[S_{vv}S_{vv}^H\right] \end{bmatrix} \tag{2.31}$$

where $E[\cdot]$ is the expectation operator and $\cdot^H$ is the complex conjugate transpose operator.

Note that (2.31) was derived taking into consideration the target vector $\mathbf{k}$ written in the lexicographic basis (see (2.29)). Alternatively, if the Pauli basis was considered (see (2.30)), $[M]$ would be referred to as the *coherence matrix*. Throughout this thesis, the coherence and the covariance Matrix are used indistinctly and are referred simply as $[M]$.

As reported in more details in the next chapters of this thesis, the analysis based on the second order moment may not be the most indicated approach for specific type of clutters. Therefore, the investigation of higher order moments has recently sparked great interest of the SAR community, introducing supplementary information to the clutter analysis and consequently leading to new ICTD approaches [30, 3]. In Chapter 4, a dedicated discussion over ICTD techniques is performed.

2.2.2 Interferometry

Interferometric radars take advantage of the information acquired by two sensors located in distinct positions to infer characteristics of the third dimension of the sensed area (scatters/terrain height). The employment of a greater set of acquisitions (more antennas or baselines) can be used in tomographic applications to derive the entire height profile of a given imaged area. Tomography is out of the scope of the present work, for that purpose the reader is advised to go to the extensive literature already published, like [86, 94, 16, 51, 72].

The terrain height of a given pixel is estimated from the phase difference (also referred to as the *interferometric phase*) between the two SLC images[6]. Figure 2.6 illustrates the acquisition architecture and the geometric procedure employed to extract the interferometric phase.

[6]For interferometric applications, the phases from the flat earth phase component and the topographic phase should be removed before any analysis.

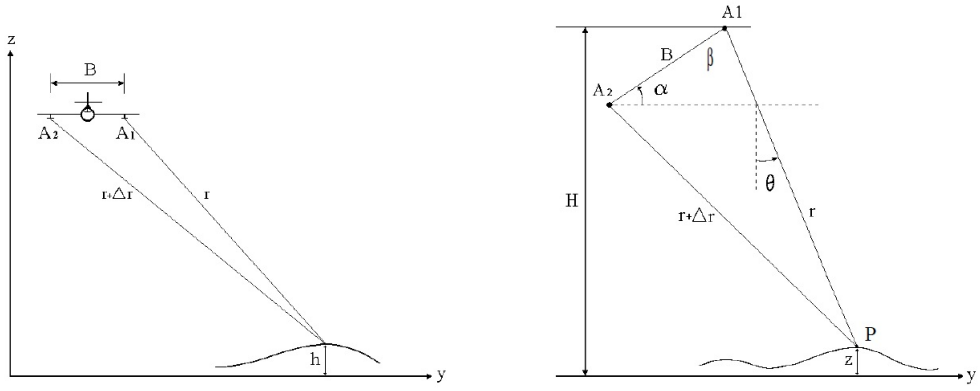

(a) (b)

Figure 2.6: (a) Dual antenna acquisition configuration; (b) Basic geometry of an Interferometric SAR system.

Note that the antennas A1 e A2 are separated by the base line B, whose tilt angle is α. H is their height and θ the illumination angle. In the configuration presented in Figure 2.6 both antennas are located on the same aircraft and the two SLC images are formed at the same time. If the same antenna shall be used for interferometric applications, two distinct flights would have to be performed with flights trajectories separated by a distance B. This specific branch of interferometry is addressed in the literature as multi-pass interferometry.

Note that

$$(r + \Delta r)^2 = r^2 + B^2 - 2rB\sin(\alpha - \theta) \rightarrow r = \frac{B^2 - \Delta r^2}{2(\Delta r + B\sin(\alpha - \theta))} \tag{2.32}$$

where $\Delta r = \frac{\lambda \Delta \phi}{4\pi}$ and $\Delta\phi$ is the phase difference extracted from the two SLC images. Finally, the height z is estimated as

$$z(r, \theta) = H - r\cos(\theta) \tag{2.33}$$

It is important to highlight that the interferometric phase of a given pixel only adds relevant information to the analysis if there is a certain degree of statistical correlation between the two images taken into consideration. In other words, if the received signals from the two different acquisitions, relative to the same area on the ground are decorrelated, then the interferometric phase does not introduce any meaningful information [87].

Decorrelation between two distinct acquisitions can be caused by several phenomena, both relative to the type of scatters being sensed or due to external factors. If the analysed pixel corresponds to a shadow area, for example, it is then composed mainly by thermal noise, hence the given signals are completely decorrelated. Otherwise, neglecting decorrelation caused by hardware mismatch between acquisitions and incorrect image registration (they are both assumed to be precisely done), the decorrelation can occur due to changes in the sensed area (specially in multi-pass interferometry). Natural changes range from the movement of the ocean to forest growth, while external factors can be, for example, the displacement of

a moving deterministic target on the scene. It is clear that such events will induce varied effects on the interferometric phase. Depending on the application, some can be neglected while others can't.

The coherence defined in (2.34) is a complex parameter whose magnitude represents a measure of the degree of correlation between two signals, corresponding to the same area on the ground, from two distinct images [57].

$$\rho_M = \frac{E[S_1 S_2^*]}{\sqrt{E[|S_1^2|E[|S_2^2|]]}} \tag{2.34}$$

where S_i, $i = 1, 2$ are the components of each SAR acquisition and $E[\cdot]$, as previously defined is the expectation operator.

Note that the coherence, being a parameter defined for any two SAR acquisitions, can be employed in varied analysis that takes into account the temporal behaviour of the area under study. High coherence acquisitions of a given area can be employed to evaluate specific types of algorithms, while the high degree of decorrelation between acquisitions (low coherence) can indicate significant temporal change of the area under study (information relevant in deforestation detection applications, for example).

In (2.34), S_1 and S_2 may correspond to different polarization pairs (transmit/receive polarization sate). Furthermore, in full polarimetric systems ($m = 3$), the entire target vector $\mathbf{k}$ can be taken into consideration [87]. Such approach is addressed in the literature as PolInSAR, accounting for the joint analysis of the information provided by both interferometric as well as polarimetric acquisitions. For such cases, the coherence in (2.34) is given by

$$\rho_k = \frac{E[\mathbf{k}_1 \mathbf{k}_2^H]}{\sqrt{E[|\mathbf{k}_1^2|E[|\mathbf{k}_2^2|]]}} \tag{2.35}$$

Note that (2.35) is an extension of the Coherence matrix defined in (2.31).

Chapter 3

PolSAR Clutter Stochastic Assessment

Sommaire

Each radar application faces different challenges during the return signal interpretation. Generally, when there is only a single dominant scatter within a resolution cell (point target), the signal processing stage is straightforward. This is the case of air surveillance radars for example. Nevertheless, when distributed targets are under investigation, special care has to be taken.

As previously mentioned, in remote sensing, multiple scatters are always present in a given resolution cell. Generally, when the interest lies in strong deterministic targets (such as man made structures), the contribution of distributed targets produces an undesired effect in the image, referred in the literature as *speckle noise*. In such cases, there is a need to understand the clutter behaviour up to a stage that allows the proposal of specific algorithms that can either reduce or remove its effect (e.g. speckle filtering algorithms [**florence**, **idan**, 56, 61]). The study of clutters composed solely by distributed targets (e.g. vegetation, forests and snow) is more challenging, requiring an analysis usually based on the stochastic properties of the SAR data targeted in extracting information on their composition.

Compared to the univariate analysis of single polarization systems, the multivariate nature of PolSAR data allows for a better prediction of the physical properties of the illuminated targets. Nevertheless, the characterization of multivariate data based on asymptotic statistics is considerably more complex. In the present chapter we investigate in closer details specific aspects related to PolSAR clutter stochastic models.

3.1 Multivariate Zero-Mean Circular Gaussian model

When the scene is homogeneous or when low-resolution SAR systems (either single polarization or multi polarization) are under investigation, situations where the number of scattering mechanism within a resolution cell is considerably large, the central limit theorem can be taken into consideration (see (2.17)). Therefore, the received signals can be locally modelled by an univariate or multivariate (depending if the system is single or multi polarization) zero-mean circular Gaussian stochastic process, being completely characterized by their variance or covariance matrix. More precisely, the probability density function of the target vector $\mathbf{k}$ defined in (2.29) is given by [59, 95]

$$p_k(\mathbf{k}) = \frac{1}{\pi^m |[M]|} \exp\left(-\mathbf{k}^H [M]^{-1} \mathbf{k}\right) \tag{3.1}$$

where, $[M]$ is the $m \times m$ Hermitian, semi-positive definite covariance matrix (see (2.31)) and m, as reported in Chapter 2, assumes the values $m = 3, 4$, depending if the reciprocity theorem applies or not, respectively.

If we further assume that the components of the target vector, S_{qp}, $q, p = h, v$, are ergodic in mean and in correlation and that their cross products terms, $S_{qp} S_{tu}^*$, $t, u = h, v$, are wide sense stationary in mean [65], the maximum likelihood estimator of (2.31) is obtained by performing a neighbouring spatial average as follow

$$\widehat{[M]} = \frac{1}{n} \sum_{i=1}^{n} \mathbf{k}_i \mathbf{k}_i^H \tag{3.2}$$

where $\mathbf{k}_i$ is the target vector of the ith resolution cell (pixel) and n is the number of pixels used in the averaging operation. $\widehat{[M]}$ is referred in the literature as the sample covariance matrix and is characterized by a Wishart distribution as follows

$$p(\widehat{[M]}) = \frac{n^{mn} \widehat{[M]}^{n-m}}{[M]^n \tilde{\Gamma}_m(n)} \mathrm{etr}(-n[M]^{-1} \widehat{[M]}) \tag{3.3}$$

where $\mathrm{etr}(\cdot)$ is the operator that performs the exponential of a given matrix trace and $\tilde{\Gamma}$ is the multivariate gamma function defined, as a function of the Gamma function Γ, by [65]

$$\tilde{\Gamma}_m(n) = \pi^{m(m-1)/2} \prod_{i=1}^{n} \Gamma(n - i + 1) \tag{3.4}$$

With the improved resolution of modern SAR platforms, the number of scatters within each resolution cell decreases considerably. High scene heterogeneity may eventually lead to non-Gaussian clutter modelling, requiring more complex stochastic models for the analysis. Several special cases of univariate stochastic processes (K-compound, Weibull, etc.) have been extensively studied over the years. They all fall in the same class of compound Gaussian distributions [76] which, in turn, had been previously grouped under the SIRP (Spherically

Invariant Random Process) family [78], whose name is often used for referring to the aforementioned stochastic processes [25, 26, 84].

Multivariate versions of SIRP distributions, namely SIRVs (Spherically Invariant Random Vectors) [107], have been frequently employed for modelling high-resolution POLSAR data [104, 7, 41, 105]. In the next section, a brief description of the referred stochastic model with normalised covariance matrix is performed. For a more detailed description of such class of random vectors, the reader is advised to go to [76].

3.2 Spherically Invariant Random Vector (SIRV) model

The SIRV is a multiplicative model that expresses the SAR signal as a product between the square root of a scalar positive quantity (texture) and the description of an equivalent homogeneous surface (speckle) [102]. It is important to notice that in the SIRV definition, the texture probability density function is not explicitly specified. As a consequence, SIRVs describe a whole class of stochastic processes [85], including the Gaussian (multivariate) model (deterministic texture), KummerU distribution (Fisher texture) [7], the multivariate $\mathcal{K}$ distribution (Gamma texture) [74] and the $\mathcal{G}^0$ distribution (inverse Gamma texture) [73], the last two being special cases of the more general multivariate $\mathcal{G}$-family, specially suited for extremely heterogeneous clutters [44, 43]. Let us now address the mathematical model that describe this class of random vectors.

As described in Section 2.2.1, for an m-dimensional PolSAR system ($m \leq 4$), the single channel model [40] has been extended as follows: in each ith azimuth / range location, $\mathbf{k}_i$ is the $m \times 1$ complex target vector corresponding to the same area on the ground. For distributed targets, the corresponding $\mathbf{k}$ vector is considered non-deterministic and may be written under the SIRV assumption.

The SIRV is, originally, a class of non-homogeneous Gaussian processes with random variance [104]. It is an important subclass of Complex Elliptically Symmetric Distributions (CES), also referred to as compound-Gaussian [76], where each m-dimensional observation vector $\mathbf{k}$ is defined as

$$\mathbf{k} = \sqrt{\boldsymbol{\tau}} \cdot \mathbf{z} \tag{3.5}$$

where $\mathbf{z}$ is an independent complex circular Gaussian vector, characterising the speckle, with zero mean and covariance matrix of the form $[T] = \sigma_0 \cdot [M]$, such that $\mathrm{Tr}\{|M|\} = 1$ and σ_0 is the total power (span). In (E.2), $\boldsymbol{\tau}$ represents the texture, a positive random variable characterising the spatial variations in the radar backscattering, which is statistically independent of the speckle. The probability density function of the texture random variable is not explicitly specified by the model, therefore, as previously mentioned in this section, SIRVs describe a wide range of well known specific models.

The generalisation of the $[M]$ maximum likelihood estimator (obtained under the deter-

ministic texture case) is the solution of the recursive equation given by

$$[\widehat{M}]_{FP} = f([\widehat{M}]_{FP}) = \frac{1}{n}\sum_{i=1}^{n}\frac{\mathbf{k}_i\mathbf{k}_i^H}{\mathbf{k}_i^H[\widehat{M}]_{FP}^{-1}\mathbf{k}_i} \tag{3.6}$$

where $\mathbf{k}_i$, $0 < i < n$ represents each sample (pixel) of the observation dataset, $\cdot^H$ is the complex conjugate transpose operator and the acronym FP stands for a Fixed-Point iteration. Equation (3.6) is often referred to as the M-estimator of scatter [76].

The generalised texture maximum likelihood estimator [104] for each observation vector is given by

$$\hat{\tau}_i = \frac{\mathbf{k}_i^H[\widehat{M}]_{FP}^{-1}\mathbf{k}_i}{m} \tag{3.7}$$

Note that the estimator described in (3.7) is a function of the covariance matrix estimator described in (3.6) and does not rely on the sample (spatially averaged) covariance matrix.

In summary, the characterisation of the PolSAR target vector $\mathbf{k}$ reduces to determining the probability density function of the texture, which is the same for all channels, and the covariance matrix $[M]$ of the speckle, from which it is possible to infer the nature of the most dominant scatters in the scene as well as the identification of their mixture process inside each cell, i.e. parametrization [18].

Aside from the formulation presented above, many methods have been proposed in the literature to both derive the covariance matrix $[M]$ as well as the texture characteristics under specific stochastic model assumptions. Usually, optimal solutions rely on maximum likelihood estimators, which are highly dependent on the model adopted [76]. With the exception of the sample covariance matrix (see (3.2)) which, asides from being the maximum likelihood estimator under the Gaussian clutter assumption, features a geometric/physical meaning for its estimation (i.e. it can be thought of as the centre of mass of the estimated covariance matrices for each pixel), other estimators loose their meaning if the assumed model does not hold, becoming sub-optimal. Furthermore, the assumption of either a Gaussian clutter or the product model to describe the heterogeneous clutter are basic assumptions of many algorithms related to segmentation and classification of PolSAR images, which would have their performance dramatically affected if their assumed models are not valid.

Despite its widespread use among the community, many authors raised the question if considering the texture polarization independent is the most suitable model for all kinds of clutter [35, 97]. In particular, under forested scenarios, where the returned signal may probably contain contributions from surface, double bounce and volume type of scatters, each one originated from different sources and thus potentially having different textures, a higher deviation from this model is expected [35]. Indeed, experimental results showed significant variations of the texture measures among the polarization channels for such kind of scenario [2] evidencing the criticality of the assumptions done with the model prior to any SAR image processing operation (segmentation, classification, speckle filtering).

Within this context, in the next section a general framework is proposed for evaluate

quantitatively the fitting of SIRV stochastic models with respect to a given multidimensional SAR dataset. Briefly, the procedure relies on the fact that the SIRV model is a specific subclass of Complex Elliptically Symmetric Distributions (CES), also referred to as compound Gaussian [76]. A Wald test is derived to verify if the structure of the fourth order moment corresponds to that of an elliptical population. The proposed method has a relatively simple form and is derived based on the Schott test for real valued random vectors [90].

3.3 Wald test on Complex Elliptical Symmetric Distribution

Testing for spherical or elliptical distributions is not a relative new subject in neither signal processing nor statistics community. Nevertheless, most of the tests are designed for real valued data and rely on the estimation of high order moment matrices [1, 38], not being suitable for PolSAR evaluation, since the latter is characterised by complex random variables and a possible mapping $\mathbb{C} \to \mathbb{R}$ would double the dimensionality of the problem, increasing significantly the complexity of the algorithms. Within this context, the procedure adopted here to derive the test on complex elliptical symmetry is analogous to what has been done by Schott with real valued random vectors [90]. Hence a few steps are deliberately let implicit being their derivation straightforward due to their conformity with the real case.

As previously mentioned, the SIRV model is a specific subclass of Complex Elliptically Symmetric Distributions (CES), also referred to as compound Gaussian [76]. CES distributions present an important property which states that their higher order moment matrices are scalars multiple of their correspondent Complex Normal Distribution (CN) [90]. Therefore, most of the statistic theory derived for CN can be easily adjusted to fit CES. Consequently, an easy way to verify if a dataset follows a CES distribution is simply to verify if the structure of its fourth order moment (quadricovariance matrix) retains this property.

Let the observation vector $\mathbf{k}$ be an $m \times n$ dataset where $m \leq 4$ is the number of polarization channels used by the system and n is the number of samples acquired from an homogeneous region, that share the same statistical properties. Furthermore, assume that this dataset is extracted from a finite second order moment elliptical distribution with zero mean vector and covariance matrix $[M]$. Therefore, the asymptotic normal distribution of the random vector $n^{1/2}\mathrm{vec}(\widehat{[M]} - [M])$, where $\mathrm{vec}(\cdot)$ is the operator that transforms a matrix into a column vector [66] and $\widehat{[M]}$ is the unbiased sample covariance matrix, is zero mean with covariance matrix Ω and pseudo-covariance matrix P, respectively given by

$$\begin{aligned} \Omega &= \sigma_1([M]^* \otimes [M]) + \sigma_2 \mathrm{vec}([M])\mathrm{vec}([M])^H \\ P &= \sigma_1([M]^* \otimes [M])K_{mm} + \sigma_2 \mathrm{vec}([M])\mathrm{vec}([M])^T \end{aligned} \tag{3.8}$$

where K_{mm} is a commutation matrix [66], $\cdot^*$ and $\cdot^H$ are the complex and complex transpose operators respectively, $\cdot^T$ stands for the transpose operation, $\otimes$ is the Kronecker product operator and σ_1 and σ_2 are functions of the dimensionality m and the CES characteristic function generator ψ [67]. Without loss of generality, assuming fitness of the fourth order moment of the CES, and that the texture τ is unit mean, they reduce to $\sigma_1 = 1 + \omega$ and

$\sigma_2 = \omega$ [76]. It is worth pointing out that ω is still a function of m and ψ and, as physical meaning, it represents the variance of the texture [76].

The fourth order moment matrix $[M]_4 = E\left[\mathbf{k}\mathbf{k}^H \otimes \mathbf{k}\mathbf{k}^H\right]$ is given by (see Appendix A)

$$[M]_4 = (1+\omega)\left[(I_{m^2} + K_{mm})\left([M] \otimes [M]\right)\right] \tag{3.9}$$

where I_q is the $q \times q$ identity matrix .

According to [39], the sample complex quadricovariance estimator can be expressed in terms of the Kronecker product as

$$\widehat{[M]}_4 = \frac{1}{n}\sum_{i=1}^{n} \mathbf{k}_i\mathbf{k}_i^H \otimes \mathbf{k}_i\mathbf{k}_i^H \tag{3.10}$$

Its corresponding standardized form is given by

$$\widehat{[M]}_{4*} = \left(\widehat{[M]}^{-\frac{1}{2}^H} \otimes \widehat{[M]}^{-\frac{1}{2}^H}\right)\widehat{[M]}_4\left(\widehat{[M]}^{-\frac{1}{2}} \otimes \widehat{[M]}^{-\frac{1}{2}}\right) \tag{3.11}$$

where $\widehat{[M]}^{-\frac{1}{2}} \cdot \widehat{[M]}^{-\frac{1}{2}^H} = \widehat{[M]}^{-1}$.

Assuming that $A = \widehat{[M]} - [M]$ and $C = \widehat{[M]}_4 - [M]_4$, it is shown in the Appendix B that, concerning the effectiveness of the test, we may assume hereafter, with no loss of generality, that $[M] = I_m$, where I_m is the m x m identity matrix and that

$$\mathrm{vec}(\widehat{[M]}_{4*}) = (1+\omega)\mathrm{vec}([N]_4) + \mathrm{vec}(C) - (1+\omega)H\mathrm{vec}(A) + O_p(n^{-1/2}) \tag{3.12}$$

where $[N]_4$ is what $[M]_4$ simplifies to when $k_i \sim CN_m(0, I_m)$ and H is an operator given by

$$H = [I_{m^2}\otimes(I_{m^2}+K_{mm})]\cdot\{I_m\otimes[(K_{mm}\otimes I_m)\cdot(I_m\otimes\mathrm{vec}(I_m))]+[(I_m\otimes K_{mm})\cdot(\mathrm{vec}(I_m)\otimes I_m)]\otimes I_m\} \tag{3.13}$$

Note that (3.12) is asymptotically equal to

$$\mathrm{vec}(\widehat{[M]}_{4*}) = (1+\omega)\mathrm{vec}([N]_4) + O_p(n^{-1/2}) \tag{3.14}$$

Therefore, defining $G = \rho^{-1}\mathrm{vec}(N_4)\mathrm{vec}(N_4)^T$, with $\rho = \mathrm{vec}(N_4)^T\mathrm{vec}(N_4)$, it is possible to state that $G\mathrm{vec}(\widehat{[M]}_{4*})$ is a consistent estimator of $[M_4]$ if and only if $[M_4]$ has the structure defined in (3.9). Hence, assuming that the latter is true, it is of common knowledge that

$$n^{1/2}v = n^{1/2}(I_{m^4} - G)\mathrm{vec}(\widehat{[M]}_{4*}) \tag{3.15}$$

is asymptotically normal with zero mean and covariance matrix

$$\Phi = (I_{m^4} - G)\Xi(I_{m^4} - G) \tag{3.16}$$

where Ξ denotes the asymptotic covariance matrix of $n^{1/2}\mathrm{vec}(\widehat{[M]}_{4*})$.

The Wald test for complex-valued signals states that

$$T = nv^H \Gamma v \tag{3.17}$$

has an asymptotic chi-squared distribution with degrees of freedom f equal to the rank of Φ if Γ is a consistent estimator of a generalised inverse of the latter. In other words, if the tested samples are elliptically symmetric (hypothesis H_0), then

$$T \to \chi^2_f \text{ in distribution} \tag{3.18}$$

Therefore, the test described in (3.17) rejects H_0 whenever T exceeds the critical value of χ^2_f, taking into consideration a significance level $1-p$, where p is also often referred to as the asymptotic level and $1-p$ the probability of false alarm.

Let us then address the formulation of Ξ. Note from (3.12) that Ξ can be written as

$$\Xi = [M]_C - (1+\omega)[M]_{C,A}H^H - (1+\omega)H[M]_{A,C} + (1+\omega)^2 H[M]_A H^H \tag{3.19}$$

where $[M]_C$ is the covariance matrix of $\text{vec}(C)$, $[M]_A$ is the covariance matrix of $\text{vec}(A)$, and $[M]_{Q,R}$ is the cross-covariance matrix between Q and R.

Note from (3.19) that in order to construct the test, it is necessary to derive sixth and eighth order moment matrices, what could significantly increase the complexity of the former. Nevertheless, assuming that they both exist and that the moment structure of our population is the same as that of an elliptical distribution up to the eight-order moments [90], then $[M]_4 = (1+\omega)N_4$, $[M]_6 = (1+\eta)N_6$ and $[M_8] = (1+\theta)N_8$, with η, θ and ω, being functions of the characteristic function generator. Furthermore it is possible to write (see (3.8))

$$[M]_C = (1+\theta)(1+\omega)^2(N_4^T \otimes N_4) + \theta(1+\omega)^2 \text{vec}(N_4)\text{vec}(N_4)^T \tag{3.20}$$

$$[M]_{C,A} = (1+\eta)\sum_i (e_i \otimes I_{m^3}) N_6 (e_i \otimes I_{m^2}) - (1+\omega)\text{vec}(N_4)\text{vec}(I_m)^T \tag{3.21}$$

where e_i denotes the ith column of the identity matrix I_m, and

$$[M]_A = (1+\omega)(I_m \otimes I_m) + \omega\left(\text{vec}(I_m)\text{vec}(I_m)^T\right) \tag{3.22}$$

In order to conclude the derivation of the test, the only point missing is to specify a consistent estimator of the generalised inverse of Φ. Note that specifying $\hat{\omega}$, $\hat{\eta}$, $\hat{\theta}$ as consistent estimators of ω, η and θ, respectively, is a sufficient condition to achieve this goal. A consistent estimator of ω is directly obtained from (3.14) and is given by

$$\hat{\omega} = \frac{1}{nm(m+1)} \sum_{i=1}^{n} \left[k_i^H \widehat{[M]}^{-1} k_i \right]^2 \tag{3.23}$$

Analogously, it can be shown that

$$\hat{\eta} = \frac{1}{nm(m+1)(m+2)} \sum_{i=1}^{n} \left[k_i^H \widehat{[M]}^{-1} k_i \right]^3 \tag{3.24}$$

and

$$\hat{\theta} = \frac{1}{nm(m+1)(m+2)(m+3)} \sum_{i=1}^{n} \left[k_i^H \widehat{[M]}^{-1} k_i \right]^4 \tag{3.25}$$

Summarising, the proposed framework for the complex elliptical symmetry starts with the estimation of (3.23), (3.24) and (3.25). Next, (3.20), (3.21) and (3.22) are calculated and consequently, (3.19) is derived. Then (3.16) is used along with (3.15) into (3.17) and the test is finally finished. The degrees of freedom of the test is equal to the rank of Φ [90] and is given by (see Appendix C)

$$f = m^2 + \frac{m(m-1)(m^2+19m+6)}{24} - 1 \tag{3.26}$$

Note that for $m = 3$, (3.26) reduces to $f = 26$.

3.4 Performance Analysis

In order to access the performance and robustness of the proposed test, simulated data, data from the P-band airborne dataset acquired by the Office National d'Études et de Recherches Aérospatiales (ONERA) over the French Guiana in 2009 in the frame of the European Space Agency campaign TropiSAR and a RAMSES X-band image acquired over Brétigny, France (see Appendix E) are taken into consideration.

3.4.1 Synthetic Data Analysis

The synthetic data used in the present analysis is divided into 9 regions, each containing 100 x 100 samples of a specific type of heterogeneous clutter. With the exception of the first, assumed Gaussian and the last assumed a polarization dependent model, all others are modelled as SIRVs (see (E.2)), with different parameters. Since the probability density function of the texture random variable is not explicitly specified by the model, with no loss of generality, we generated the synthetic dataset assuming it to have a Gamma distribution. The shape and scale parameters of the Gamma distribution that characterises the texture random variable for each region are such that their mean are fixed and set to 1 and the their variances are given as in Figure 3.1.

Once the Gamma distribution is parameterized for each region c, a simulated texture vector $\tilde{\boldsymbol{\tau}}^c$, $2 \leq c \leq 8$ is randomly generated. Afterwards, a complex normal distributed

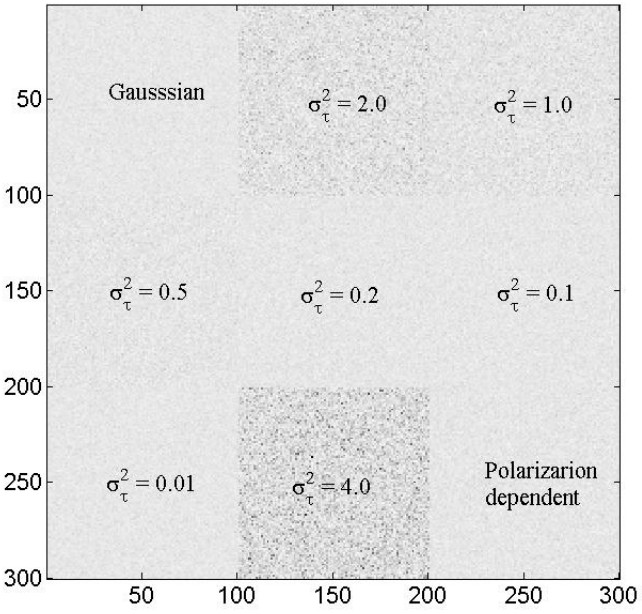

Figure 3.1: Synthetic data span with an indicative of the variance of Gamma distribution that characterises the texture random variable for each region.

random vector $\tilde{\mathbf{z}}$, i.e., $\tilde{\mathbf{z}}^c \sim CN(\mathbf{0}, \mathbf{I})$ is generated. Finally, the simulated observation vector for each region is then given by

$$\tilde{\mathbf{k}}^c = [\mathbf{M}]^{\mathbf{1/2}} \sqrt{\tilde{\boldsymbol{\tau}}^c} \cdot \tilde{\mathbf{z}}^c \tag{3.27}$$

where $[M]$ is the speckle covariance matrix, kept the same for all regions and given by

$$[M]^{1/2} = \begin{bmatrix} 0.2236 & 0 & 0.5477 \\ 0.2236 & 0.3873 & 0.5477j \\ 0 & -0.3873j & 0 \end{bmatrix} \tag{3.28}$$

where $j = \sqrt{-1}$ is the imaginary unit. According to [98] this covariance matrix describes an heterogeneous clutter composed by 60% of quarter wave, 30% of helix left screw and 10% of dipole, with entropy equal to 0.8.

A key point in the analysis of statistical tests performance is the choice of the set of samples (size and location within the data) used in the derivation of their stochastic properties. Since the synthetic data used in the present study is composed by homogeneous regions, a sliding window approach is sufficient for the definition of the set of samples used. Nevertheless the size of this sliding window can impact directly in the performance of the test, either if it is underestimated or overestimated. Figure 3.2 presents in green an over plot of the points where the test indicates non Spherical Symmetric samples with the synthetic data span as background for different sliding window sizes. The asymptotic level p (see (E.13)) was set to 0.99.

Note that the proposed test performance is extremely dependent on the window size. It is evident in Figure 3.2 that the higher the window size, the better the probability of detection (seen in the efficient of the test in rejecting the multiplicative model for the pixels in the "Polarization Dependent" region). Nevertheless, the probability of false alarm can be seen from two perspectives. On the one hand, the amount of isolated false alarms (outliers) decreases as the window size increases, on the other, even though the number of cluster of false alarms pixels remains nearly the same, their size increases with an increase of the window size. The latter points to the dependence of the test performance on the degree of heterogeneity within the set of samples used in the derivation of the statistics.

Therefore, it is possible to conclude that the proposed test has a very good performance in discriminating between SIRV and non SIRV heterogeneous clutter, indicating where the traditional product model (polarization independent texture) fails. Nevertheless, depending on the degree of non-stationarity of the samples used in the test, it also rejects the models, what can be better seen in the boarders of a few regions on the dataset. It is important to highlight that it is not mandatory that the test will fail when samples from different SIRVs models are used to extract the statistics. If that was the case, all the boarders within the synthetic dataset would have failing pixels and yet just the boarders of a few regions present this behaviour.

This assertion opens an interesting venue for discussion, the performance of the test under mixture models. Its is possible to conclude from the achieved results that such performance is a function of the heterogeneity degree within the dataset used to derive the test statistics. Therefore, if the mixed models are close to each other, then the derived test is able to correctly identify them as being SIRVs. Nevertheless, if the probabilistic models are too different from each other the text indicates a departure from the Spherically Invariant Random Vector model.

The test performance is also verified as a function of the confidence level p. Analogously, Figure 3.3 presents in green an over plot of the points where the test indicates non Spherical Symmetric samples with the synthetic data span as background for different asymptotic levels p. The window size was chosen to be 23×23. Note that the probability of detection, as defined above, remains nearly unchanged, while the probability of false alarm increases considerably as the asymptotic level decreases.

For the sake of completeness, we verify the consistency of the test as a function of the window size. Figure 3.4 shows the normalized fitted chi-squared distribution to the histogram of the test performed (see (3.17)), using the sliding window approach (window sizes 7×7, 15×15 and 23×23) and taking into consideration the region where the pixels present a Gamma distribution with variance $\sigma_\tau^2 = 0.5$. It is important to highlight that the integral of any pdf over the range $[-\infty, \infty]$ should always be equal to 1, nevertheless, since we are mainly interested in the goodness of fit of the test, with no loss of generality, we chose to present the normalized version of the given curves.

Note from Figure 3.4 that the chi-squared distribution with degrees of freedom given by (3.26) does not provide an overall satisfactory goodness of fit for the proposed Spherical

Symmetry test, despite of the chosen window size. Nevertheless, the goodness of fit of the tail distribution (more important in our analysis) of the derived test presented in (3.17) for window sizes 15×15 and 23×23 is remarkable, in accordance with the theory derived in the previous section. Note further that such goodness of fit of the tail distribution is not verified for small window sizes, what can be seen in the curve corresponding to a 7×7 window size. This points to another indication of the test performance dependence to the window size. Finally, it is important to highlight once again that the proposed Wald test distribution is asymptotically chi-squared, therefore, for each window size, the test distribution will most likely present a departure from the chi-squared one, as a function of the number of samples being used in the statistics derivation.

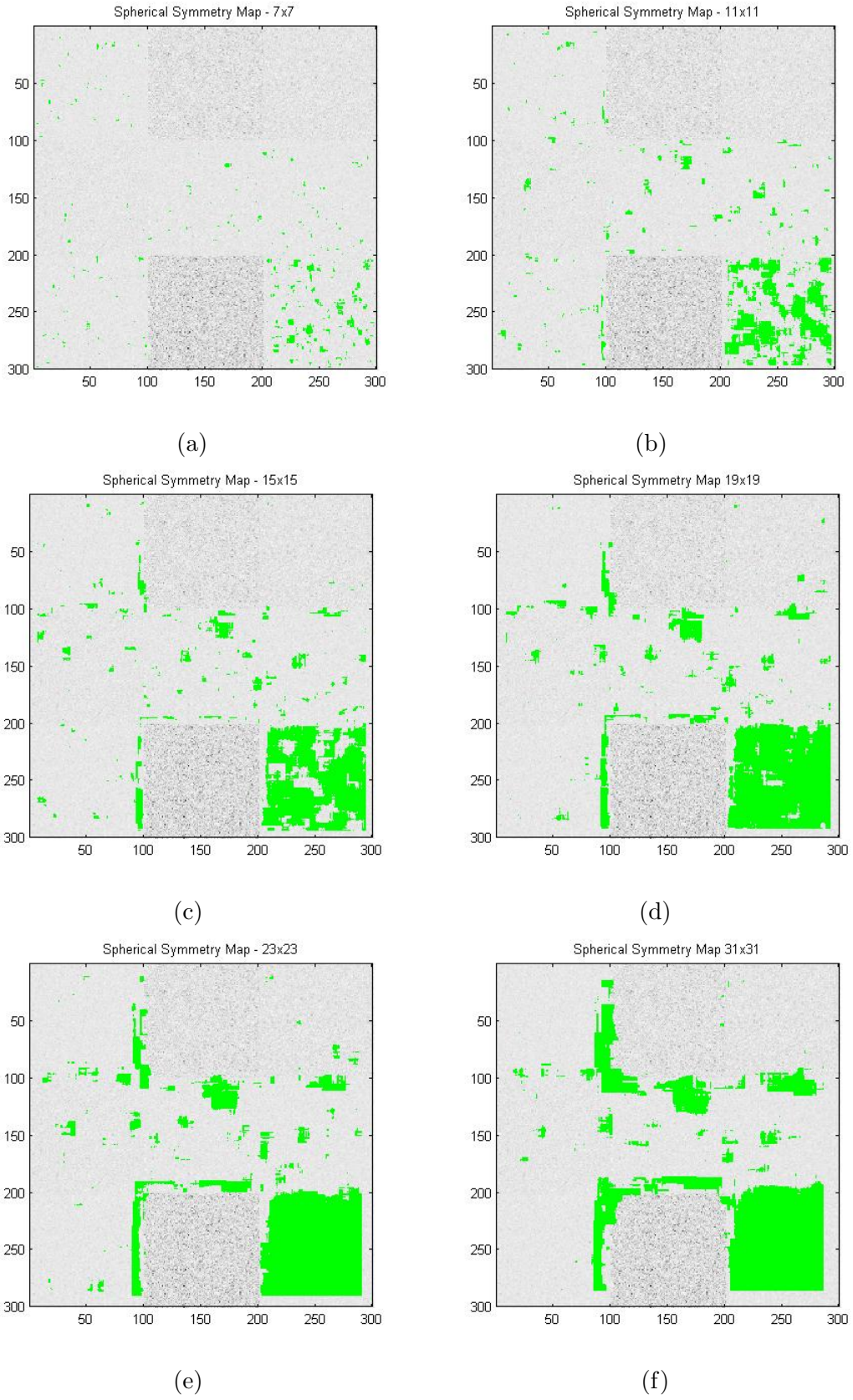

(a) (b) (c) (d) (e) (f)

Figure 3.2: Rejected samples by the proposed test in green backgrounded by the synthetic data span. Test repeated with different window sizes: (a) 7×7; (b) 11×11; (c) 15×15; (d) 19×19; (e) 23×23; (f) 31×31.

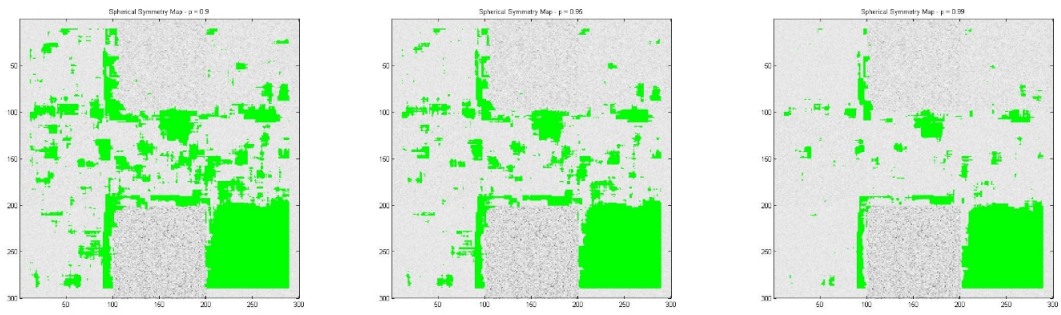

(a) (b) (c)

Figure 3.3: Rejected samples by the proposed test in green backgrounded by the synthetic data span. Test repeated with different asymptotic levels p: (a) 90%; (b) 95%; (c) 99%.

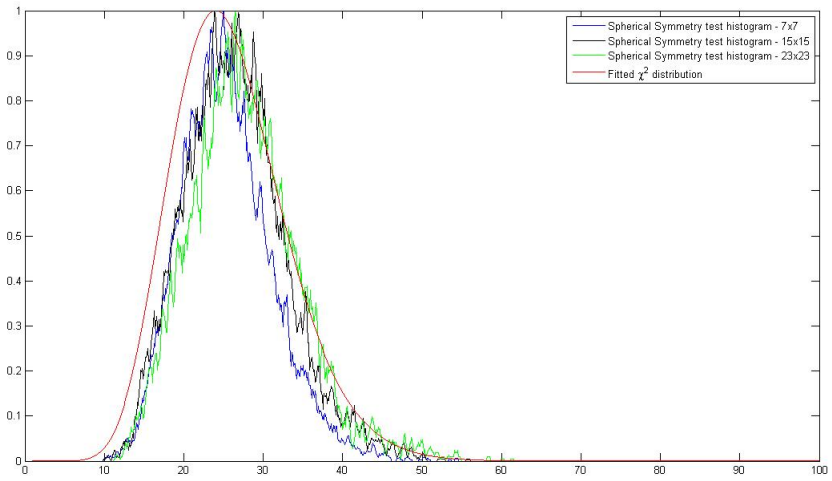

Figure 3.4: Fitted chi-squared distribution (red) to the histogram of the test performed with different window sizes: 7×7 (blue), 15×15 (black) and 23×23 (green). It was taken into consideration the region with Gamma distribution and variance $\sigma_\tau^2 = 0.5$.

3.4.2 Real Data Analysis

Once the test is validated with synthetic data, we carried on with our investigation using real data. More precisely, in the present work we take into consideration data from the P-band airborne dataset acquired by the Office National d'Études et de Recherches Aérospatiales (ONERA) over the French Guiana in 2009 in the frame of the European Space Agency campaign TropiSAR, characterising an area mainly composed by distributed targets and a RAMSES X-band image acquired over Brétigny, France with strong deterministic targets. More details of the datasets employed in the analysis can be found in Appendix E.

When working with real data, the set of samples used in the test can be extracted either by using a sliding window, or from classes previously segmented with the use of an additional algorithm. In the present work we choose to apply the test on a sliding window configuration, to avoid any constraint (or bias) that could emerge from the use of the former. The sliding window size, in turn, is a constant concern in SAR community since high values decrease considerably the system spatial resolution and may eventually introduce bias in the estimation of a few parameters. Many authors raised the question of what would be the optimal window size for several different applications, e.g. [58, 65]. In the previous section the tradeoffs in the proposed statistical test performance, concerning the sliding window size, were discussed. The size of the sliding window was then chosen to be 15×15, which presented a good performance regarding the probability of detection and probability of false alarm and is in accordance to what is described as necessary by other authors when applying many SAR algorithms [58, 65, 82].

The analysis starts by verifying the consistency of the test with respect to temporal datasets. Before applying the proposed test, it is first necessary to verify if the dataset is coherent, i.e., if there is no significant statistical decorrelation between the information acquired in different moments (see (2.34)). Four images acquired by the Office National d'Études et de Recherches Aérospatiales (ONERA) over the same area on the ground (in French Guiana), by the same P-band airborne sensor flying in the same trajectory were taken into consideration. The time interval between each acquisition with respect to the first (taken as reference) is 2, 4 and 7 days, respectively. More details on the dataset are provided in Appendix E.

Figure 3.5 presents the magnitude of the coherence of each temporal image calculated with respect to the first one. It is important to highlight that this preliminary analysis is done merely in a qualitative, rather then a quantitative, sense. Therefore, only the first component of the target vector, written in Pauli basis (see (2.30)) is taken into consideration. Note that the temporal datasets are coherent with respect to one another. This result is in accordance to what was reported in [32].

Next, we perform the proposed clutter stochastic model testing procedure on each of the aforementioned polarimetric temporal data set. The result is presented in Figure 3.6. Note that the test is consistent with respect to temporal coherent datasets. The average of matching results from the test is 83.73%, i.e. the average number of pixels in each image

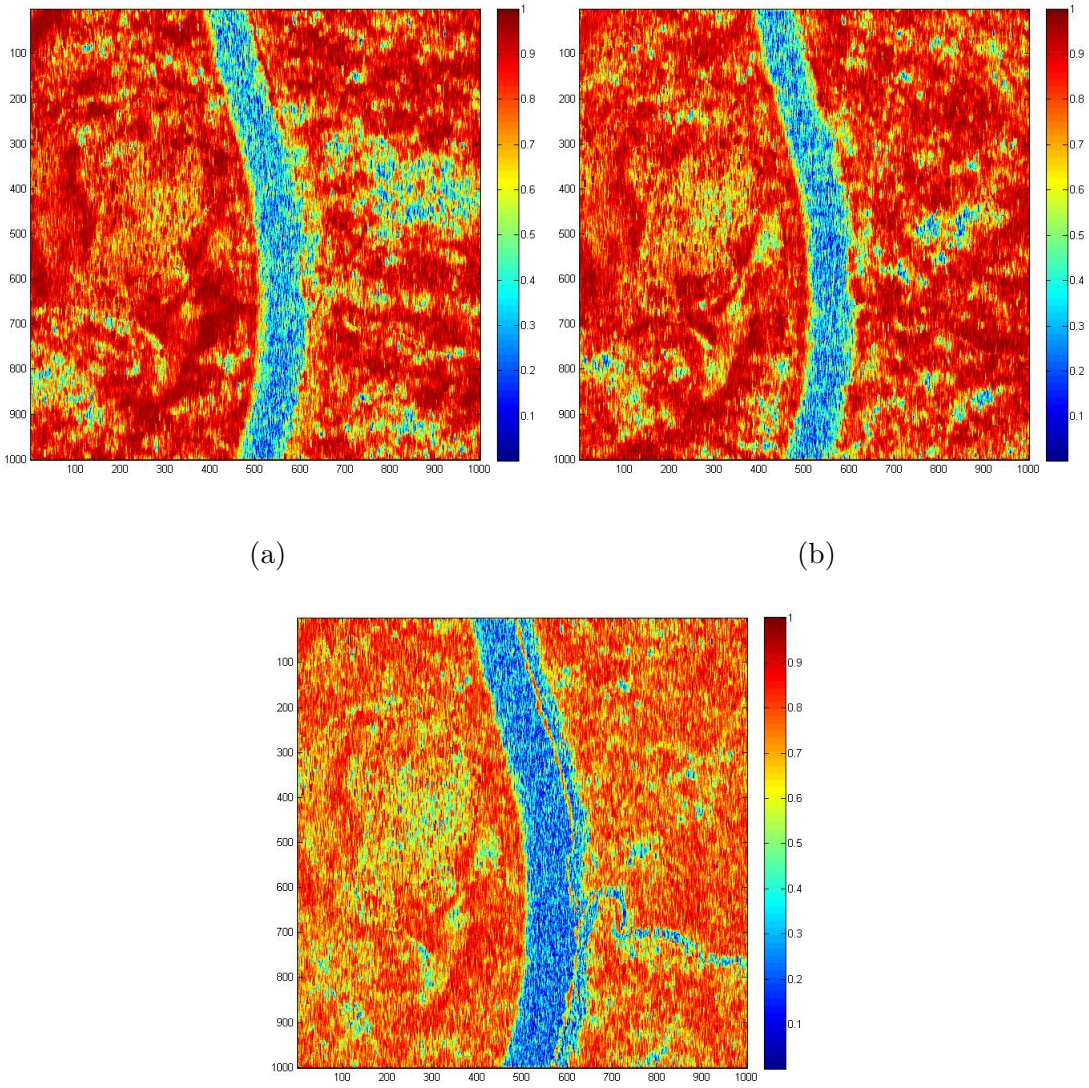

Figure 3.5: Temporal analysis of the Spherical Symmetry test: (a) coherence between the reference image and image 2; (b) coherence between the reference image and image 3; (c) coherence between the reference image and image 4.

whose test outcome is the same as the outcome taking into consideration the reference image is 83.73%. Therefore, different coherent temporal polarimetric data sets provide nearly the same test result.

As an additional tool for the remainder of the analysis, a statistical classification algorithm is still employed to segment the scene under study into 8 different classes. For that purpose, the statistical classifier developed for highly textured POLSAR data [41] was employed. Un-

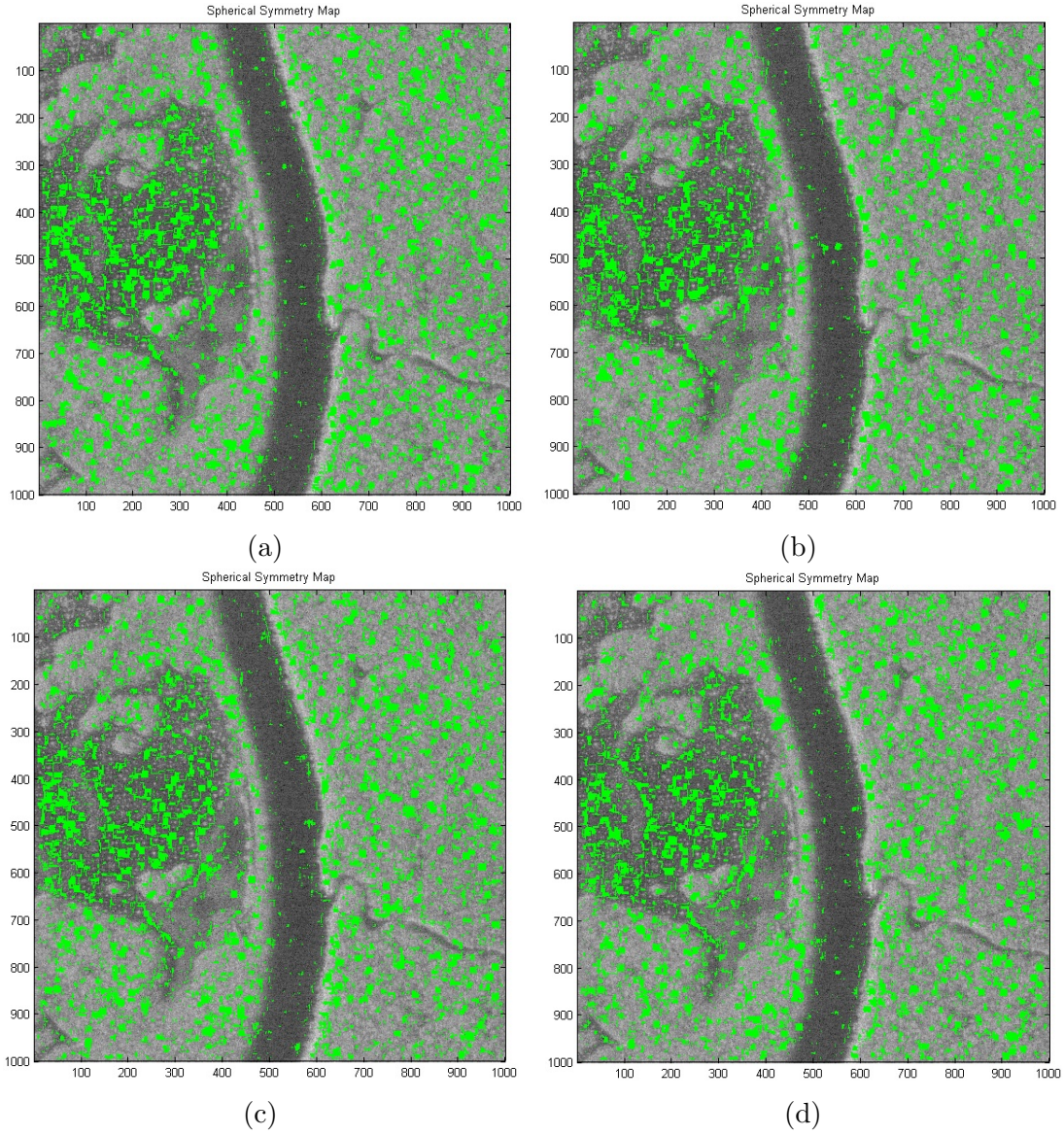

Figure 3.6: Temporal analysis of the Spherical Symmetry test: (a) test output performed on the reference image; (b) test output performed on the image 2; (c) test output performed on the image 3; (d) test output performed on the image 4.

like the classical H/α unsupervised classification [18], that assumes Gaussian homogeneous clutter and therefore relies on the Sample Covariance Matrix (SCM) estimation, classical mean and Wishart distance, the Non-Gaussian heterogeneous clutter is taken into account. More details on this algorithm is presented in Chapter 6, where its contribution is more noticed.

Let us first address the TropiSAR dataset. Figure 3.7 presents the region under study of the referred area (different from the one use in the temporal analysis due to its higher heterogeneity), the classification algorithm output and the spherical symmetry map where,

in green, are indicated non Spherical Symmetric samples backgrounded by the dataset span.

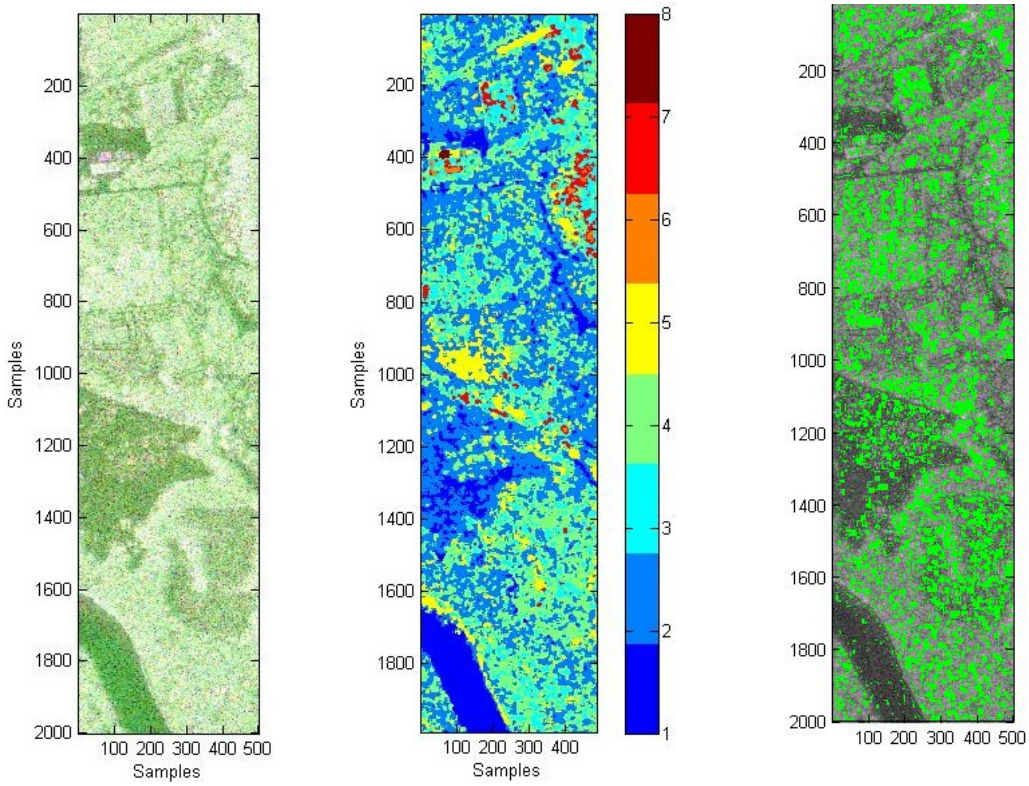

Figure 3.7: French Guiana area under study: (a) RGB image, Red (HH+VV), Green (HV), Blue (HH-VV); (b) statistical classification algorithm output; (c) spherical symmetry map.

Note that the river constitutes Class 1, as well as some presumable floated areas while Class 8 is mainly represented by a small region probably with some man made structure. Using an H/α feature space (Figure 3.8), it is possible to perceive the high degree of heterogeneity within the data which contains pixels that can be classified as Volume, Double-Bounce and Surface type of scatters [19]. Likewise the statistical classification algorithm, more details on the H/α feature space are given in Chapter 4.

Note that the amount of pixels that fail the proposed test in such type of dataset is not negligible (30%). This indicates that a considerable portion of the data does not fit the Spherically Invariant Random Vector model (product model). Furthermore, note that the test is able to correctly identify regions with high indexes of non-stationarity, more accentuated in borders between classes, as can be clearly seen in what seems to be the river shore. The intervals $[200:300, 200:300]$ and $[400:500, 400:600]$ of the dataset, both composed by pixels from several different classes, also present a high concentration of samples that fail the test and therefore do not fit the product model. The percentage of rejected pixels for each class is given in Table 3.1.

Note that Classes 3, 7 and 8 are not very good representatives of the product model, while on the other hand, classes 1, 2, 4, 5 and 6 are well described as SIRVs. Further investigation

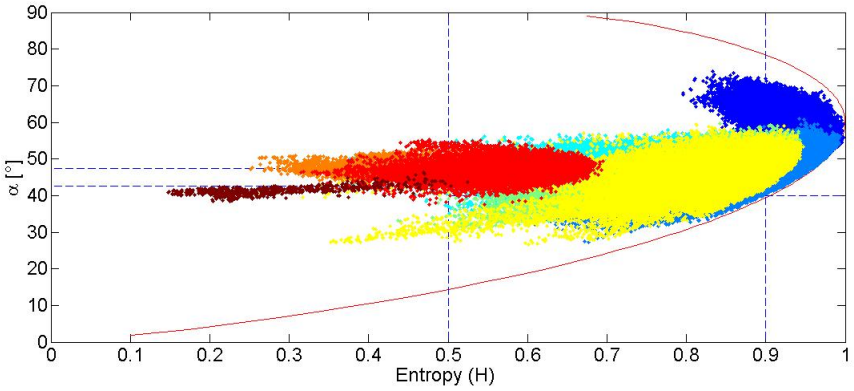

Figure 3.8: French Guiana area under study: H/α feature space.

Table 3.1: Percentage of non spherical symmetric pixels per class in French Guiana area under study.

Class	Percentage of non spherical symmetric pixels
1	13.76%
2	25.46%
3	45.30%
4	33.20%
5	32.19%
6	30.99%
7	48.76%
8	55.12%

of the data revealed that most of the pixels declared non spherical symmetric by the proposed test (98.62%) had their statistic derived from a set of samples containing pixels from different classes, more precisely, 3 (38.79%) or 4 (30.51%) classes. This indicates for the importance in considering the high heterogeneity of the data, specially under forested scenarios, in the derivation of SAR image processing algorithms. The latter becomes critical if a sliding window approach is directly adopted with no additional step to avoid the contamination of pixels with different characteristics, compromising the considered statistical model goodness of fit.

Let us now turn our attention to the RAMSES X-band image acquired over Brétigny, France, which characterises an urban area. Analogously, Figure 3.9 presents the referred area, the classification algorithm output and the spherical symmetry map where, in green, are indicated non Spherical Symmetric samples backgrounded by the dataset span.

Note that, unlike the TropiSAR dataset, the RAMSES X-band image depicts a more homogeneous region, therefore the amount of non spherical symmetric pixels is considerably less than the former, accounting for just 18% of the pixels in the image. On the other hand, likewise the TropiSAR dataset analysis, most of the pixels declared non spherical symmetric by the proposed test (62.12%) had their statistic derived from a set of samples containing

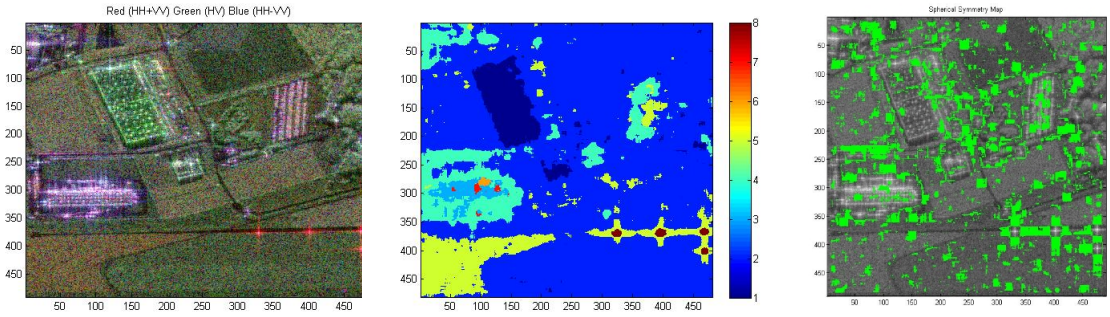

(a) (b) (c)

Figure 3.9: RAMSES X-band image acquired over Brétigny, France: (a) RGB image, Red (HH+VV), Green (HV), Blue (HH-VV); (b) statistical classification algorithm output; (c) spherical symmetry map.

pixels from different classes. Furthermore, it is important to highlight the correctness of the test in indicating the regions where the trihedrals are present as Spherical Symmetric pixels since we can characterise them as a sum of a deterministic signal with SIRV clutters, being straightforward to state that the result also fits a SIRV model. Nevertheless, once again, the high heterogeneity of the samples used in deriving the statistics seems to be the cause of the surroundings of the regions where the trihedrals are located failure to the test and, consequently, failure to the product model.

3.5 Remarks

The analysis with real data (see figures (3.7) and (3.9)) showed that the rate of pixels that fail the proposed test is not negligible in specific types of scenarios. The forested area investigated here presented 30% of pixels that do not fit the product model. It is important to highlight that the applied classification used as an additional tool to better illustrate the regions where the model fails was unsupervised, therefore the correspondence to ground truth may not be strictly exact. It is common sense in SAR community that the evaluation of unsupervised classification is a challenging task, due to the high degree of complexity in relating, physically and unambiguously, classes to the ground truth data [35], specially in tropical forest scenarios where ground truth is scarce and generally incomplete due to the difficult in accessing and performing in situ measurements. Furthermore, highly heterogeneous clutters rarely present the same statistic behaviour within another, making it difficult to precisely quantify the amount of pixels that will fail the model.

Even though the lack of precise ground truth can limit the assertion of what is causing the product model to fail, the main objective of the present analysis was to show that by proving the correctness of test (by means of a detailed mathematical derivation and an analysis with a synthetic dataset) and by applying it to real datasets with different sensor characteristics, we could be able to indicate that the amount of pixels that fail the model can be non negligible,

requiring extra attention in their analysis.

In short, a considerable portion of high heterogeneous data may not fit the Spherically Invariant Random Vector model (product model). Therefore, traditional detection and classification algorithms developed based on the latter become sub-optimal when applied in such kind of regions, highlighting for the need of either updating the model to one that associates an individual texture variable with each polarimetric channel [35], or the development of model independent algorithms, like the Independent Component Analysis (ICA), proposed in [3].

The former, introduces a high degree of complexity in modelling PolSAR data and, consequently in deriving proper algorithms suited for such models. Furthermore, providing unique models when multi-texture assumption is taken into consideration is a challenge very difficult to came across. The ICA, on the other hand, being a blind source separation technique, based on higher order statistical moments, aims in recovering statistical independent sources without having any physical background of the mixing process [48]. Therefore, it is a model independent strategy to analyse the behaviour of non-Gaussian heterogeneous clutters (inherent to high resolution SAR systems) which proved itself very useful and introduces an alternative way of physically interpreting a polarimetric SAR image. In the next chapter this technique is further addressed.

Chapter 4

Incoherent Target Decomposition

Sommaire

Polarimetric target decomposition is one of the most powerful and widespread tools for PolSAR image interpretation. The analysis of the interaction between the illuminated area and the transmitted waveform, to each polarimetric state of the latter, allows for a better prediction of the basic scattering mechanisms present on the scene, and to more efficiently propose classification, detection and geophysical parameter inversion algorithms.

More specifically, Incoherent target decomposition (ICTD) theory assumes that the scattering process in most natural media is a combination of coherent speckle noise and random vector scattering effects. Therefore, not only a statistical analysis is often required, but also it is a common practise to associate to the imaging cell the concept of average or dominant scattering mechanisms [18].

ICTD algorithms can be split in two stages: the decomposition of an image pixel into basic target vectors and the correct retrieval of quantitative information from them (parametrization). Concerning the latter, Cloude and Pottier's parameters (entropy, alpha and anisotropy) [19] and Touzi's target scattering vector model [98] are the most employed ones, whose usefulness have already been demonstrated by several authors. Regarding the former, the association of the three most dominant scatters in an image cell to the eigenvectors of the coherence/covariance matrix of the data is so widespread in the PolSAR community that it is often mistaken as the only alternative for that purpose. In the present chapter we first describe the aforementioned parametrization methods, then we present the Eigenvector based ICTD, highlighting the constraints inherent to such technique and finally introduce the Independent Component Analysis as an alternative ICTD method to be employed in conjunction with the latter in an attempt to better interpret PolSAR data of distributed scatters.

4.1 ICTD Parametrization

Parameterizing a given target vector (defined in (2.30)) means associating to the latter physical parameters related to its shape/composition that enables its classification as one of the already known scattering mechanisms or natural phenomena. Such parameters are derived based on the electromagnetic behaviour of the backscattered wave, considering each polarization state of the transmit waveform. In the following, two of the most employed, within the SAR community, parametrization methods are briefly described.

4.1.1 Cloude and Pottier $H/\alpha/\beta$

The Scattering Vector Reduction Theorem proposed by Cloude and Pottier [19] states that for any scattering mechanisms, its target vector can be written as a set of transformations performed in the identity vector [49] as follows

$$\mathbf{k} = |\mathbf{k}| \cdot \begin{bmatrix} e^{j\phi_1} & 0 & 0 \\ 0 & e^{j\phi_2} & 0 \\ 0 & 0 & e^{j\phi_3} \end{bmatrix} \cdot \begin{bmatrix} 1 & 0 & 0 \\ 0 & \cos(\beta) & -\sin(\beta) \\ 0 & \sin(\beta) & \cos(\beta) \end{bmatrix} \cdot \begin{bmatrix} \cos(\alpha) & -\sin(\alpha) & 0 \\ \sin(\alpha) & \cos(\alpha) & 0 \\ 0 & 0 & 1 \end{bmatrix} \cdot \begin{bmatrix} 1 \\ 0 \\ 0 \end{bmatrix} \tag{4.1}$$

The reduced form of the target vector is given as

$$\mathbf{k} = |\mathbf{k}| \cdot \begin{bmatrix} \cos(\alpha)e^{j\phi_1} \\ \sin(\alpha)\cos(\beta)e^{j\phi_2} \\ \sin(\alpha)\sin(\beta)e^{j\phi_3} \end{bmatrix} \tag{4.2}$$

where the angles ϕ_i, $i = 1, 2, 3$ represent phase relations with no relevant physical meaning reported up to now and the angles β and α account for the scatter orientation with respect to the radar line of sight and its natural phenomenology, respectively. The α angle is a key parameter if the scatter physical behaviour is under investigation, ranging from an isotropic surface ($\alpha = 0°$) to double bounce type of targets ($\alpha = 90°$), passing trough oriented dipole ($\alpha = 45°$).

The referred decomposition presents ambiguity when discriminating between some specific scatters. In [27] the authors highlight that some targets with the same scattering type parameter can not be distinguished using the Cloude and Pottier parameterization. This is the case of helix and dihedral, for example. Therefore, the authors propose an analysis in an alternative orthonormal basis formed by a sphere and a pair of helices to circumvent the problem. The ambiguities related to the parametrization are not addressed in the present work. For that purpose the reader is advised to go to [27].

Additionally, other concerns have been raised regarding the robustness of the aforementioned parametrization which are mainly related to the roll-variance of the β angle and the inability to describe asymmetric type of targets [98]. Nevertheless, in the present work, these concerns are also neglected with no loss of generality since our main interest lies in the target classification scheme originated from the referred parametrization (see Section 4.2.1), which does not take into account the β angle [18].

4.1.2 Touzi Target Scattering Vector Model

The target scattering vector model derived in [98] based on the Kennaugh-Huynen decomposition is given, for both symmetric and asymmetric targets, by

$$\mathbf{k} = m|\mathbf{k}|_m \cdot e^{j\phi_s} \cdot \begin{bmatrix} 1 & 0 & 0 \\ 0 & \cos(2\psi) & -\sin(2\psi) \\ 0 & \sin(2\psi) & \cos(2\psi) \end{bmatrix} \cdot \begin{bmatrix} \cos(\alpha_s)\cos(2\tau_m) \\ \sin(\alpha_s)e^{j\phi_{\alpha_s}} \\ -j\cos(\alpha_s)\sin(2\tau_m) \end{bmatrix} \tag{4.3}$$

where each coherent scatter can be represented by four unique and roll-invariant parameters, τ_m, α_s, ϕ_{α_s} and m and by two roll variant parameters ϕ_s and ψ. In [6], Bombrun made a detailed investigation of the ambiguities in (4.3) and came up with the following relations

$$\begin{aligned} \mathbf{k}(\tau_m, \alpha_s, \phi_{\alpha_s}, m, \phi_s, \psi) &= \mathbf{k}(-\tau_m, \alpha_s, \phi_{\alpha_s} \pm \pi, m, \phi_s, \psi \pm \frac{\pi}{2}) \\ &= \mathbf{k}(-\tau_m, -\alpha_s, \phi_{\alpha_s}, m, \phi_s, \psi \pm \frac{\pi}{2}) \end{aligned} \tag{4.4}$$

In (4.3), target helicity, τ_m, is used for identifying its symmetric nature and is defined in the interval $[-\pi/4,\ \pi/4]$. The parameter α_s, defined in the interval $[0,\ \pi/2]$ represents the magnitude of the symmetric scattering, while ϕ_{α_s}, ranging between $[-\pi/2,\ \pi/2]$, its phase. In [98] it is shown that α_s is identical to Cloude and Pottier scattering type parameter for a low entropy symmetric target, i.e., target having an axis of symmetry in the plane orthogonal to the radar line of sight direction. These three parameters allows for a complete and an unambiguous description of coherent scatters while ψ determines the target orientation angle, m is a measure of the maximum amplitude return and the phase ϕ_s is investigated only in interferometric applications.

In his work, with the aid of the Poincaré sphere, Touzi enumerates a set of canonical scattering mechanisms and their corresponding τ_m, α_s, ϕ_{α_s} parameters. Figure 4.1 illustrates a few of the scattering mechanisms parameterized with the aforementioned method.

As in Cloude and Pottier decomposition, Touzi target vector scattering model also presents ambiguity for some specific scatters. While in [27] the authors proposed an analysis in an alternative orthonormal basis to circumvent the problem in Cloude and Pottier parametrization, in Touzi's decomposition the ambiguity problem seems slightly more complex since it involves the evaluation of the orientation angle ψ.

In order to derive the roll invariant parameters τ_m, α_s and ϕ_{α_s}, responsible for an unambiguous description of the target, the orientation angle has to be first derived and removed, an operation referred to as "desying" in [8]. This procedure has been addressed in [8] where the authors proposed a new method for estimating ψ and compared its performance with the method proposed by Krogager based on the phase difference between right-right and left-left circular polarizations of the scattering matrix [53]. The referred method is given by

$$\psi = \frac{1}{2}\arctan\left(\frac{2\Re\{(S_{HH}^* + S_{VV}^*)S_{HV}\}}{\Re\{(S_{HH}^* + S_{VV}^*)(S_{HH} - S_{VV})\}}\right) \tag{4.5}$$

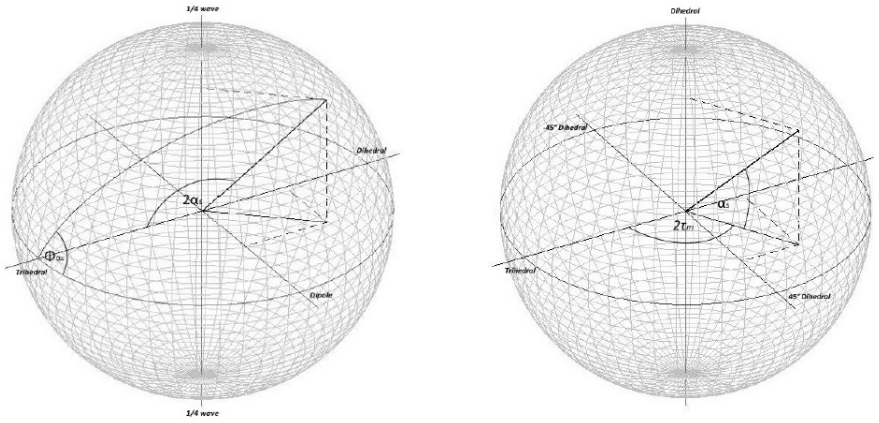

(a) (b)

Figure 4.1: Poincaré sphere representation of Touzi parameters and scattering mechanisms parameterized considering: (a) $\tau_{=}0$, (b) $\phi_{\alpha_s} = 0$.

The authors in [8] concluded that unlike the method proposed by Krogager, theirs provide an unbiased estimation of the target's orientation angle and should be used for its characterisation. Nevertheless, the procedure described does not treat ambiguities that appears for some special targets. In Appendix D, we better address this issue but it is worth pointing out that it is not the intention of the authors here to propose a solution for the aforementioned ambiguity problem, but rather to show the importance in the appropriate implementation of the parametrization algorithm and evaluation of the parameters derived.

4.2 Target vectors estimation

Prior to the parametrization, it is first necessary to estimate the scattering vectors from the given data. The assumption that the scattering process in most natural media is a combination of coherent speckle noise and random vector scattering effects leads to the need of a stochastic approach for that purpose. Furthermore, the concept of average or dominant scattering mechanisms has to be associated to each imaging cell [19], since multiple targets contribute to the backscatter electromagnetic signature of a given pixel (see (2.17)).

4.2.1 Eigenvector based ICTD

The Eigenvector based approach employs a three-level Bernoulli statistical model to estimate average target scatters within the data. More precisely, it relies on the diagonalisation of the Hermitian, semidefinite positive coherence or covariance matrix (see (2.31)) by an unitary similarity transformation [19, 49] given by

$$[M] = [Z][\Lambda][Z]^{-1} \tag{4.6}$$

where $[M]$ is the estimated coherence matrix taking into consideration the pixel neighbours within a sliding window. $[Z]$ is an unitary matrix whose columns are the eigenvectors of $[M]$ and $[\Lambda]$ is the corresponding diagonal eigenvalues matrix.

Such method assumes that each eigenvector represents one of the most dominant deterministic scattering mechanisms within the image cell. Since the coherence matrix is 3×3 (assuming that the reciprocity theorem holds, i.e. $m = 3$), the three scatters that stands out are retrieved. Many authors justify the usage of the Eigenvectors approach claiming that they form an orthogonal basis, and that the diagonalisation performed on the coherence matrix indicates that the retrieved sources are uncorrelated, what for Gaussian clutter assumption also means independence [49]. The drawback of this kind of method emerges when the clutter is not Gaussian or not composed by orthogonal mechanisms, situations where the performance of the algorithm could be compromised. As reported in Chapter 5, under the aforementioned scenarios, both characteristics can in fact compromise the correct interpretation of the scene under analysis.

The contribution of each mechanism to the total backscatter phenomenology is given by its corresponding eigenvalue. The entropy H is a parameter introduced to measure how much, in terms of statistics, the scatters are mixed. In other words, it measures the degree of randomness within the image cell. It is a function of the eigenvalues λ_i, $i = 1, 2, 3$ (representing the corresponding contribution from each scatter), written as

$$H = \sum_{1}^{3} -P_i \log_3 P_i \tag{4.7}$$

where $P_i = \lambda_i/(\lambda_1 + \lambda_2 + \lambda_3)$. It is important to note that the entropy, being a function only of the eigenvalues of the coherence matrix is roll-invariant and basis invariant.

The combined use of the Eigenvector approach with Cloude and Pottier's parametrization gave rise to one of the most employed and most traditional classification schemes in PolSAR data analysis, the H/α feature space [19]. Low entropy values indicate that a dominant scatter is mainly responsible for the given polarimetric signature, while high values (close to 1) point to the existence of multiple scattering mechanisms within the image cell equally strong, suggesting that there is not a single one that stands out among the others. The α angle is extracted from the eigenvectors of the coherence matrix and, as previously mentioned, represents the physical behaviour of the scatter. Each eigenvector correspond to a scattering mechanism within the image cell and therefore each one will provide a different α angle. The authors in [19] state that the best estimate of such parameter to represent the image cell is an weighted average based on the eigenvalues of the coherence matrix. In the next section we take a closer look on this classification scheme.

H/α feature space

The H/α plane is a standard tool for PolSAR image analysis serving as basis for many detection, classification and geophysical parameters inversion algorithms. The H/α classifi-

cation introduces an extra step in the characterization of the scattering mechanisms within a resolution cell. After decomposing an image pixel into basic target vectors and correctly retrieving quantitative information from them (parametrization), it allows the association of the estimated parameters to natural phenomena.

Once the α angle is estimated for each mechanism, a weighted average based on the contribution of each scatter (eigenvalue) is calculated. The resultant average α along with the entropy H derived for each pixel are plotted in a plane. Based on the polarimetric behaviour of known type of natural phenomena, Cloude and Pottier proposed linear boundaries to classify an image cell based on its H and α values. The outcome of this clustering is a feature space consisting of 9 classes divided in low, medium and high entropy, and surface, dipole and double bounce type of targets, depicted in Figure 4.2.

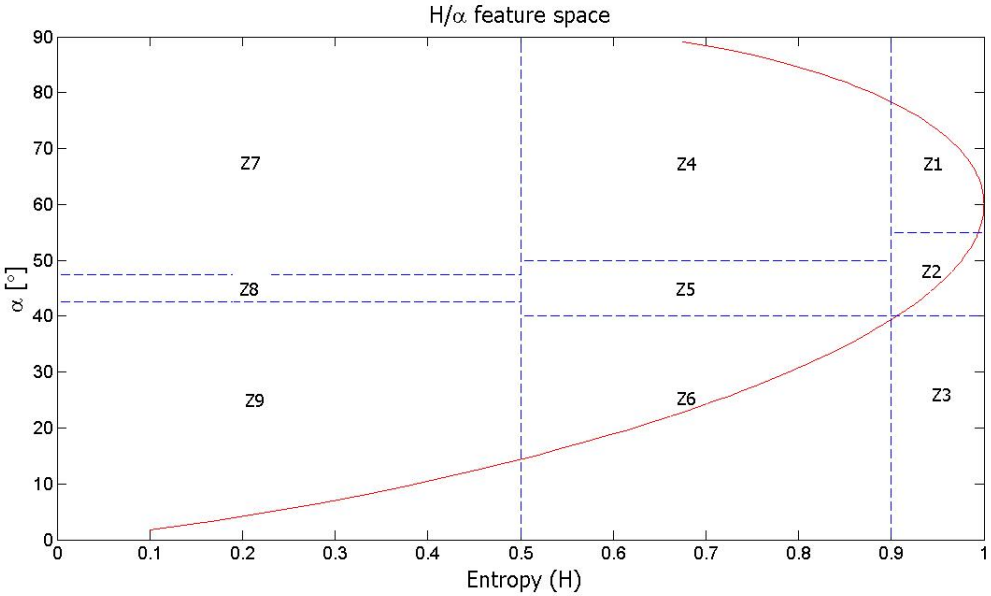

Figure 4.2: H/α feature space.

Many works are based on such method, from geophysical parameters inversion algorithms (in varied regions from the globe) to detection and classification algorithms. Having a remarkable correspondence to ground truth, the usage of this unsupervised technique has had very few improvements since its conception. Nevertheless, there is an important remark still uncovered related to this method. The orthogonality constraint of the eigenvectors of the coherence matrix generates unfeasible regions in the plane, reducing the feasible H/α pairs that can be represented in the feature space. It is important to highlight that these regions are mathematically, and not physically, unfeasible.

As reported in [19], this limitation reaches its apex for $H = 1$, when only $\alpha = 60°$ becomes a possible solution that complies with the referred constraint. Nevertheless, it is counter intuitive to believe that when any multiple scatters are equally present in an image cell, necessarily the behaviour of the resultant mechanism has to be the one of double bounce scatters.

The feasible regions boundaries are represented by two curves (also presented in Figure 4.2), calculated as the H/α pair estimated considering the following coherence matrices

$$[M]_I = \begin{bmatrix} 1 & 0 & 0 \\ 0 & m & 0 \\ 0 & 0 & m \end{bmatrix} \quad 0 \leq m \leq 1 \tag{4.8}$$

and

$$[M]_{II} = \begin{cases} \begin{bmatrix} 0 & 0 & 0 \\ 0 & 1 & 0 \\ 0 & 0 & 2m \end{bmatrix} & 0 \leq m \leq 0.5 \\ \begin{bmatrix} 2m-1 & 0 & 0 \\ 0 & 1 & 0 \\ 0 & 0 & 0 \end{bmatrix} & 0.5 \leq m \leq 1 \end{cases} \tag{4.9}$$

The limiting curves on the H/α plane reduce the analysis of high entropy type of targets in a more limiting way than the analysis of low entropy ones. Even though polarimetry is a better suited tool to analyse low entropy type of targets, the ability to correctly estimate the parameters that describe the illuminated scatters is crucial. Therefore, any constraint that prevent this from happening decreases the performance of any classification, detection and geophysical parameter inversion algorithms. Furthermore, when surface type of scatters are addressed, even in low entropy environment the constraint on the estimated average α angle can lead to a misinterpretation of the actual behaviour of the clutter, directly affecting the performance of classification and detection algorithms as well as the validity of many physical models widely used to describe this type of targets. For the sake of completeness, let us verify what kind of theoretical heterogeneous clutter may fall in the aforementioned unfeasible regions that arise when the Eigenvector approach is employed. For that purpose, Touzi target scattering vector model is taken into consideration.

Considering the TSVM parametrization of the canonical scatters presented in the previous section, let us assume that the heterogeneous clutter composition in the scenario under study is 15% dihedral ($\alpha_s = 90°$), 35% dipole ($\alpha_s = 45°$) and 50% cylinder ($\alpha_s = 18°$). Such non-orthogonal symmetric scattering mechanisms may be found in nonurban/forested areas [80, 55]. Since the referred scatters present zero helicity due to their symmetry, Cloude and Pottier average α angle can be extracted directly from Touzi's α_s, and is given, for such clutter, by $\alpha = 38.25°$. The estimated Entropy is $H = 0.9089$. Note that these values of H and α would fall into a non feasible region, if correctly retrieved by the Eigenvector approach. Nevertheless, the orthogonality constraint between the estimated scatters does not enable this from happening. The Eigenvector approach estimates mutually orthogonal but incorrect scattering mechanisms whose H and average α pair will mandatory fall within the boundaries set by the aforementioned limiting curves.

Another evidence that the orthogonality constraint introduced by the Eigenvector approach may compromise the performance of classification algorithms arises when the H/α

feature space is used as a starting point in iterative classification algorithms. Iterative classification algorithms, like the ones proposed in [104, 62], rely on the assumption that pixels with similar statistical behaviour may compose a same cluster (class) even if they reside in different boundaries regions. Therefore, once an initial population is defined (generally the output of the H/α classification), a distance measure based on the stochastic model adopted is taken into consideration to verify if a given pixel is more likely to be part of a new class than its actual one. In many applications it is noticeable the migration of pixels originally classified in zone 6 to zone 2, indicating that pixels in these regions have characteristics that are not well described by neither of phenomena represented by them. This subject is further addressed in Chapter 6.

In [3] a new strategy to polarimetric target decomposition was presented by incorporating the independent component analysis (ICA). The ICA is a blind source separation technique based on higher order statistical moments and cumulants whose utility has already been explored in many different research areas, such as wireless communications, feature extraction and brain imaging applications [48]. The results presented in [3] proved it to be a very promising area in polarimetry, mainly when non-Gaussian heterogeneous clutters (inherent to high resolution SAR systems) are under study. The theoretical potential in estimating similar entropy and first component, when compared to traditional eigenvector decomposition, but rather a second most dominant component independent with respect to the first one and unconstrained by the orthogonality introduces an alternative way of identifying the canonical scattering mechanisms within an image cell and, therefore, of physically interpreting a polarimetric SAR image. The following section describes this method in more detail.

4.2.2 Independent Component Analysis based ICTD

In order to better address the ICA approach to ICTD and highlight the main differences regarding the Eigenvector decomposition, first we shall model the problem from a blind source separation perspective. Let $\mathbf{x}$ be a set of observation vectors, then

$$\mathbf{x} = \mathbf{A}\mathbf{s} \tag{4.10}$$

where $\mathbf{A}$ is the mixing matrix and $\mathbf{s}$ is the mutually independent sources vector. Analogously to Eigenvector decomposition, each column of the estimated mixing matrix $\hat{\mathbf{A}}$ represents one of the most dominant mutually independent target vector present in the observed scene. The estimated sources, $\hat{\mathbf{s}}$, are given by

$$\hat{\mathbf{s}} = \hat{\mathbf{A}}^{-1}\mathbf{x} \tag{4.11}$$

The ICA approach aims, based on higher order statistical moments, in recovering statistical independent sources without having any physical background of the mixing process [23]. Once a stationary set of observed Pauli target vector is chosen, a pre-processing step, consisting in centering and whitening, is first performed. The former assumes subtracting the mean values, while the latter is an orthogonalization transform, $\mathbf{V}$, applied on the set of vectors $\mathbf{x}$ and therefore on the mixing matrix $\mathbf{A}$, increasing the algorithm performance and

reducing the computational load [3]. Then a Non-Circular Complex Fast-ICA algorithm [75] is applied in order to estimate the mixing matrix $\mathbf{W} = \hat{\mathbf{VA}}$. The final step of the algorithm consists in de-whitening the estimated mixing matrix using the inverse of the operation performed during the pre-processing step, assuring that, unlike Eigenvector decomposition, the estimated components are not constrained to any orthogonality among them.

The NC-Complex Fast-ICA algorithm can be applied with different criterions. In all analysis performed throughout this thesis we chose to employ the same approach as in [3], which is specifically suited to scenarios where sources may eventually present non-circular distributions [75]. This fast converging algorithm based on a fixed-point iteration scheme algorithm seeks to emphasise the Non-Gaussianity of the sources by maximising an arbitrary nonlinear contrast function whose extrema coincides with the independent component [5]

$$J_G(\mathbf{w}) = E\{G(|\mathbf{w}^H\mathbf{t}|^2)\} \tag{4.12}$$

where $\mathbf{t} = \mathbf{Vx}$ and $\mathbf{w}$ is the estimated mixing vector (column of the estimated mixing matrix $\mathbf{W}$) which converges to one of the columns of the whitened mixing matrix $\mathbf{VA}$. For the sake of completeness, the fixed-point solution proposed in [75] is given as follow

$$\mathbf{w}_{n+1} = -E\{g(|\mathbf{y}|^2)\mathbf{y}^*\mathbf{t}\} + E\{g'(|\mathbf{y}|^2)|\mathbf{y}|^2 + g(|\mathbf{y}|^2)\}\mathbf{w}_n + E\{\mathbf{t}\mathbf{t}^T\}E\{g'(|\mathbf{y}|^2)\mathbf{y}^{*2}\}\mathbf{t}_n^* \tag{4.13}$$

where the notation $g(z) = dG(z)/dz$ and $g'(z) = dg(z)/dz$ adopted here is the same as the authors employed in [75] and $\mathbf{y} = \mathbf{w}^H\mathbf{t}$. Note that the referred algorithm does not rely on the estimation of the covariance matrix of the sampled vectors.

In [3], a detailed analysis on the performance of the algorithm with respect to the nonlinear function, $G(y)$, was performed. The authors evaluated the kurtosis $G(y) = \frac{1}{2}y^2$, the square root function $G(y) = \sqrt{0.05 + y}$ and the logarithm function, described as the most appropriate in [3], given by

$$G(y) = \log(0.05 + y) \tag{4.14}$$

It is worth pointing out that the choice of the contrast function is application dependent and that the slow growing nature of (4.14) allows a more robust estimation with respect to the presence of outliers when compared to the more intuitive kurtosis measure of non-Gaussianity. A more complex discussion over the Non-Circular Complex Fast-ICA algorithm is out of the scope of the present work. For this purpose the reader is advised to read [3, 47, 75].

The contribution of each source i to the total backscattering, evaluated as the squared l^2 complex norm of the corresponding mixing matrix column is given by

$$||\hat{\mathbf{A}}_i||_2^2 = |\hat{A}_{1i}|^2 + |\hat{A}_{2i}|^2 + |\hat{A}_{3i}|^2 \tag{4.15}$$

Entropy is then calculated in a similar manner as in Eigenvector based decomposition (see (4.7)). Likewise, the parameters for each target vector i are derived in an unchanged manner using either Touzi's TSVM or Cloude and Pottier parameters.

It is important to highlight that, unlike the eigenvalue matrix obtained in the Eigenvector decomposition, that contains the information relative to the contribution of each source displayed in a straightforward manner (diagonal components), the referred information can not be derived using a similar approach when the ICA is employed. Furthermore, in [106], one of the first published attempts of introducing the ICA into the POLSAR data analysis, the contributions were estimated based on the information of the derived sources, rather than on the mixing matrix. Nevertheless, this approach is impracticable for the proposed estimation procedure, since the variances of the estimated sources are set to the unit value. Finally, as it will be shown in Chapter 5, the estimation of the mixing matrix is more relevant than the sources themselves, and in PolSAR applications the latter may even present ambiguities.

For comparison purposes, note that in Eigenvector based decomposition model, the complex single-look observation vector can be written from a source mixing perspective as

$$\mathbf{x} = \mathbf{T}^{1/2}\mathbf{s} \tag{4.16}$$

where $\mathbf{s}$ characterises a white speckle, i.e., with identity covariance matrix and $\mathbf{T}$ is the observation vector coherence matrix, given as a function of the diagonal matrix $\Lambda^{1/2}$, that contains the square root of its eigenvalues, and $\mathbf{Z}$, a matrix whose columns are given by each eigenvector of $\mathbf{T}$ (see 4.6), as follows

$$\mathbf{T}^{1/2} = \mathbf{Z}\Lambda^{1/2} \tag{4.17}$$

Even though (4.10) and (4.16) are mathematically identical, with $\mathbf{A} = \mathbf{T}^{1/2}$, the model and, consequently, the estimation method will provide different estimated sources and mixing matrix.

Finally, it is important to highlight that In PolSAR ICTD research area, the stability of the estimated parameters with respect to polarisation basis changes and rotations around the line of site is a key factor to ensure the decomposition technique performance. In [3], the authors proved that ICA preserves the roll invariant property of Touzi's parameters. In the present thesis, however, we neglect the demonstration of the aforementioned properties. For the purpose, the reader is advised to the above mentioned reference work.

Even though the first step towards a new ICTD parametrization technique had been given in [3], some theoretical aspects of ICA based ICTD were not covered, limiting its full usage in PolSAR data analysis. The following chapters focus on exploiting a few of this aspects in order to increase the range of applications where this technique can be employed.

Chapter 5

ICA based ICTD - Theoretical Aspects

Sommaire

In the context of PolSAR Incoherent Target Decomposition, as reported in the previous chapter, many methods have been proposed in the literature to both decompose an image pixel (composed by distributed scatters) into basic target vectors as well as to correctly retrieve quantitative information from them (parametrization). Concerning the latter, Cloude and Pottier's parameters (entropy, alpha and anisotropy) [19] and Touzi's target scattering vector model [98] are the most employed ones, whose usefulness have already been demonstrated by several authors. Regarding the former, the assessment of PolSAR data statistical properties (derived using neighbouring pixels) is a key factor to derive the average or dominant scattering mechanisms within a resolution cell composed by stochastic distributed targets.

The Eigenvector based ICTD manages to decompose an image pixel into the three most dominant scatters from the averaged coherence matrix. Furthermore, it has an intrinsic property that the derived scatters are orthogonal and uncorrelated, which for Gaussian clutters also means independence. The drawback of this kind of method emerge when the clutter is not Gaussian or not composed by orthogonal mechanisms, situations where the performance of the algorithm could be compromised.

A detailed discussion on Chapter 3 concluded that high heterogeneity scenes (inherent to high resolution systems) may eventually lead to non-Gaussian clutter modelling. SIRVs (Spherically Invariant Random Vectors), have then been constantly employed for modelling high-resolution POLSAR data. Nevertheless, as indicated by several authors [35, 97] and as a conclusion of the results achieved by the employment of the proposed procedure to test the goodness of fit of the product model to PolSAR data (see Chapter 3), polarization independent texture may not be the most suitable model for every kind of clutter. The later highlights

for the need of either considering polarization dependent texture models or the development of model independent algorithms.

In Chapter 4, the Independent Component Analysis, being a model independent algorithm, was described as a potential alternative for highly heterogeneous PolSAR data. The referred method is briefly summarised in three main steps: data selection, based on the statistical classification of the POLSAR image; estimation of independent components and parametrization of the derived target vectors. As stated in [3], the major drawback of the proposed method is the size of the observation dataset, which has to be somewhat larger than the size of the sliding window used in the well established methods. This constraint led the authors in [3] to use an unsupervised classification algorithm rather than relying on a very large sliding window, jeopardising the effectiveness of the method.

The use of a classification algorithm limits the performance of the method in the sense that the image is segmented in a priori defined number of classes with variable sizes, what can compromise the estimation of the target vectors parameters and, as a consequence, the correct interpretation of the scatters present in the area under study. The employment of a classification algorithm introduces a few implications. For example, a class can contain more samples than it needs for a correct estimation of target's parameters, meaning that spatial resolution, highly degraded with the use of this approach, is worse than it could be. On the other hand, if a class do not contain samples enough, the parameters estimated may present a high variance, indicating that the values derived do not always comply with ground truth.

Within this context, in the present chapter a Monte Carlo simulation approach is employed to evaluate the optimal size of a sliding window for various medias, simple ones composed by basic scatters such as helix, dipole, dihedral and trihedral and more complex ones like Surface, Double Bounce and Volume returns. The simulation procedure is similar to the one presented in [58] to evaluate the bias of multilook effect on Cloude and Pottier [18] parameters in Eigenvector based polarimetric SAR decomposition. An unsupervised classification algorithm is employed to identify within a RAMSES X-band image acquired over Brétigny, France (see Appendix E), sets of samples characterising Surface, Double Bounce and Volume type of average scattering mechanisms. The mixing matrix and the covariance matrix for each of the aforementioned complex type of scatters are estimated using proper algorithms (Non-Circular Complex Fast-ICA algorithm [47] and Fixed-point algorithm [104], respectively) and used to bootstrap random samples for the Monte Carlo simulation approach. It is important to highlight that, as reported in [3], the mixing matrix and the covariance matrix are potentially different, thus the set of random samples used in the ICA and Eigenvector decomposition analysis are not the same. Regarding the analysis with basic scatters, the aforementioned parameters are manually set.

The main difference concerning the generation of the simulated data is that in [58] only Gaussian variables were addressed and no texture was considered, meaning that the sampled coherence matrix has the complex Wishart distribution (see (3.2)). In the present work the heterogeneous clutter is described by a variation of the Spherically Invariant Random Vectors (SIRV) model [104], assuming a polarization dependent texture, characterised by a random vector. Analogously to what was done to the mixing and covariance matrices, the

texture distribution parameters, for each of the aforementioned complex type of scatters, are estimated from the real dataset while for basic scatters, they are manually set.

Finally, in this chapter we also address another drawback inherent to ICA described in the literature, that could limit its usage in PolSAR application: the central principle of non-gaussianity of the sources that has to be assumed in the model [48]. As mentioned in Chapter 3, in remote sensing SAR community, generally, the clutter is assumed homogeneous and under the basis of the central limit theorem, it is described by a zero-mean, multidimensional, complex Gaussian pdf [65, 96, 60] (see (3.1)). Even though heterogeneous clutter models have gained notoriety, one single Gaussian source could jeopardise the performance of ICA, making its use inappropriate. Nevertheless recent studies [37] proved that even Gaussian sources can be separable under certain conditions and we depart from these results to increase, in PolSAR data analysis, the range of potential applications to this technique.

5.1 Identifiability, separability and uniqueness

In [3], the authors proved that the ICA preserves the roll invariant property of Touzi's parameters. Continuing with the establishment of theoretical background for the proper use of ICA in polarimetric decomposition, in the present work the identifiability, separability and uniqueness of ICA, when employed in PolSAR applications, are addressed. We revisit the theorems derived in [37] and establish general conditions for an efficient blind source separation approach by means of ICA to polarimetric target decomposition.

Each of the above mentioned properties is relevant for a specific type of application. The separability is investigated when the ICA is employed for retrieving the original sources, the identifiability when the mixing matrix is the one that should be correctly derived and finally, uniqueness is addressed when there is an interest on the distribution of the sources [37]. Problems where sources may have normal components with the same circularity coefficient, for instance, can be identifiable but not separable or unique.

In the framework of PolSAR applications, the interest lies in the estimation of the mixing matrix rather than in the sources themselves. Therefore the identifiability property plays a key role in ICA polarimetric target decomposition. The authors in [37] state that the absence of complex normal sources is not the only sufficient condition to correctly reconstruct the mixing matrix A. They claim that when A is of full column rank and there are no two complex normal sources with the same circularity coefficient, it is also possible to retrieve A. The latter also guarantees that the model is separable.

The previous statement ensures that if there are more sources than mixtures in the model then, in order to correctly retrieve the mixing matrix, the clutter can not have any Gaussian component. Nevertheless, if this is not the case, the clutter can even be entirely composed by Gaussian components. This surprising and yet untapped property of ICA can be of great interest to PolSAR community, since it determines that Gaussian sources and the mixing matrix of models containing Gaussian sources can indeed be retrieved under certain conditions.

5.2 Monte Carlo simulation approach

The authors in [3] proved the usefulness of the Independent Component Analysis in ICTD by means of its employment in real data, leaving some open questions like the performance of the algorithm under a sliding window implementation and under clutter containing Gaussian components scenarios. In the present work a Monte Carlo simulation approach is performed in order to complement the results obtained in [3] and empirically establish theoretical background that will allow a more efficient use of ICA in further PolSAR applications.

5.2.1 Sliding window optimal size estimation

The heterogeneous clutter is here described by a variation of the Spherically Invariant Random Vectors (SIRV) model, with normalised covariance matrix and polarization dependent texture, defined in Chapter 3. Different assumptions regarding its composition are assumed: basic scatters (orthogonal and non-orthogonal) representing average or dominant scattering mechanisms within the imaging cell and complex scatters (Surface, Double Bounce and Volume). The Independent Component Analysis does not include the estimation of the covariance matrix itself, nevertheless, since, for comparison reasons, we perform the same simulations with the Eigenvector based decomposition, the coherence matrix estimator defined in (3.6) is also addressed.

Each simulation procedure, for a given window size and clutter type is repeated 1000 times and then the estimated parameters are averaged. For the first set of simulations the average or dominant scattering mechanisms within the imaging cell are assumed basic scatters and two scenarios are established: one containing orthogonal targets and the other containing non-orthogonal mechanisms. The Gamma distribution shape and scale parameters that characterises the texture are fixed and set to 1.95 and 0.51, respectively. They are used to generate a simulated texture vector $\tilde{\boldsymbol{\tau}}^c$. Afterwards, a complex normal distributed random vector $\tilde{\mathbf{z}}$, i.e., $\tilde{\mathbf{z}} \sim CN(\mathbf{0}, \mathbf{I})$ is generated. Finally, the simulated observation vector for each class is then given, analogous to (E.24), by

$$\tilde{\mathbf{x}}^c = \mathbf{A}\sqrt{\tilde{\boldsymbol{\tau}}^c} \cdot \tilde{\mathbf{z}} \tag{5.1}$$

The simulated dataset (5.1) is then used as input for both the Eigenvector decomposition and ICA decomposition.

Let us first investigate the behaviour of Eigenvector decomposition, hereafter also referred to as PCA (*Principal Component Analysis*) for simplicity and ICA under the assumption that the heterogeneous clutter is composed by orthogonal targets. It is important to highlight that special care has to be taken in the appropriate choice of the simulated scattering mechanisms, since Touzi TSVM present ambiguities for some specific scatters, as addressed in Appendix D. In the present analysis, the clutter composition is 60% of helix left screw, 30% of helix right screw and 10% of trihedral. The mixing matrix, in Pauli basis for such type of clutter

[98] is given by

$$\mathbf{A} = \begin{bmatrix} 0.3162 & 0 & 0 \\ 0 & 0.3873 & 0.5477 \\ 0 & 0.3873j & -0.5477j \end{bmatrix} \tag{5.2}$$

where $j = \sqrt{-1}$ is the imaginary unit and $\mathbf{A} = \mathbf{T}^{1/2}$ according to (4.10) and (4.16). The Entropy of such clutter is 0.8 while Touzi's roll invariant parameters are displayed in Table 5.1.

Table 5.1: Orthogonal mechanisms Touzi's parameters

	τ_m [°]	α_s [°]	ϕ_{α_s} [°]
Helix left screw	45	45	0
Helix right screw	−45	45	0
Trihedral	0	0	0

Figure 5.1 presents the estimated Touzi's roll invariant parameters and entropy derived using ICA and Eigenvector decomposition. Note that both Eigenvector decomposition, as anticipated by [58], and ICA correctly derive the Touzi's parameters corresponding to the three components as well as the entropy. The third component is more problematic for both decomposition, presenting a lower convergence rate. Regarding the Entropy and first and second components, the behaviour of Eigenvector decomposition and ICA are very similar, and the same window size can be used for both.

The choice of the sliding window size is a constant concern in SAR community since high values decrease considerably the system spacial resolution and low values may eventually introduce bias in the estimation of a few parameters. Many authors raised the question of what would be the optimal window size for several different applications, e.g. [58, 65]. Note in Figure 5.1 that a window size 11×11 provides a good estimation of the first and second components TSVM parameters as well as the entropy with negligible bias, representing a good choice in terms of performance tradeoffs.

Next a scenario with non-orthogonal targets is addressed. The clutter is then composed by 60% of helix left screw, 30% of dipole and 10% of dihedral. The mixing matrix, in Pauli basis, for such type of clutter is given by

$$\mathbf{A} = \begin{bmatrix} 0 & 0.3873 & 0 \\ 0.3162 & 0.3873 & 0.5477 \\ 0 & 0 & -0.5477j \end{bmatrix} \tag{5.3}$$

The Entropy of such clutter is also 0.8 while Touzi's roll invariant parameters are displayed in Table 5.2.

As expected, since Eigenvector decomposition has an intrinsic constraint that the estimated components are mutually orthogonal, it is unable to correctly derive the original

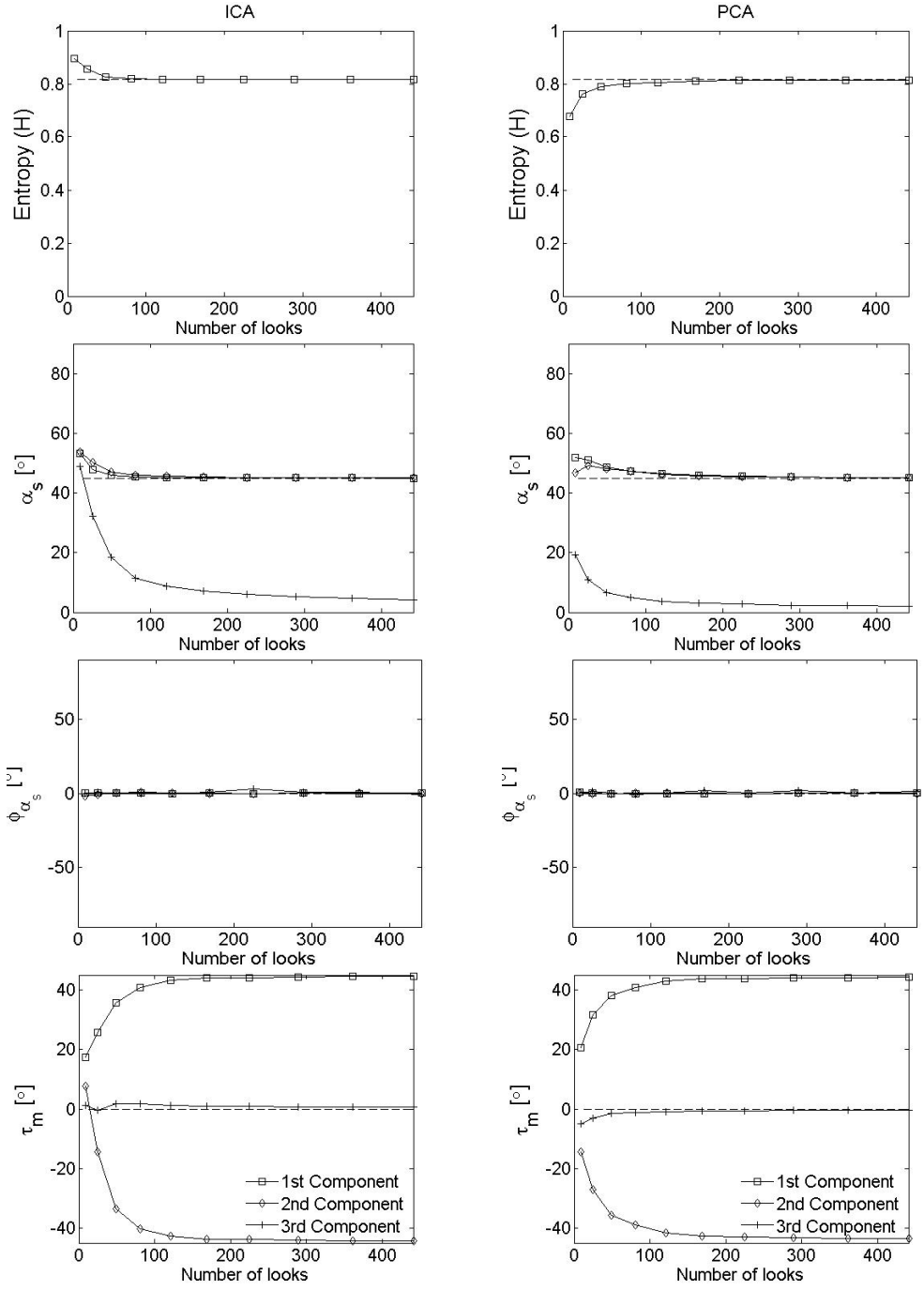

Figure 5.1: Entropy and Touzi TSVM parameters derived with ICA and Eigenvector polarimetric target decomposition, PCA, for a clutter composed by basic orthogonal mechanisms.

mixing matrix, failing to estimate the contents of the heterogeneous clutter. On the other hand, ICA is not constrained to orthogonality therefore it successfully estimates the three components parameters. Figure 5.2 presents the results of ICA.

Table 5.2: Non-orthogonal mechanisms Touzi's parameters

	τ_m [°]	α_s [°]	ϕ_{α_s} [°]
Helix left screw	45	45	0
Dipole	0	45	0
Dihedral	0	90	0

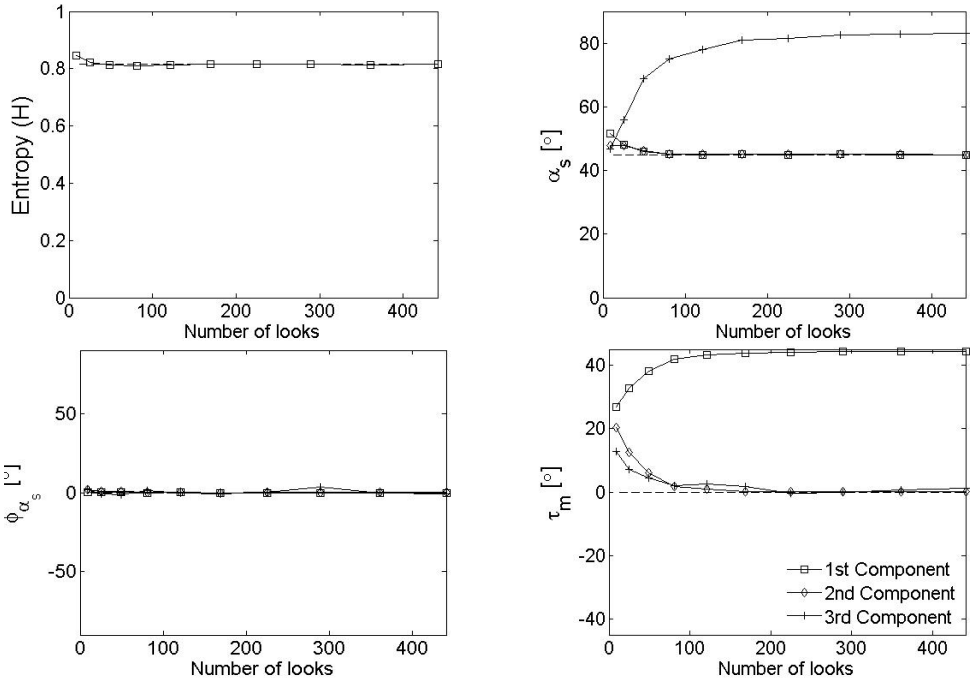

Figure 5.2: Entropy and Touzi TSVM parameters derived with ICA polarimetric target decomposition for a clutter composed by basic non-orthogonal mechanisms.

Note that the convergence rate of the estimated parameters, compared to a scenario with only orthogonal targets (see Figure 5.1) nearly doesn't change, concluding that the same window size can be used despite of the orthogonality of the scattering mechanisms.

For the sake of completeness, Figure 5.3 presents the estimator standard deviation in order to better evaluate its performance. Note that, the standard deviation of most of the parameters tends to zero, with the exception of the third component ϕ_{α_s} and τ_m.

Let us now address more complex type of targets, composed by either Surface, Double-Bounce or Volume scatters. The first step in the simulation procedure is to define the observation dataset from which the covariance matrix, the mixing matrix and the texture parameters will be estimated for each of the aforementioned mechanisms. An unsupervised classification algorithm developed for highly textured POLSAR data [42] is employed to identify within a RAMSES X-band image acquired over Brétigny, France (see Appendix E), sets of samples characterising Surface, Double Bounce and Volume type of average scattering mechanisms.

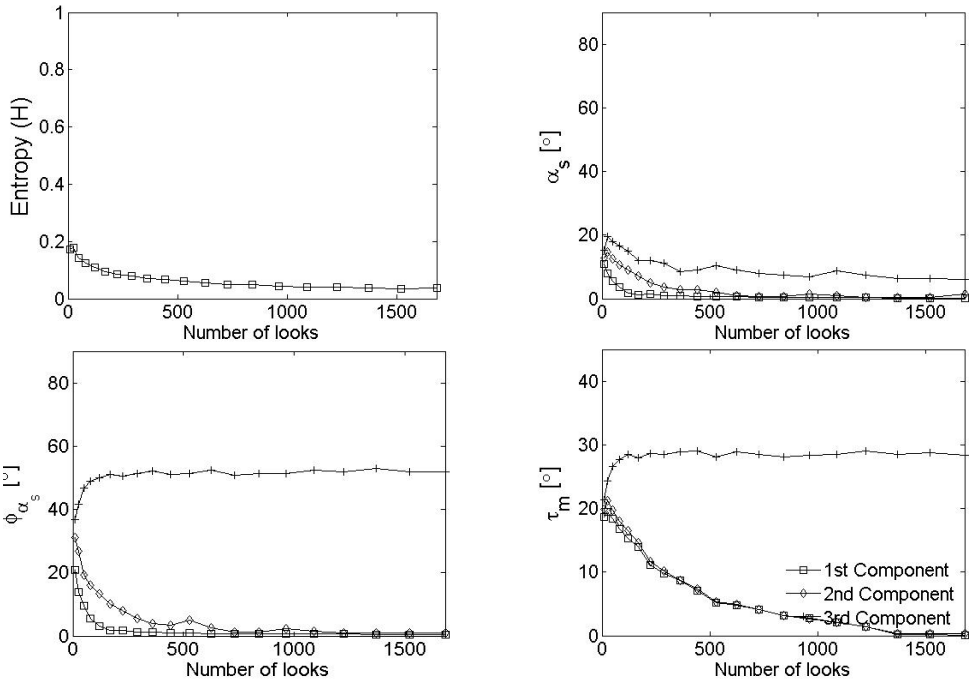

Figure 5.3: Standard deviation of the Entropy and Touzi TSVM parameters derived with ICA polarimetric target decomposition for a clutter composed by basic non-orthogonal mechanisms.

More details on the classification algorithm is provided in the next chapter, where it assumes a more crucial role on the analysis. Even though it has already been shown throughout this thesis, for the sake of completeness, Figure 5.4 presents the referred area in Red (HH+VV), Green (HV) and Blue (HH-VV), the classification algorithm output and an H/α feature space.

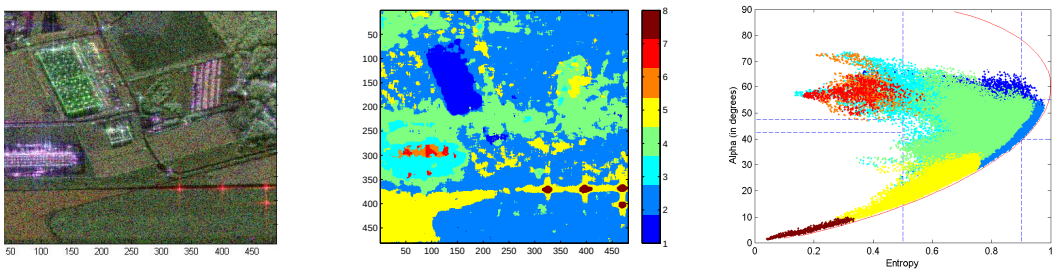

(a) (b) (c)

Figure 5.4: Brétigny area under study: (a) RGB image, Red (HH+VV), Green (HV), Blue (HH-VV); (b) Statistical classification algorithm output; (c) H/α feature space.

Analysing the H/α feature space, it is possible to concluded that Class 1 is mainly composed by Volume scatters, Class 5 is mainly composed by Surface and Class 6 is mainly composed by Double-Bounce scatters. Therefore samples, corresponding to each class were extracted from the referred set and the mixing matrix, $\hat{\mathbf{A}}^c$, and covariance matrix, $[\hat{M}]^c_{FP}$,

were estimated for each of the described classes ($c = 1, 2, 3$) of mechanisms. An algorithm described in [24], initialised with the identity matrix, is used for the latter. Next, the texture is also estimated for each observation vector corresponding to one of the three aforementioned classes (Surface, Double Bounce and Volume).

The generalised texture maximum likelihood estimator for each observation vector is given by 3.7. By estimating the texture parameter for each pixel, we get a set of realizations from which it is possible to retrieve its distribution parameters. Since the probability density function of the texture random vector is not explicitly specified by the model, as well as in the previous set of simulations, we will analyse the parameters convergence rate assuming it to have a Gamma distribution. The parameters of the distribution are then extracted from the already estimated $\hat{\tau}_i^c$ and used to generate simulated texture vectors to bootstrap random samples for the Monte Carlo simulation approach. The remaining steps of the simulated data generation are the same as previously described. It is important to highlight that, as reported in [3], the mixing matrix and the covariance matrix are potentially different, thus the set of random samples used in the ICA and Eigenvector decomposition analysis are not the same.

Figure 5.5 presents the results of the polarimetric decomposition using both ICA and Eigenvector decomposition (PCA). Note that, despite the low convergence rate of ϕ_{α_s} for Surface type of scatter, the convergence rate behaviour achieved by both ICA and PCA are nearly the same as the ones obtained in the simulations with basic scatters as the average or dominant scattering mechanisms. This conclusion leads to the possibility of using the same window size as previously reported of 11×11 samples.

5.2.2 Gaussian sources

As addressed in Section 5.1, the mixing matrix and, consequently, Touzi's parameters can be correctly estimate even if the clutter has Gaussian components. Figure 5.6 shows the results of the estimation of the entropy and Touzi's parameters, α_s, τ_m, ϕ_{α_s} for a model described by (4.10) with a mixing matrix A given as (5.3) and the heterogeneous clutter s composed by two sources described by the SIRV model and one Gaussian with zero mean and unit variance. The Gamma distribution shape and scale parameters that characterises the texture in the SIRV sources are fixed and set to 1.95 and 0.51, respectively.

Note that ICA is able to correctly estimate Touzi's parameters at the expense of a noticeable lower convergence rate for the helicity τ_m, and a slightly lower convergence rate of α_s, increasing the Bias for lower window sizes. Nevertheless, it fails to derive the correct entropy value, overestimating it.

5.2.3 Spatial correlation

Spatial correlation is a phenomenon inherent to remote sensing SAR systems. This feature has already been explored by many different authors specially in the conception of classification

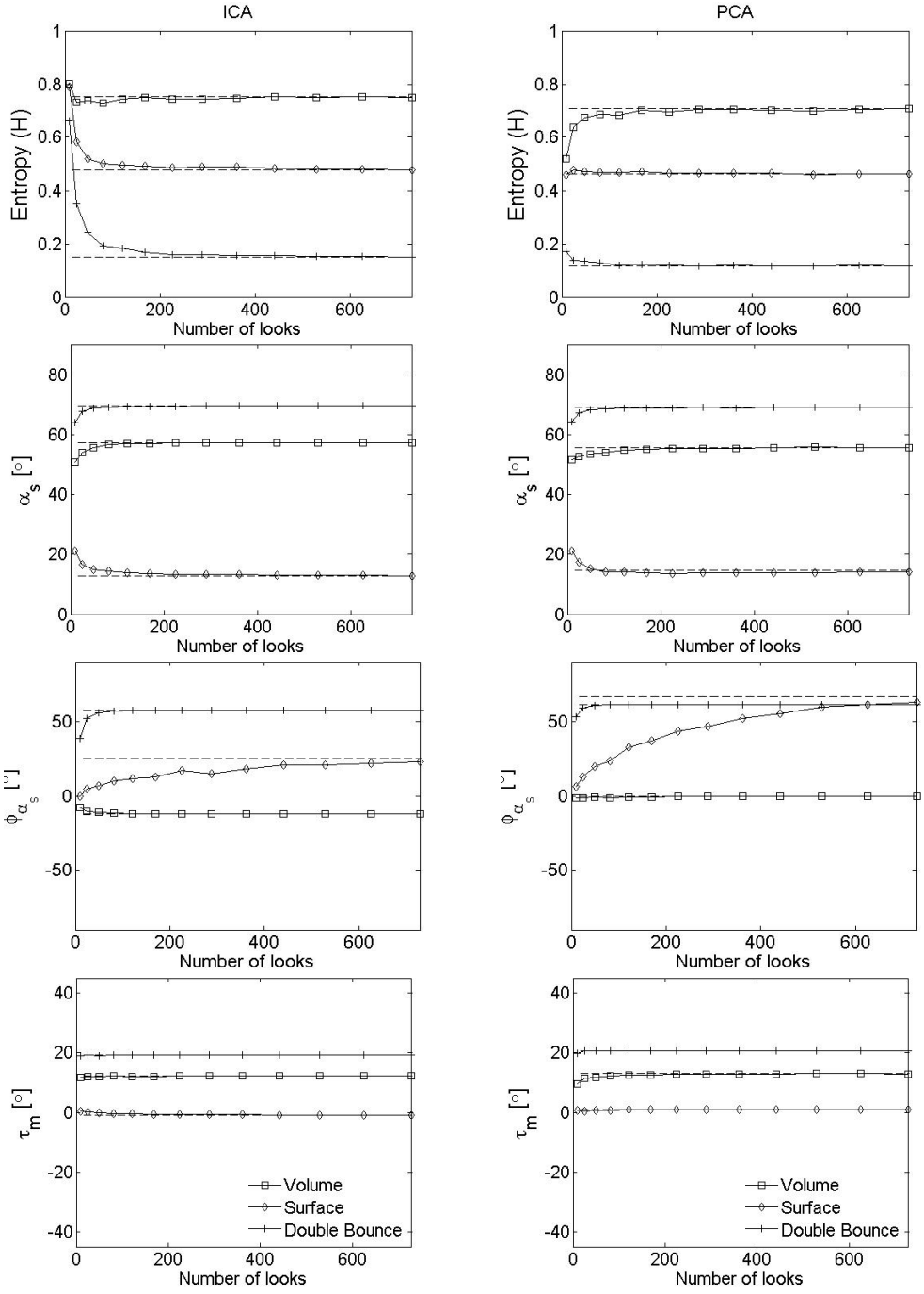

Figure 5.5: Entropy and Touzi TSVM parameters derived with ICA and Eigenvector polarimetric target decomposition, PCA, for a complex clutter types: Surface, Double-Bounce and Volume.

algorithms [103]. In the present work spatial correlation is introduced for each source, by creating a statistical dependence on neighbours pixels and thus generating a more realistic type of clutter. The robustness of ICA is verified under this scenario for a clutter type

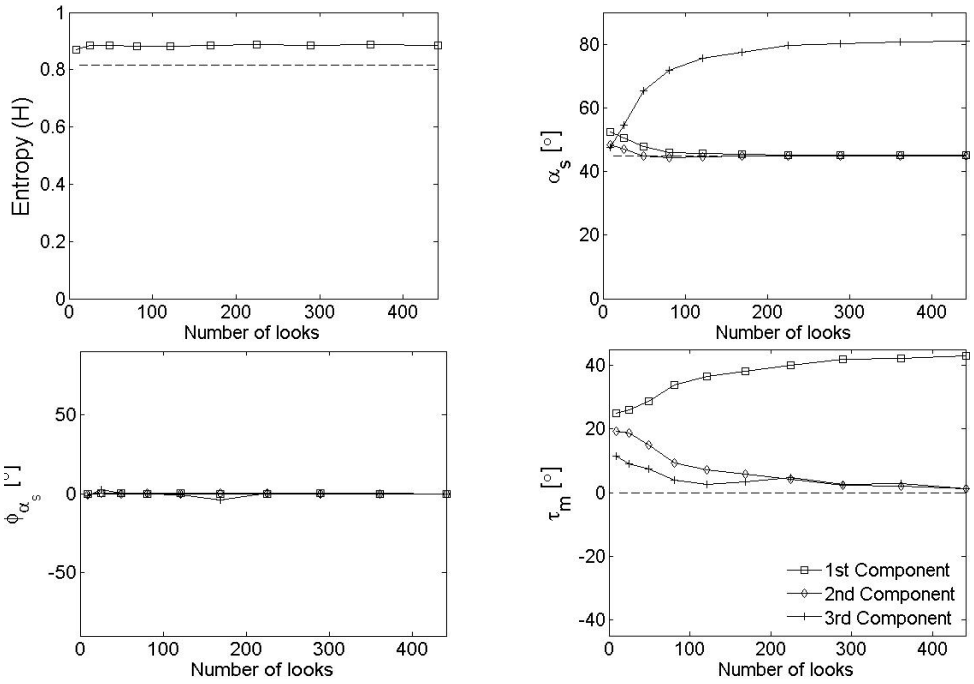

Figure 5.6: Entropy and Touzi TSVM parameters derived with ICA polarimetric target decomposition for a clutter composed by basic non-orthogonal mechanisms and one Gaussian source.

composed by basic non-orthogonal mechanisms, as previously described in Section 5.2.1 and Gamma textured sources.

The procedure of generating correlated Gaussian samples and, therefore, statistically dependent pixels is achieved by and additional step of filtering. In theory, the random process that characterises the speckle with no statistical dependence in the space dimension has a flat infinite power spectral density. Therefore, its Autocorrelation function has a strong peak (represented by a Dirac delta function) at the origin and thus all samples are uncorrelated, what for Gaussian sources, also means independence. The generation of such kind of stochastic process is unfeasible, due to the inability of generating a flat infinite power spectral density. Therefore, the generation of uncorrelated Gaussian random variables is achieved by a computational procedure that creates samples from a stochastic process with a flat power spectral density and bandwidth $B = f_s$, where f_s is the sampling frequency. The Autocorrelation function of such process is a sync(t), with nulls spaced by $t_z = \frac{1}{B}$, thus the extracted samples are uncorrelated, what for Gaussian sources also means independence. If the bandwidth of the referred stochastic process is reduced (rectangular filtering), the samples do not correspond to the nulls anymore and therefore are correlated, and hence statistically dependent.

Figure 5.7 presents the estimated entropy and Touzi TSVM parameters for the aforementioned configuration. Note that spatial correlation does not significantly deteriorates the performance of ICA polarimetric decomposition, slightly increasing the Bias for low window

sizes.

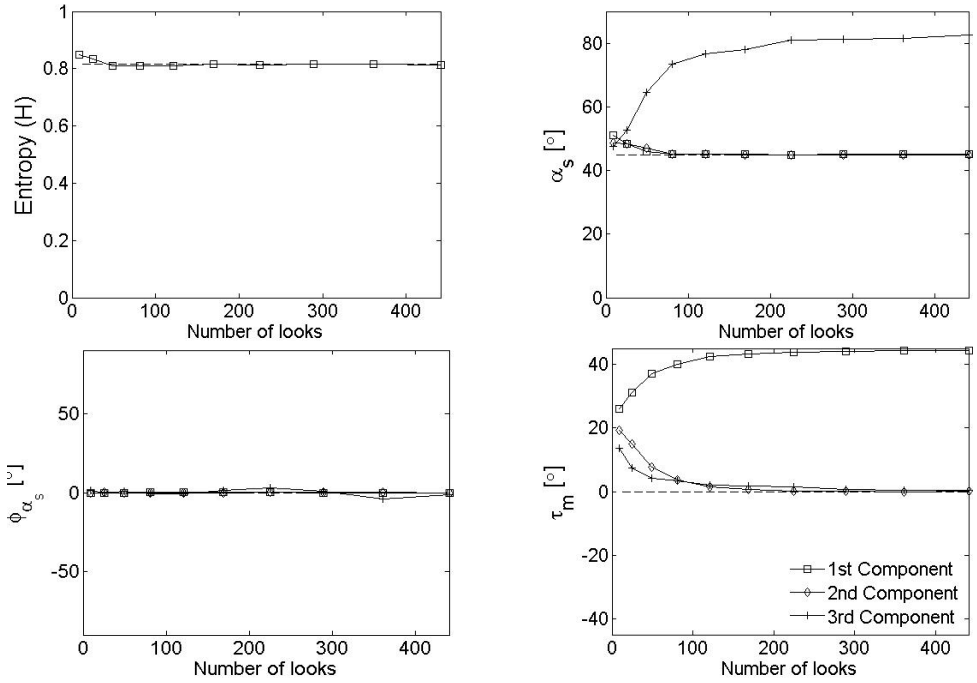

Figure 5.7: Entropy and Touzi TSVM parameters derived with ICA polarimetric target decomposition for a clutter composed by basic non-orthogonal mechanisms and with spatial correlation.

5.3 Remarks

The present chapter focused on addressing and quantifying the two main drawbacks of the employment of Independent Component Analysis in polarimetric target decomposition: the higher amount of samples needed and the assumption of non-Gaussian clutter. Based on simulated data we managed to better investigate the theoretical concepts and quantify the bias on the entropy and Touzi's parameters caused by insufficient number of samples used in their estimation.

It is shown that when the averaged or most dominant scattering mechanisms that characterises the heterogeneous clutter are orthogonal, Touzi's parameters estimated using ICA are the same as the ones estimated using Eigenvector decomposition and the convergence rate of the estimation is nearly the same. When the clutter is composed by non-orthogonal mechanisms, unlike Eigenvector decomposition, ICA successfully derive the basic scattering mechanisms without compromising its performance.

Simulations with complex type of scatters, Volume, Double-Bounce and Surface, whose characteristic were extracted from real data, heterogeneous clutter with Gaussian sources

and with spatial correlation showed similar results, giving strength to the proposal of using a sliding window size of 11×11 in ICA based ICTD approach.

Finally, it is important to highlight once again that the Independent Component Analysis is a model independent strategy to analyse the behaviour of non-Gaussian heterogeneous clutters (inherent to high resolution SAR systems). It proved itself very useful by introducing an alternative way of physically interpreting a polarimetric SAR image which, unlike Eigenvector decomposition (PCA), estimates average mechanisms not constrained to any orthogonality among them.

Chapter 6

ICA based ICTD - Practical Aspects

Sommaire

In Chapter 5, the theoretical gap involving ICA based ICTD was reduced, enabling a considerable increase in its usage. Nevertheless, since it is a recently introduced ICTD approach to PolSAR image analysis, it is still difficult to assert if there are specific scenarios where ICA performance is higher than PCA's (Eigenvector based ICTD). Alternatively, we believe that the additional information introduced by ICA can be combined with the information provided by the Eigenvector decomposition in order to better propose, among others, classification and geophysical parameter inversion algorithms. Within this context, the present chapter addresses, in more details, the results obtained when ICA based ICTD is performed on varied datasets, comparing them to the information provided by the Eigenvector approach. For more details on the datasets, the reader is advised to go to the Appendix E.

6.1 Cloude and Pottier H/α feature space analysis

The analysis of Cloude and Pottier H/α feature space outcome when ICA based ICTD is performed first considers a RAMSES X-band image acquired over Brétigny, France. The increase of possibles H/α pairs brought about the ICA based ICTD can be explored from several aspects. In the present work, we focus our investigation in pixels that fall in region 3 in the H/α plane. For that purpose, first we address the outputs of an unsupervised classification algorithm developed for highly textured POLSAR data [42] to identify pixels that switch between classes originally assigned to regions 6 and 2 when the Eigenvector approach is applied.

The aforementioned method relies on a statistical test on the covariance matrices estimated for each pixel considering its neighbours within a sliding window. A distance measure,

derived based on the data probabilistic model adopted, is used to verify to which class a given pixel corresponds. The distance measure employed in the present work assumes that the heterogeneous clutter is described by the Spherically Invariant Random Vectors (SIRV) model, with normalised covariance matrix. As described in Chapter 3, the SIRV is, originally, a class of non-homogeneous Gaussian processes with random variance [104] where each observation vector is defined as the product between an independent complex circular Gaussian vector, characterising the speckle and a positive random vector characterising the spatial variations in the radar backscattering (texture). The probability density function of the texture random vector is not explicitly specified by the model.

The first step prior to the employment of the classification algorithm is to assess the conformity of the data with respect to the statistical model considered. In Chapter 3 a general framework which allows quantitative evaluation of the SIRV stochastic models goodness of fit with respect to a given multidimensional SAR dataset was proposed. The referred Wald test consists in verifying if the structure of its fourth order moment (quadricovariance matrix) matches the one of Complex Elliptical Symmetric Distributions (CES), a more general class of which SIRVs are part. This procedure was already performed in Chapter 3 and its output is presented in Figure 3.9.

As concluded in Chapter 3, only a small portion of the pixels in the area under study fails the test (18%), indicating that the SIRV model is a good representative of the data stochastic behaviour. The classification algorithm is then briefly described in 4 steps: generation of the initial population based on the H/α classification (see Chapter 4), where pixels corresponding to the same region compose a single cluster; compute each cluster centre; calculate the distance measure between each pixel to all cluster centres; associate the pixel to the cluster corresponding to the smallest distance derived in the previous step.

The adaptive nature of the classification algorithm seeks to group pixels with similar statistical behaviour, in an attempt to better cluster similar physical phenomena. The high amount of pixels that switch between classes evidence that H/α classification fails to fully explain certain type of scattering mechanisms. Figure 6.1 presents the initial H/α classification output, the statistical classification algorithm output after 4 iterations and the corresponding H/α feature spaces.

It is relevant to report that in previous works that employed ICA based ICTD, the decomposition was performed considering a global approach, instead of a sliding window [3, 80]. Pixels from each class were considered as belonging to the same observation vector and the parameters were derived for the entire class. It is shown later on this chapter that the estimated centre of mass on the H/α plane, assuming the aforementioned consideration are nearly the same for ICA and Eigenvector based ICTD [80]. This result indicates that in a global point of view, the average ICA based ICTD performance resembles the one achieved with the Eigenvector approach.

Let us now investigate the evidences that the limitations inherent to the Eigenvector approach in the H/α feature space can be compromising the correct interpretation of the SAR image. In the present work, our focus relies on the analysis of pixels whose polarimetric

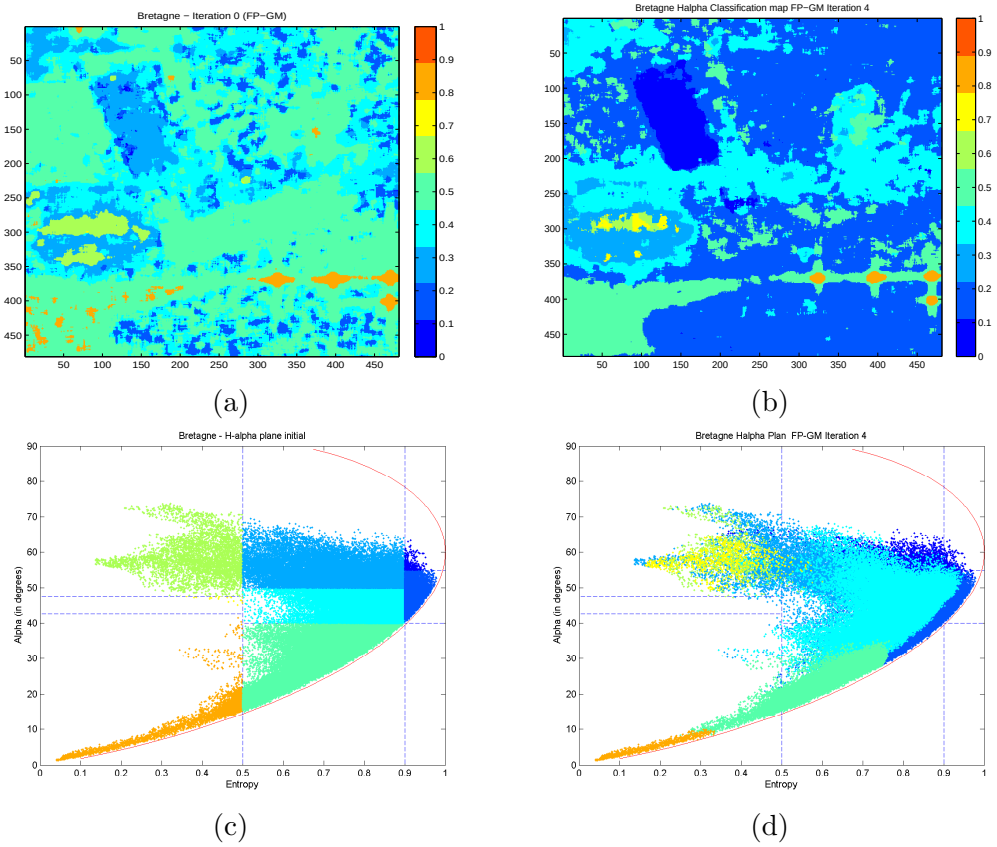

Figure 6.1: Brétigny area under study: (a) H/α classification output; (b) Statistical classification algorithm output, 4th iteration; (c) H/α initial feature space; (d) H/α feature space after the 4th iteration.

behaviour falls into regions 2,3 and 6. According to the authors in [19], region 6 represents a medium entropy surface scatter. When compared to the expected behaviour of surface mechanisms, it is stated that the increase in entropy can be related to either an increase in the surface roughness or due to canopy propagation effects. If the entropy increased further and the α range was kept unchanged, pixels would fall in region 3 and would be classified as a high entropy surface. Nevertheless, due to the mathematical constraint discussed in Chapter 4, no scattering mechanisms can be identified as belonging to this region. Finally, region 2, stands for high entropy vegetation scattering, including volume type of scatters. The natural behaviour of forest canopies and some types of vegetated surfaces with random highly anisotropic scattering elements may fall in this region [19]. Note that the physical phenomenologies represented by region 6 and region 2 are very different. Therefore, it should be expected very few doubt in determining if a pixel is better represented by region 6 or by region 2.

Figure 6.2 indicates the amount of pixels that move from class 6 to class 2 at each iteration. The total amount represents 62.36% of the set originally classified in region 6. If we associate a single pixel in the edge between regions 6 and 2 ($H = 0.9$ and $\alpha = 39°$) as an extra class

of the initial population defined by the H/α classification, a huge amount of pixels switch to this new class, as seen in Figure 6.3.

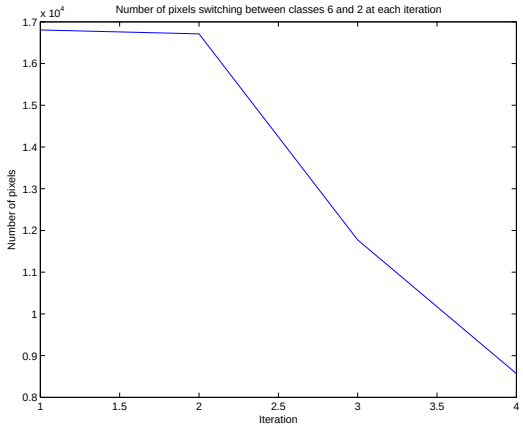

Figure 6.2: Number of pixels switching between classes 6 and 2 after each iteration.

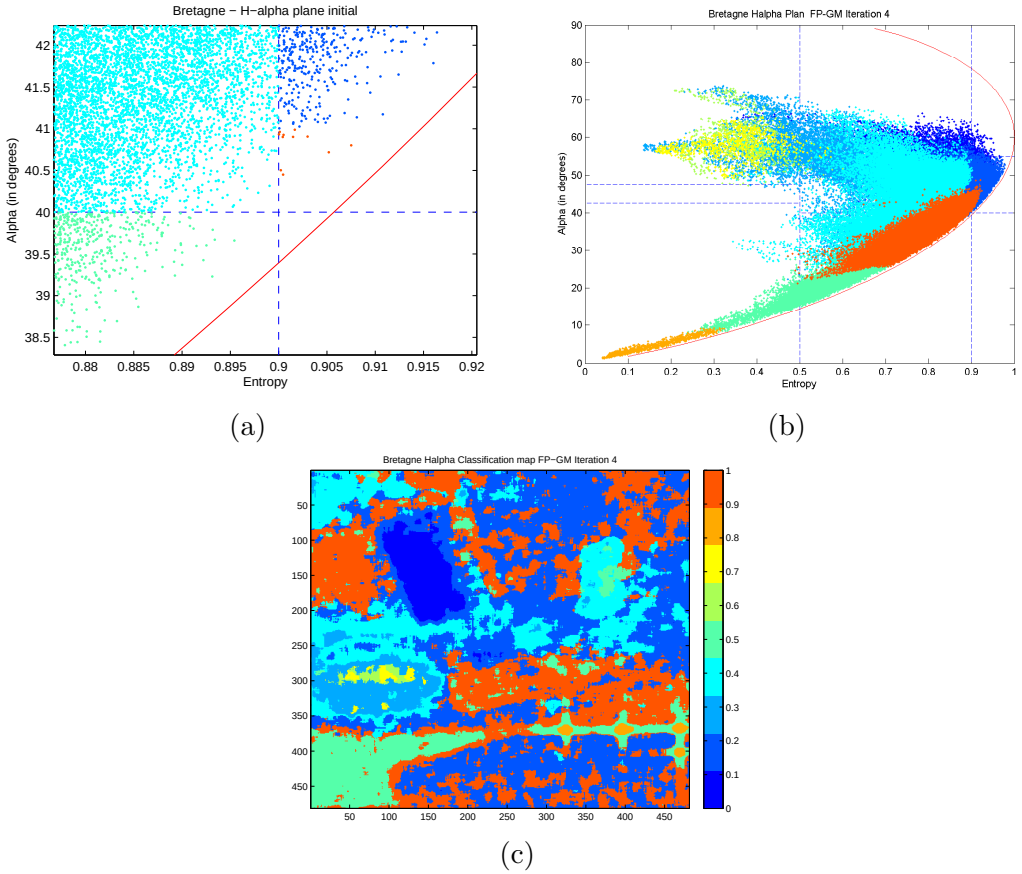

Figure 6.3: Results considering an extra class defined as the edge between regions 6 and 2: (a)H/α classification output, (b) H/α feature space after the 4th iteration and (c) Statistical classification output after the 4th iteration.

Now lets address the new information provided by the ICA based ICTD. A comparison with the H/α classification resultant taking into consideration the ICA based ICTD (depicted in Figure 6.4) indicates that a high percentage of the pixels that switch between classes originally assigned to regions 6 and 2 are classified as belonging to region 3. More precisely, 69.23%. Furthermore, only 10% of the pixels classified in region 3 where not originally classified in region 6 when the Eigenvector approach was employed. These results indicate that the physical behaviour of the switching pixels is better represented by region 3, high entropy surface scattering, which is unfeasible when the Eigenvector approach is employed.

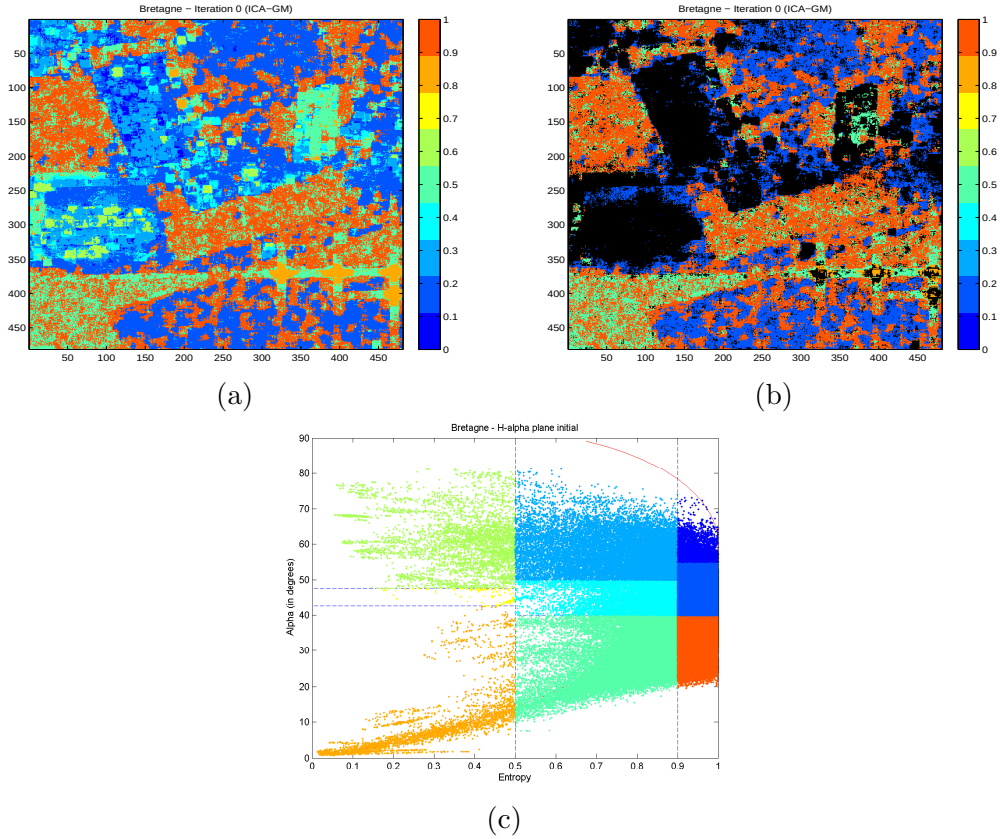

Figure 6.4: (a) H/α classification output, (b) H/α classification output of pixels that fall into Eigenvector approach non feasible regions when ICA based ICTD is employed and (c) H/α feature space.

It is important to highlight that the choice of the sliding window size is a constant concern in SAR community since high values decrease considerably the system spatial resolution and low values may eventually introduce bias in the estimation of a few parameters. In Chapter 5 it was shown that a window size 11×11 represents a good choice in terms of performance tradeoffs relative to ICA based ICTD [81]. This size is in accordance to what is referred to as optimal by other authors when the Eigenvector approach is employed [58, 65].

A good indicator of the robustness of the new information provided by the ICA based ICTD with respect to the H/α feature space is the false alarm rate it provides. A tropi-

cal forest scenario is taken into consideration to verify if pixels are incorrectly classified as belonging to region 3 when their natural phenomenology clearly indicates that they should be represented by region 2. Data from the P-band airborne dataset acquired by the Office National d'Études et de Recherches Aérospatiales (ONERA) over the French Guiana in 2009 in the frame of the European Space Agency campaign TropiSAR is addressed.

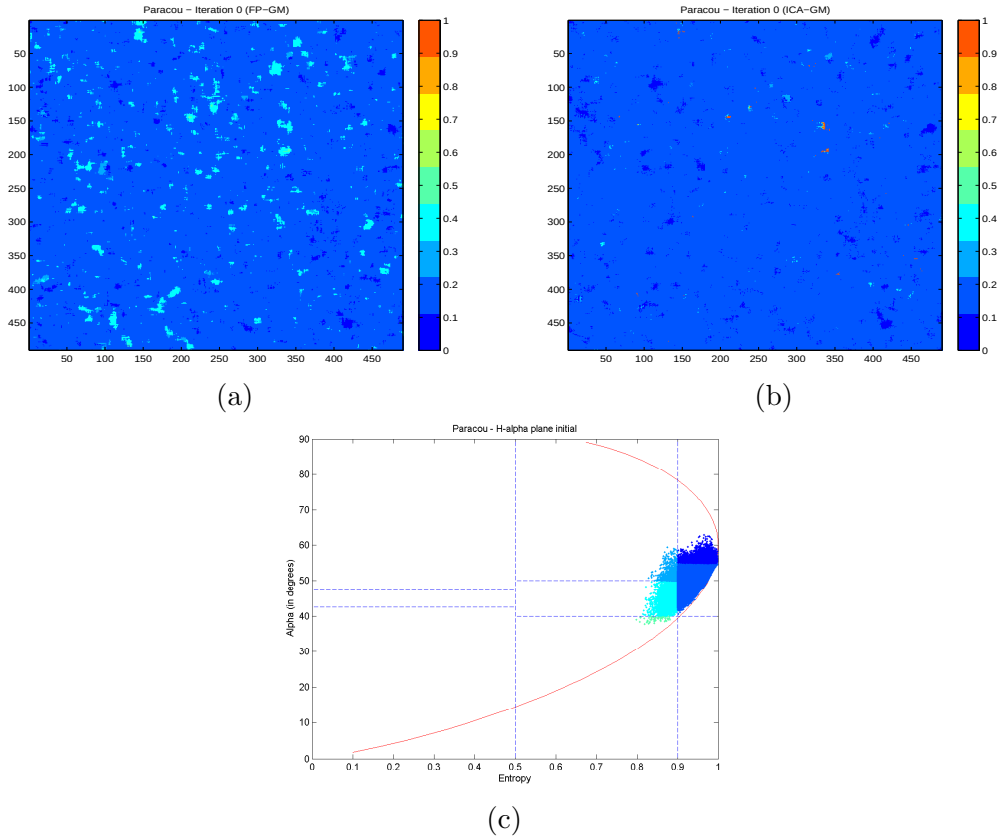

Figure 6.5: French Guiana area under study: (a) H/α classification output when the Eigenvector approach is employed and (b) H/α classification when ICA based ICTD is taken into consideration and (c) H/α feature space when the Eigenvector approach is employed.

Note in Figure 6.5 that ICA correctly associates most of the tropical forest physical behaviour to region 2, volume scatters, as expected, considering the forest canopies effect. Nevertheless the estimated entropies are higher when compared to the Eigenvector approach.

Finally, we conclude the investigation of the new information provided by the ICA related to the H/α feature space by analysing the results of a combined use of the ICA based ICTD and the statistical classification algorithm described. The ICA can be inserted in two stages of the referred algorithm, whose feasibility are discussed as follows.

First, it can be used as the initial population, considering the H/α classification output resultant from the ICA based ICTD. In [42] the authors state that the initial population does not affect the classification output, presenting a comparison of the results achieved when the Eigenvector H/α classification is used for this purpose and when a random population

is employed. Nevertheless, the introduction of a new class of mechanisms, represented by region 3 in the H/α plane can indeed influence the outcome of the classification algorithm. It is important to highlight that no further modifications are necessary in this approach. Since the data is mainly composed by SIRV samples (see Figure 3.9), and we are verifying the statistical resemblance between pixels based on their covariance matrices, the distance measure employed so far can be kept unchanged, as well as the remainder of the code.

Alternatively, a more drastic modification to the algorithm could be proposed. Instead of estimating the covariance matrices centre of mass for each class, the mixing matrices barycenter could be addressed. Additionally, a proper distance measure would also have to be derived accordingly. The implementation of such approach is not straightforward, since the task of estimating matrix geometric means is a complex subject. The concept of geometric mean for more than two matrices has only been fully defined recently, powered by the association of the geometric mean of two positive definite matrices, M_1 and M_2, as the midpoint of the geodesic (with respect to a natural Riemannian metric) joining M_1 and M_2 [4]. While the derived theory is valid when addressing positive definite matrices [4] (which is the case of the covariance matrices), it does not hold for the mixing matrices estimated with ICA, which are not necessarily positive definite. Therefore, more effort has to be spent in order to define a proper concept for the mixing matrices mean. A more complex discussion over this topic is out of the scope of the present work. For that purpose, the reader is advised to go to [4, 50, 70].

The previous discussion make it clear that the second alternative for a combined use of ICA and the classification algorithm requires a more detailed theoretical analysis prior to its implementation. Therefore, in the present work, we address the first approach proposed. Figure 6.6 presents side by side the output of the statistical classification algorithm when the Eigenvector H/α classification is used as the initial population and when the ICA based ICTD H/α classification is employed.

Note that the class associated to region 3 persists throughout the iterations and the corresponding clusters are representing well defined regions. Furthermore, it is important to highlight that the clusters represented by all other classes are nearly the same in the Eigenvector approach and ICA based ICTD.

It is also important to emphasise that, as previously mentioned, the new information provided by the ICA based ICTD with respect to Cloude and Pottier H/α feature space can be addressed from many aspects. In the present work we focused on scattering mechanisms that were originally classified as medium entropy surface scatters (region 6) and after the employment of the statistical classification algorithm were considered high entropy volume type of targets (region 2). Nevertheless, it is not mandatory that pixels classified in region 3 when ICA based ICTD is used follow this pattern. Let us now repeat the test procedure taking into account the POLSAR data set acquired in October 2006 by the E-SAR system over the upper part of the Tacul glacier from the "Chamonix - Mont Blanc" test site, France. Figure 6.7 presents the referred area in Red (HH+VV), Green (HV) and Blue (HH-VV) and the output of the Spherical Symmetry test where in green are represented Non Spherical Symmetric pixels.

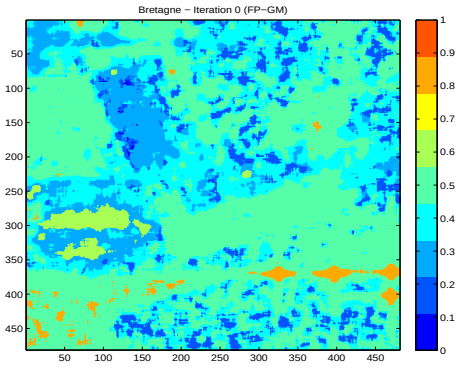
Bretagne − Iteration 0 (FP−GM)

(a)

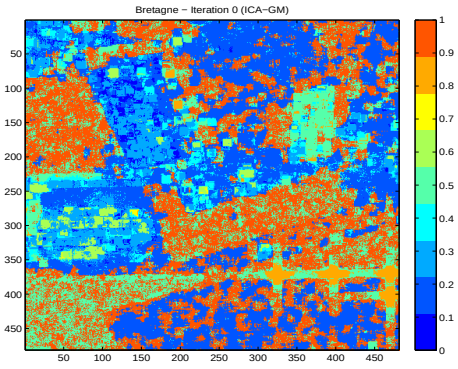
Bretagne − Iteration 0 (ICA−GM)

(b)

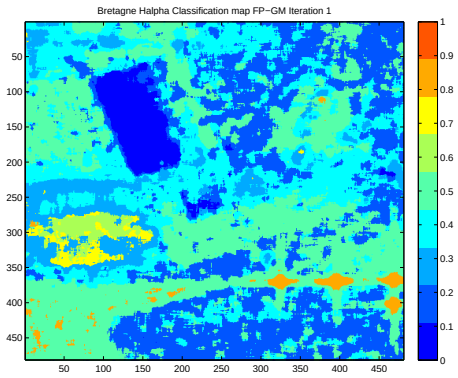
Bretagne Halpha Classification map FP−GM Iteration 1

(c)

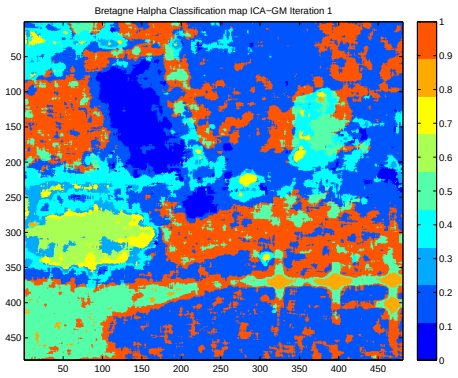
Bretagne Halpha Classification map ICA−GM Iteration 1

(d)

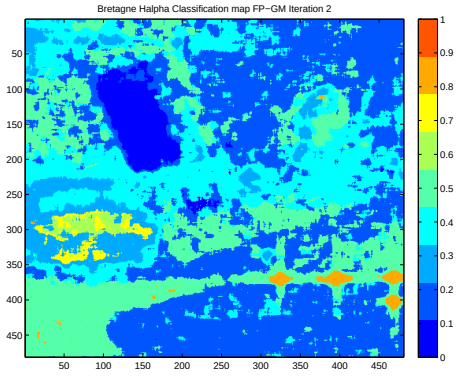
Bretagne Halpha Classification map FP−GM Iteration 2

(e)

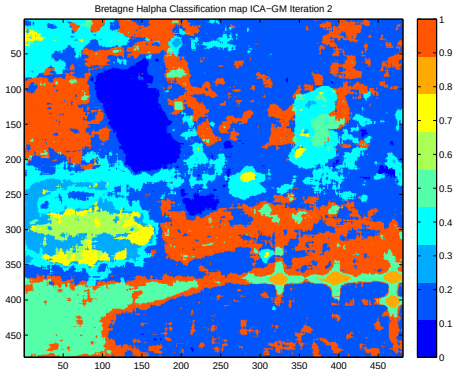
Bretagne Halpha Classification map ICA−GM Iteration 2

(f)

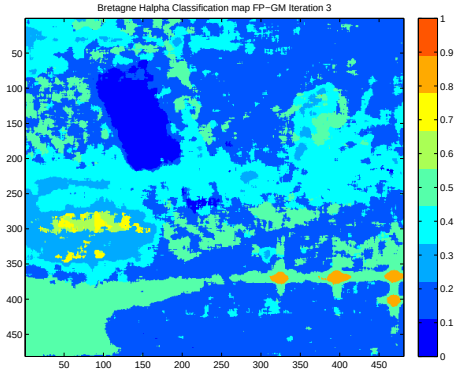
Bretagne Halpha Classification map FP−GM Iteration 3

(g)

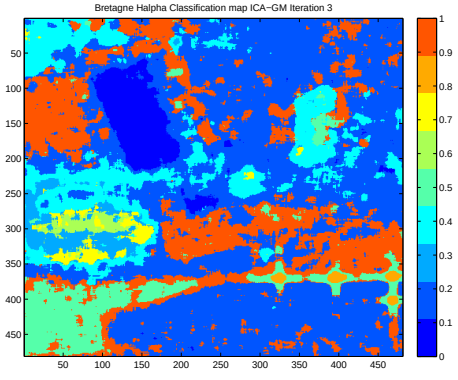
Bretagne Halpha Classification map ICA−GM Iteration 3

(h)

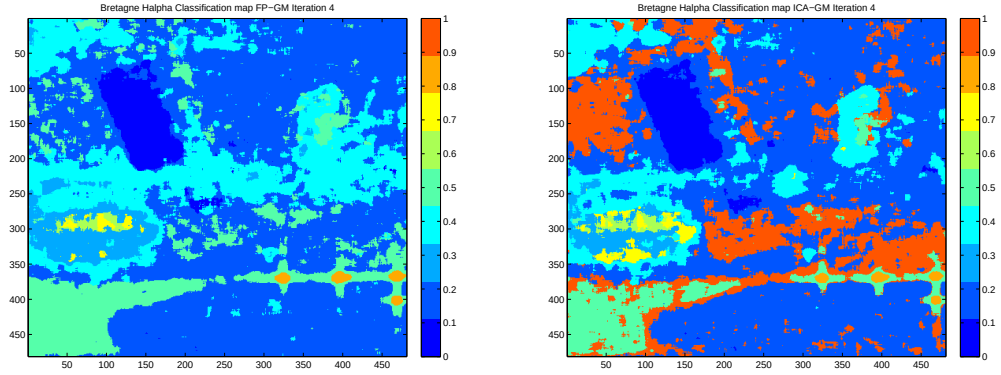

(i) (j)

Figure 6.6: Brétigny area under study: (a) Eigenvector H/α initial population; (b) ICA based ICTD H/α initial population; (c) Eigenvector based statistical classification algorithm output, 1st iteration; (d) ICA based ICTD statistical classification algorithm output, 1st iteration; (e) Eigenvector based statistical classification algorithm output, 2nd iteration; (f) ICA based ICTD statistical classification algorithm output, 2nd iteration; (g) Eigenvector based statistical classification algorithm output, 3rd iteration; (h) ICA based ICTD statistical classification algorithm output, 3rd iteration; (i) Eigenvector based statistical classification algorithm output, 4th iteration; (j) ICA based ICTD statistical classification algorithm output, 4th iteration.

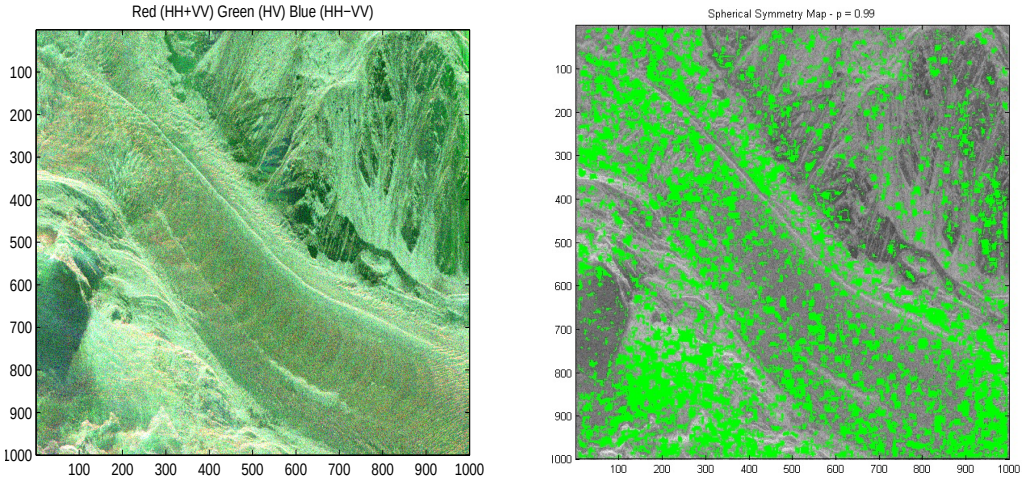

(a) (b)

Figure 6.7: Tacul glacier area under study: (a) RGB image, Red (HH+VV), Green (HV), Blue (HH-VV); (b) Spherical symmetry map.

Note that only a small portion of the pixels in the area under study fails the test (29%), indicating that the SIRV model is also a good representative of this dataset stochastic behaviour. Figure 6.8 presents the initial H/α classification output for both Eigenvector approach and ICA based ICTD, the statistical classification algorithm output after 4 iterations. The corresponding H/α feature spaces are depicted in Figure 6.9.

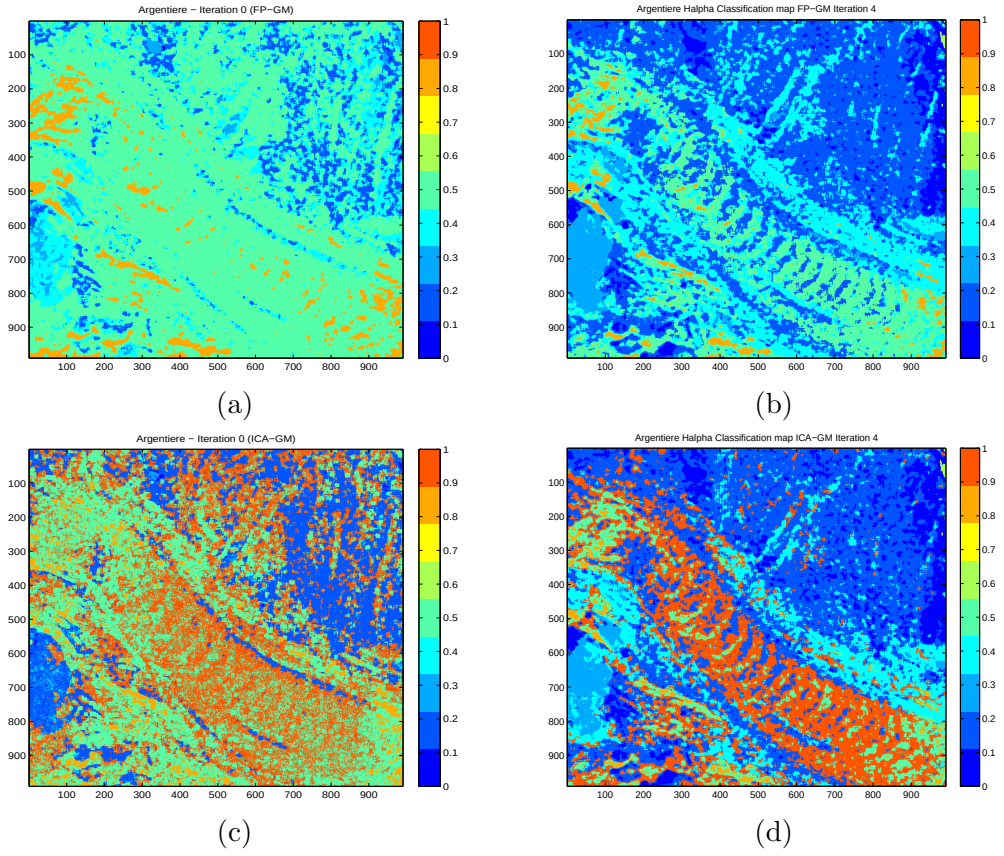

Figure 6.8: Tacul glacier area under study: (a) H/α classification output Eigenvector approach; (b) Statistical classification algorithm output, 4th iteration Eigenvector approach; (c) H/α classification output ICA based ICTD; (d) Statistical classification algorithm output, 4th iteration ICA based ICTD.

The amount of pixels that move from class 6 to class 2 when the Eigenvector approach is employed represents just 34.70% of the set originally classified in region 6. Nevertheless, even though the displacement of pixels between classes 6 and 2 is negligible, scatters represented by region 3 in the H/α feature space not only are still present but also are well clustered, specially after the employment of the statistical classification algorithm. The latter is an evidence that region 3 may be indicating a specific natural phenomenon unable to be represented when the Eigenvector approach is taken into consideration.

Indeed, region 3 is mainly characterizing the pixels that represent the curved stripes due to the "Forbes's bands" phenomena [54, 100], a periodical feature caused by a regularly recurrent displacement of the Tacul glacier during a year. The Forbes's band can be identified in

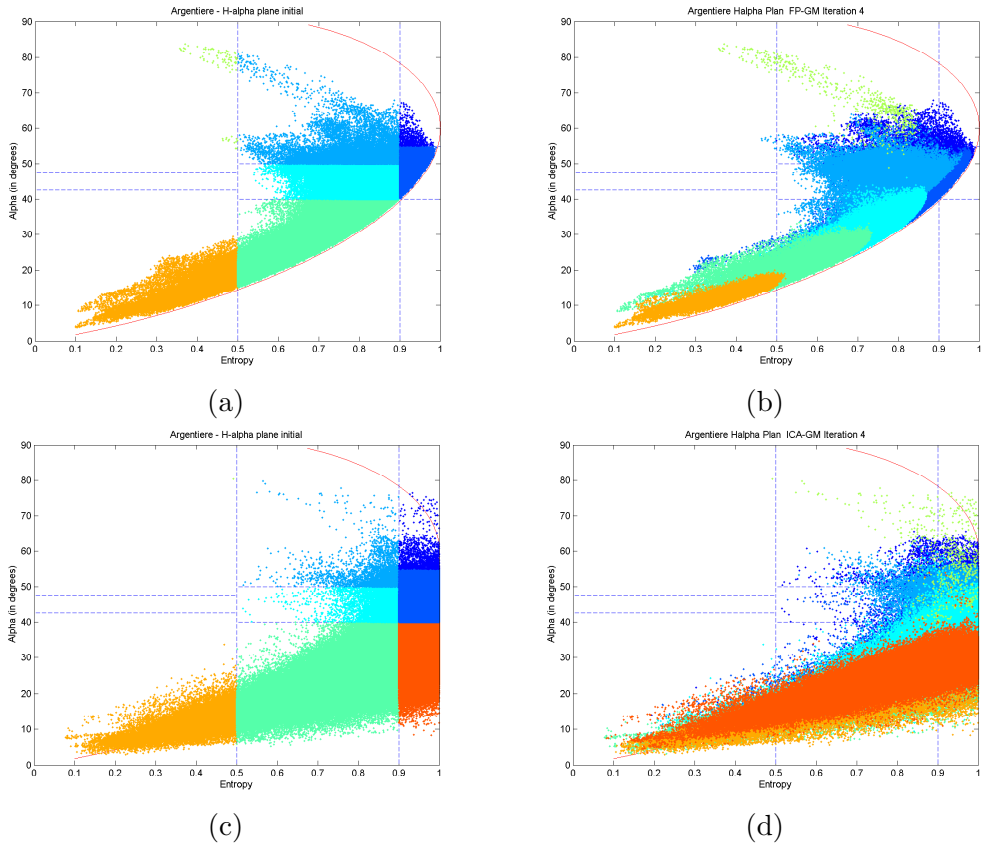

Figure 6.9: Tacul glacier area under study: (a) H/α initial feature space Eigenvector approach; (b) H/α feature space after the 4th iteration Eigenvector aproach; (c) H/α initial feature space ICA based ICTD; (d) H/α feature space after the 4th iteration ICA based ICTD.

Figure 6.8 as the succession of undulations which sweeps transversely across the sensed region. Originally defined in 1842 by Prof. Forbes, as *dirt bands*, the curves pointing downwards the glacier are mainly composed by the accumulation of rocks and dirt that fall on the ice, mostly during summer time. Such impurities affect the grain size and cristallinity characteristics of the ice in its composition (e.g. they prevent the formation of large undisturbed crystals). Therefore, its correct identification/characterization is extremely relevant in the analysis of glacier ice.

In [54], the authors interpreted the corresponding scattering mechanisms as a dominant surface backscatter with low entropy and alpha angles. This is in accordance to what is depicted in Figure 6.8 (see also Figure 6.9). Nevertheless, note that a considerable portion of pixels in this area correspond to class 4 which does not, in theory, explain the physical phenomenon. The ICA approach on the other hand indicates that the aforementioned region is initially better characterized by a high entropy surface backscattering signature, which is unfeasible in the Eigenvector based ICTD using Cloude and Pottier parametrization. Whilst the typical alpha angles estimated using both methods are nearly the same, the entropy

derived with ICA is higher, and the existence of pixels characterized as belonging to class 4 is negligible. If no classification algorithm was employed, it would be already possible to characterize the dirty bands and estimate geophysical parameters related to them taking into consideration only the initial population derived with the ICA based ICTD (using a sliding window approach).

Among other improvements, the statistical classification output clearly delimits the aforementioned regions, increasing the ability to better characterize them. The correct identification of Furthermore, note that the expected behaviour of the dirt bands as they approach the bottoms, is met in the ICA based approach, i.e., they are reduced as the glacier descends until they disappear, which can be observed by the higher amount of pixels classified in class 5 (medium entropy surface) in the bottom of the glacier.

Finally, it is interesting to note that the *snow bands*, are equally classified either using the ICA approach or the traditional Eigenvector based ICTD. The dominant mechanisms of the areas surrounding the dirt bands, where the ice is cleaner is correctly identified as a combination of surface and volume mechanisms (region 2 in the H/α feature space), probably due to a partial penetration of the ice surface in L-band [54]. Once again, note that the transition between the two regions (dirt and snow), is intuitively better represented by region 3 in the H/α feature space, as indicated by the ICA based ICTD approach.

The characterisation of snow parameters based on SAR data analysis is an active research within the scientific community [68, 101, 28, 63]. The snow pack backscattering can contain contributions from four different mechanisms: snow pack surface component, snow volume component, underlying ground surface component and ground volume interaction component. The complex polarimetric signature of such target is a function of both the imaging sensor parameters (e.g., frequency and incident angle) as well as the geophysical characteristics of the snow (e.g., snow density and snow depth), the latter variable over time. Many authors addressed the inversion of snow parameters and the derivation of snow models based on the behaviour of PolSAR datasets acquired, specially, in mountainous regions. Recently, the entropy derived with Eigenvector based ICTD was promisingly associated to the dry snow depth [28]. The authors reported that smaller dry snow packs (relative to the end of winter season) lead to an increase in the entropy. The change in the physical behaviour of the snow scattering mechanism is related to the reduction of the ice crust, which mainly represents strong surface scattering, causing an increase in snow surface and volume backscattering components. As highlighted throughout the present work (mainly in Chapter 4), high entropy type of targets can be incorrectly interpreted when the Eigenvector based ICTD is employed. Therefore, the proposed ICA approach emerges as a promising tool in the study of such scattering mechanisms.

6.2 Tropical Forest Analysis by Means of Touzi TSVM

The effectiveness of the additional information provided by the ICA based ICTD for PolSAR data has already been verified in urban scenarios and in snow environment, as presented in

the previous section and in the works [3, 28]. In the present section we investigate more closely the results and the algorithm performance under tropical forest scenarios, comparing them with the traditional Eigenvector decomposition (also addressed as PCA throughout this thesis).

The characterisation of forested areas is still an open challenge in the SAR community. The high degree of complexity achieved by the returned signal considerably increases the challenge on its analysis [35, 97]. High entropy data is generally expected due to the possible contribution of both surface, double bounce and volume type of scatters, limiting the usage of the widely employed Cloude and Pottier H/α feature space, as discussed in the previous section. Therefore, in this section, the obtained independent target vectors are parameterized using the Target Scattering Vector Model (TSVM) proposed by Touzi [98], allowing the representation of the dominant single scatters on the Poincaré sphere and, consequently, the estimation of its physical properties based on its position on the sphere.

A homogeneous region near the Paracou test site in French Guiana, consisted mainly of tropical forest, is taken into consideration. The data was provided by the Office National d'Études et de Recherches Aérospatiales (ONERA), and was aquired in 2009 in the frame of the European Space Agency campaign TropiSAR. More details about the dataset can be found in Appendix E. In the present analysis we decided to use the output of the classification algorithm (described in the previous section) to define the stationary set of observed Pauli target vectors, rather then relying on the sliding window approach. With no loss of generality, this decision was motivated by the high homogeneity of the data, considerably reducing the dimensionality of the estimation procedure. Figure 6.10 presents the area under study in Red (HH+VV), Green (HV) and Blue (HH-VV) as well as the output of the classification algorithm described in the previous section.

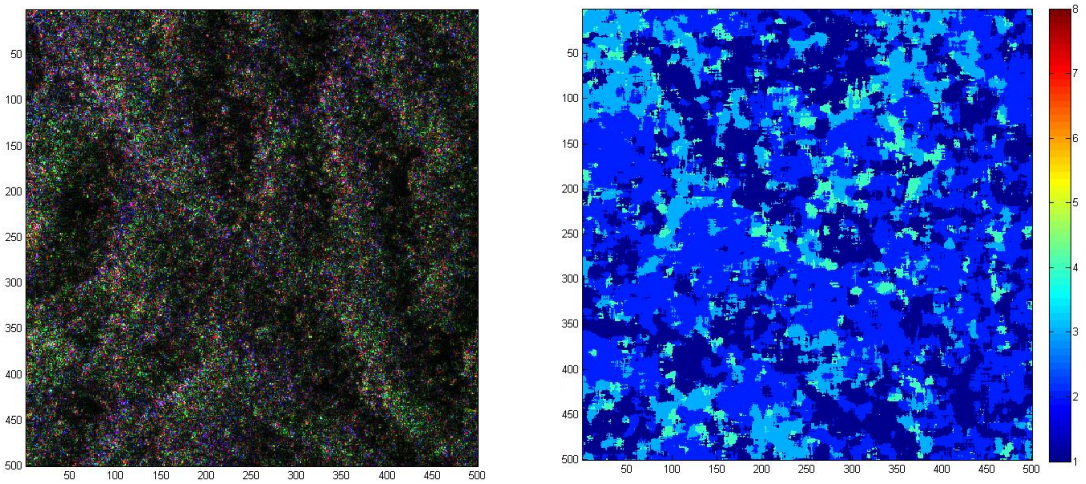

(a) (b)

Figure 6.10: French Guiana area under study: (a) RGB image, Red (HH+VV), Green (HV), Blue (HH-VV); (b) Statistical classification algorithm output.

Each class is analysed using the H/α feature space in order to better interpret and to correlate the estimated TSVM parameters to known type of scatters. Figure 6.11 present the parameters derived with the Eigenvector decomposition and the ICA approach, respectively.

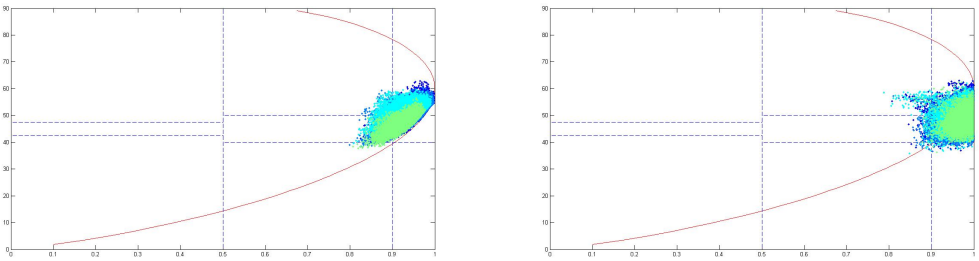

(a) (b)

Figure 6.11: French Guiana area under study: (a) H/α feature space derived using the Eigenvector decomposition; (b) H/α feature space derived using the ICA approach.

As previously addressed in the present chapter, the orthogonality constraint imposed by the eigenvectors, combined with the averaging of the α angle introduces non feasible regions in the H/α plane, delimited by the curves plotted on the graph, which can decrease the performance of the latter in the analysis of high entropy type of targets. As already mentioned, this constraint does not hold for the ICA approach, what can be noted once again for this specific dataset, increasing the dimensionality of possible regions and therefore the analysis itself.

Even though the classes derived with ICA and Eigenvector decomposition, for specific pixels, fall in different regions within the H/α plane, the center of mass of each class indicates nearly the same type of target, that corresponds to the traditional behaviour of forest canopies. Therefore, further investigation on the parameters derived is advised to fully understand the potential in the additional information introduced by the Independent Component Analysis under forested scenarios. Tables 6.1 and 6.2 presents Touzi's TSVM parameters derived for the three main scatters in each class using the Eigenvector decomposition and the ICA approach, respectively.

Analysing the results using the Poincaré sphere, we can conclude that while the Eigenvector decomposition is indicating a mix of basically Cylinder and Dihedral, the ICA approach points out to the presence of Dipoles along with Dihedrals. Both estimations are in accordance to the type of scattering mechanisms generally found in forested scenarios and can be thought of as supplementary information that could lead to a more effective analysis.

Table 6.1: Touzi's parameters derived for the three most dominant component in each class estimated using the Eigenvector approach

	Class I	**Class II**	**Class III**	**Class IV**
Entropy	0.97	0.97	0.96	0.95
τ_{m_1} [°]	2.97	4.35	12.94	2.94
α_{s_1} [°]	17.80	18.35	12.63	15.53
$\phi_{\alpha_{s_1}}$ [°]	38.82	−12.13	35.51	−24.12
τ_{m_2} [°]	12.21	−5.53	−26.07	0
α_{s_2} [°]	69.77	79.20	44.38	78.49
$\phi_{\alpha_{s_2}}$ [°]	44.50	−59.38	78.15	−46.97
τ_{m_3} [°]	−31.26	−2.68	0.79	−3.58
α_{s_3} [°]	82.19	72.88	78.92	78.12
$\phi_{\alpha_{s_3}}$ [°]	3.92	−3.90	−4.41	−10.54

Table 6.2: Touzi's parameters derived for the three most dominant component in each class estimated using the ICA approach

	Class I	**Class II**	**Class III**	**Class IV**
Entropy	0.98	0.99	0.97	0.97
τ_{m_1} [°]	−2.25	−2.95	0.29	0.83
α_{s_1} [°]	35.32	39.10	26.34	43.20
$\phi_{\alpha_{s_1}}$ [°]	−10.81	−8.94	−23.21	−19.71
τ_{m_2} [°]	3.68	19.98	−2.28	4.39
α_{s_2} [°]	47.27	73.72	59.47	36.15
$\phi_{\alpha_{s_2}}$ [°]	−23.42	−61.03	−45.54	−14.95
τ_{m_3} [°]	3.66	0.63	16.40	−15.48
α_{s_3} [°]	77.74	36.20	74.64	71.02
$\phi_{\alpha_{s_3}}$ [°]	33.00	−10.92	−48.77	−46.42

6.3 PolInSAR Experiments

In case of PolInSAR data (see Chapter 2), the same ICA algorithm as described in Chapter 4 can be employed, except that the dimension of the Blind Source Separation problem is increased by two (i.e. $m = 6$). Therefore, (4.10) can be extended to

$$\begin{bmatrix} x_1 \\ x_2 \\ \vdots \\ x_6 \end{bmatrix} = \begin{bmatrix} A_{11} & A_{12} & \cdots & A_{16} \\ A_{21} & A_{22} & \cdots & A_{26} \\ \vdots & \vdots & \ddots & \vdots \\ A_{61} & A_{62} & \cdots & A_{66} \end{bmatrix} \begin{bmatrix} s_1 \\ s_2 \\ \vdots \\ s_6 \end{bmatrix} \tag{6.1}$$

where $\mathbf{x}$ is a set of observation vectors, $\mathbf{A}$ is the mixing matrix and $\mathbf{s}$ is the mutually independent sources vector.

If we introduce the spatially averaged coherency matrix of the POLinSAR observation vector as $\mathbf{T_6}$, the mixing matrix $\mathbf{A}$ can be represented as the factorization of the covariance matrix

$$\mathbf{T_6} = \mathbf{A}\mathbf{A}^H = \begin{bmatrix} \mathbf{T_{11}} & \Omega_{12} \\ \Omega_{12}^H & \mathbf{T_{22}} \end{bmatrix} \tag{6.2}$$

with $\mathbf{T_{11}}$ being the master PolSAR coherency matrix, $\mathbf{T_{22}}$ the slave PolSAR coherency matrix and Ω_{12} the interferometric coherency matrix.

After computing these three matrices from the previously derived mixing matrix, it is now possible to directly apply the PolInSAR coherence optimization proposed in [17]. Figures 6.12 and 6.13 illustrate the coherence optimization results obtained using the proposed ICA based technique. Local sliding neighborhood approach, both in terms of optimized coherence and the associated interferometric phases was employed. One can notice the unwrapped phase is converted to DEM (Digital Elevation Model) using the ambiguity height (around 200m for this PolInSAR data set). The obtained results are in good agreement with the available ground truth (top of the highest building at about 11m). Furthermore, the height difference between the 2nd and the 1st components shows that the two scattering mechanisms (building edge and ground) are well separated in Figure 4-(b). Similar behavior has been reported in [21]. For quantitative performance assessment, the normalized log-ratio [99] between the ICA and PCA derived optimized coherences is computed as

$$R = \sum_{(i,j)\in\mathbf{I}} 20\log\left(\frac{1}{3}\sum_{k=1}^{3}\frac{\rho_k^{opt_{ica}}(i,j)}{\rho_k^{opt_{pca}}(i,j)}\right) \tag{6.3}$$

The ICA revels an improvement in R of exactly 27.05 dB computed over the entire test PolInSAR image (500×500 pixels).

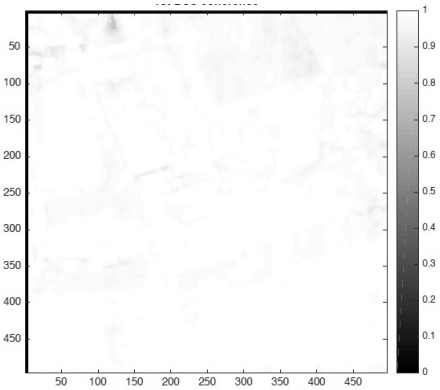

Figure 6.12: Brétigny area under study: ICA optimized coherence - 1st component.

The results depicted in Figure 6.13 are comparable to the ones reported in [22]. In the latter, the authors proposed a time-frequency optimization method based on the wavelet transform, achieving results very close to the ground truth (as obtained using the ICA PolInSAR approach). Therefore, it is possible to conclude that the ICA performance in PolInSAR applications is a promising research area which is worth exploring. Table 6.3 presents the

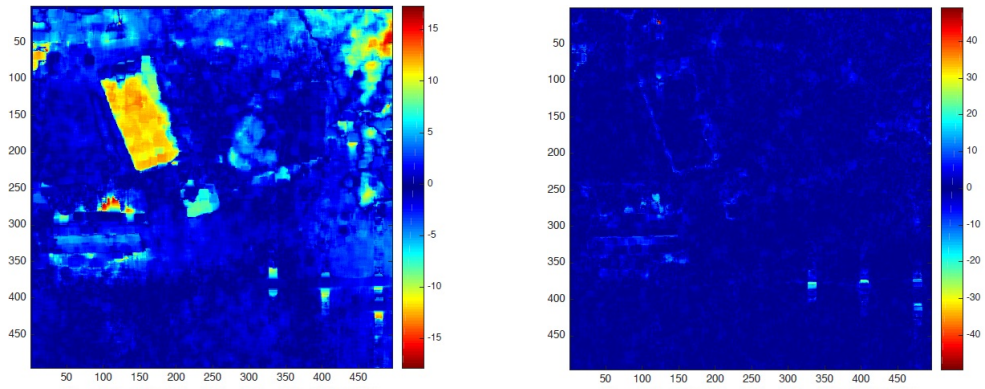

(a) (b)

Figure 6.13: Brétigny area under study: Digital Elevation Model (DEM) after ICA coherence optimization - (a) 1st component, (b) height difference between the 2nd and the 1st component.

height estimation of the three buildings present in the scene under analysis using the two referred methods.

Table 6.3: Height estimation using the ICA based PolInSAR approach and the time-frequency optimization method based on the Wavelet transform.

Method	Building 1	Building 2	Building 3
ICA	11.0	3.0	7.0
Wavelet	10.6	3.4	7.1
Ground Truth	11.5	3.5 to 7	10

6.4 Remarks

In the present chapter, we first addressed the potential new information provided by ICA based ICTD in terms of Cloude and Pottier H/α feature space. A theoretical analysis, performed in Chapter 4, of the limiting curves described in [19] that generate unfeasible regions in the aforementioned plane show that they arise as a consequence of the orthogonality constraint inherent to the coherence matrix eigenvectors, which are associated to the most dominant scatters present in the analysed pixel. Since the ICA based ICTD does not introduce such constraint, examples of possible clutter compositions with non-orthogonal mechanisms that fall outside the Eigenvector approach feasible regions were addressed.

A detailed analysis of a RAMSES X-band image acquired over Brétigny, France revealed that a high number of pixels switch between regions 6 (medium entropy surface scatters) and 2 (high entropy vegetation scatters), when an iterative classification algorithm, based on the stochastic features of the data, is employed. The latter points to the inability of the

Eigevenctor approach to correctly identify the physical phenomenon that lies behind these given pixels. The result of the ICA based ICTD showed that a considerable percentage of these pixels are classified as belonging to region 3 in the H/α plane, that is unfeasible when the Eigenvector approach is employed.

The investigation of the new information provided by the ICA based ICTD was also addressed considering an Alpine region composed mainly by snow. The results showed that the reported pattern of changing pixels between region 6 and region 2 does not always stand. Nevertheless, clusters composed by pixels represented by region 3 in the H/α plane are still formed and they represent very well defined areas in the observed scene, corresponding to the Forbes's band phenomenom. This suggests that the ICA approach is a promising tool in the study of such scattering mechanisms, increasing the analysis performance of glacier complex surface and sub-surface which are made of rocks, snow and ice.

The performance and the additional information provided by the Independent Component Analysis approach to ICTD in forested area scenarios was also evaluated. Accounting for the difficulty in relating the derived parameters to ground truth, it was shown the differences between the aforementioned method and the traditional Eigenvector decomposition by means of a detailed comparison using Cloude and Pottier's H/α feature space and Touzi's TSVM parameters derived with both approaches.

In the analysis of the considered forested area, even though the ICA and Eigenvector decomposition indicate different regions for some specific pixels, the average scattering mechanism remains nearly the same, highly influenced by the forest canopies. The analysis on Touzi's TSVM parameters revealed that both approaches, ICA and Eigenvector decomposition, indicate the strong presence of Dihedral type of scatters in the scene. Nevertheless, while the latter is indicating the presence of Cylinders along with Dihedrals, the former points out to the existence of Dipoles in the analysed data.

The results obtained point to the high potential of ICA based ICTD with respect to the analysis of high entropy type of scatters. Even though it is a common sense in SAR community that polarimetry is a better suited tool to analyse low entropy type of targets, the ability to correctly estimate the parameters that describe the illuminated scatters is crucial. Therefore, any constraint that prevent this to happen decreases the performance of any classification, detection and geophysical parameter inversion algorithms.

With respect to the PolInSAR experiments carried on, the obtained results show improvements in terms of the derived optimized coherences and, in the same time, they remain consistent with the actual ground truth. It is important to highlight that, as already reported in [93], in the original PolInSAR formulation proposed in [17], the phase centers separation, corresponding to different scatters, is carried out by decomposing the data into three orthogonal components. Nevertheless, the performance of such algorithm is directly associated to the assumption about the presence of orthogonal deterministic scattering mechanisms, which, as already approached throughout this thesis does not hold for forested scenarios. In [77] the same authors formulated a more sophisticated model based inversion algorithm for forest parameter estimation. This approach was not considered in the present work, nevertheless,

the analysis of its result combined with the Independent Component Analysis based ICTD is highly recommended for future works possibilities.

Finally, it is important to highlight that ICA proved itself very useful as an ICTD method by introducing an alternative way of physically interpreting a polarimetric SAR image which, unlike Eigenvector decomposition (PCA), estimates average mechanisms not constrained to any orthogonality among them. The new information provided by ICA based ICTD with respect to Cloude and Pottier H/α feature space can be further investigated in many different applications, specially the ones related to surface type of scatters. A study of the relation between the new parameters retrieved and soil roughness is a promising research area. The analysis of sea ice with the help of the H/α plane [88, 89], is another application that may also benefit from the additional information provided. Such type of clutter may present high degree of depolarisation which, despite being mainly associated to volume type of scatters, may be also due to rough and highly deformed ice, which is in fact a physical phenomenon inherent to surface mechanisms [30, 36]. Therefore, it is expected that the polarimetric behaviour of sea ice is better represented by region 3 in the H/α plane since it, intuitively, reflects more accurately a physical phenomenon corresponding to a clutter composed by both surface and volume scatters.

It is important to highlight that the applied classification was unsupervised, therefore the correspondence to ground truth may not be strictly exact. It is common sense in SAR community that the evaluation of unsupervised classification is a challenging task, due to the high degree of complexity in relating, physically and unambiguously, classes to the ground truth data [35]. Furthermore ground truth data in tropical forest/snow covered scenarios is scarce and generally incomplete due to the difficulty in accessing and performing in situ measurements.

The main caveat related to ICA is that since it has been recently introduced as an ICTD approach to SAR image analysis, it is still difficult to assert if there are specific scenarios where ICA performance is higher than Eigenvector's. Alternatively, the authors believe that the additional information introduced by ICA can be combined with the information provided by the Eigenvector decomposition in order to better propose, among others, classification and geophysical parameter inversion algorithms.

Chapter 7

Conclusion

In the present work several aspects of highly heterogeneous PolSAR clutter analysis (inherent to high resolution polarimetric SAR systems) were addressed. First, the validity of the product model (SIRV) when employed to characterise multivariate PolSAR data was verified. A new methodological framework to assess the conformity of multivariate high-resolution PolSAR data model in terms of asymptotic statistics was presented. Statistical hypotheses testing on the structure of the quadricovariance matrix was performed in order to investigate if samples from an homogeneous region constitute an elliptical symmetric dataset, the latter being true if the aforementioned model holds. Simulations with synthetic data and a detailed analysis over real data were performed.

The analysis with synthetic data asserts for the effectiveness and consistency of the proposed test derived, showing that the latter is able to correctly identify regions from which the samples do not present elliptical symmetry and, as a consequence, do not fit the Spherically Invariant Vector model. The performance of the test was verified for different confidence levels and window sizes, indicating the importance in properly choosing these parameters for better and not biased results. Finally, it was verified that under SIRV assumption the test output is in accordance with the expected, rejecting regions composed by samples that present high indexes of non-stationarity (borders), aside from outliers.

Prior to the quantitative analysis with real data, the consistency of the test with respect to a temporal coherent dataset was also verified, evidencing its robustness. Next, the investigation of the test outcome with varied datasets (see figures (3.7) and (3.9)) showed that the rate of rejected pixels is not negligible in specific types of scenarios. The forested area investigated here presented 30% of pixels that do not fit the product model. It is important to highlight that the applied classification used as an additional tool to better illustrate the regions where the model fails was unsupervised, therefore the correspondence to ground truth may not be strictly exact. Even though the lack of precise ground truth can limit the assertion of what is causing the product model to fail, the main objective of the present analysis was to show that by proving the correctness of test (by means of a detailed mathematical derivation and an analysis with a synthetic dataset) and by applying it to real datasets with different sensor characteristics, we could be able to indicate that the amount of pixels that fail the model can be non negligible, requiring extra attention in their analysis.

In short, a considerable portion of high heterogeneous data may not fit the Spherically Invariant Random Vector model (product model). Therefore, traditional detection and clas-

sification algorithms developed based on the latter become sub-optimal when applied in such kind of regions, highlighting for the need of either updating the model to one that associates an individual texture variable with each polarimetric channel [35], or the development of model independent algorithms, like the Independent Component Analysis (ICA), proposed in [3].

The former, introduces a high degree of complexity in modelling PolSAR data and, consequently in deriving proper algorithms suited for such models. Furthermore, providing unique models when multi-texture assumption is taken into consideration is a challenge very difficult to came across. The ICA, on the other hand, being a blind source separation technique, based on higher order statistical moments, aims in recovering statistical independent sources without having any physical background of the mixing process [48]. Therefore, it is a model independent strategy to analyse the behaviour of non-Gaussian heterogeneous clutters (inherent to high resolution SAR systems) which proved itself very useful and introduces an alternative way of physically interpreting a polarimetric SAR image.

In the present work, we also focused on addressing and quantifying the two main drawbacks of the employment of Independent Component Analysis in polarimetric target decomposition: the higher amount of samples needed and the assumption of non-Gaussian clutter. Based on simulated data we managed to better investigate the theoretical concepts and quantify the bias on the entropy and Touzi's parameters caused by insufficient number of samples used in their estimation.

It was shown that when the averaged or most dominant scattering mechanisms that characterises the heterogeneous clutter are orthogonal, Touzi's parameters estimated using ICA are the same as the ones estimated using Eigenvector decomposition and the convergence rate of the estimation is nearly the same. When the clutter is composed by non-orthogonal mechanisms, unlike Eigenvector decomposition, ICA successfully derive the basic scattering mechanisms without compromising its performance.

Simulations with complex type of scatters, Volume, Double-Bounce and Surface, whose characteristic were extracted from real data, heterogeneous clutter with Gaussian sources and with spatial correlation showed similar results, giving strength to the proposal of using a sliding window size of 11×11 in ICA based ICTD approach.

Reducing the theoretical gap involving ICA based ICTD, enables a considerable increase in its usage. Within this context, the potential new information provided by ICA based ICTD in terms of Cloude and Pottier H/α feature space was verified. A theoretical analysis of the limiting curves described in [19] that generate unfeasible regions in the aforementioned plane show that they arise as a consequence of the orthogonality constraint inherent to the coherence matrix eigenvectors, which are associated to the most dominant scatters present in the analysed pixel. Since the ICA based ICTD does not introduce such constraint, examples of possible clutter compositions with non-orthogonal mechanisms that fall outside the Eigenvector approach feasible regions were addressed.

A detailed analysis with real data revealed an interesting property of ICA based ICTD

that is unmatchable by the Eigenvector approach: the ability to classify targets as corresponding to Zone 9 in the aforementioned feature space. ICA performance was also verified under forested scenarios indicating similar average scatters as the Eigenvector approach, but rather supplementary scattering mechanisms when Touzi TSVM was taken into consideration. Finally, the present work presented a new framework for applying BSS techniques with POLinSAR data for polarimetric coherence optimization and associated interferometric phases estimation. The obtained results show improvements in terms of the derived optimized coherences and, in the same time, they remain consistent with the actual ground truth.

The main caveat related to ICA is that since it has been recently introduced as an ICTD approach to SAR image analysis, it is still difficult to assert if there are specific scenarios where ICA performance is higher than Eigenvector's. Alternatively, the authors believe that the additional information introduced by ICA can be combined with the information provided by the Eigenvector decomposition in order to better propose, among others, classification and geophysical parameter inversion algorithms.

Finally, as a by-product of this work, closed form expressions for the fourth and sixth order moments of Complex Normal distributed random vector were derived and extended to Complex Elliptical Symmetric distributions, along with consistent estimators.

To increase the contribution of the subjects presented in this thesis to the scientific community, the authors would like to enumerate some future work possibilities, which are, in some extent, already being addressed by the latter. Even though the two major research axes investigated throughout the present work were combined in an analysis of high resolution PolSAR data, they can also be addressed separately. That is why we shall divide future work suggestions considering them as distinct fields.

Regarding the stochastic assessment of high resolution PolSAR clutter models, the authors believe that the consistency of the proposed test can be further stressed. A closer verification of its performance under mixture models and different probabilistic models assumption (other than K-distribution), and a detailed comparison with the results achieved by the original Schott test for real multivariate random data are subjects that could be exploited. This may lead to a considerable increase in the range of possible remote sensing applications (not to mention different communication systems other than radar) in which it could be employed.

Since the proposed Wald test probabilistic distribution is asymptotically chi-squared, it is expected that for each window size the test distribution presents a departure from the chi-squared one, as a function of the number of samples being used in the statistics derivation. Therefore, another interesting analysis would be the closer investigation of this phenomenon and the derivation of the most appropriate test statistic as a function of the window size being employed.

Associating the proposed method to other stochastic tests of multivariate PolSAR data is also an interesting approach that could be analysed. Circularity and sphericity are probabilistic properties whose usefulness have already been verified by previous works. Within this context, a general framework could be proposed, combining them all on a single, more

complete analysis.

Identifying and better characterising SAR data that do not fit the SIRV model based on the imaged region or the sensor properties are also key factors to propose more efficient detection, estimation and inversion of geophysical parameters algorithms. Once this step is done, updating the model should be considered, taking into account either a polarization dependent scenario or a model not based on a texture/speckle architecture.

Finally, on the other hand, even though ICA based ICTD has been proving itself as a promising research field in PolSAR data analysis, there are many theoretical assessment that still need to be addressed with respect to its proper employment in target decomposition. Its performance for different types of scatters, different mixtures and considering clutters characterised by varied stochastic models, are examples of subjects that still need to be exhausted.

Furthermore, the results achieved when taking into consideration real data still need to be better understood. Varied scenarios should be investigated and, if possible, geophysical properties of the scene under study should be precisely associated to the ICA estimated components. Within this context, a joint use along with the Eigenvector approach could be investigated instead of a simple stand alone employment.

Finally, an interesting advantage of the ICA based ICTD worth of investigation is its ability to identify more than three sources, which is something that the Eigenvector approach can not do. Since many model based incoherent target decompositions highlight for the existence of multiple sources (more than three), it is clear that ICA can get closer to them when compared to the eigenvector approach, increasing the range of applications where it could be more efficiently employed.

Appendix A

Fourth order and sixth order matrices of Complex Normal Distributions

In this section we extend the derivation performed in [66] of the fourth and sixth order moments of real-valued random vectors with normal distribution to complex-valued variables.

Let u be an m x 1 vector with a complex normal distribution $u \sim CN(0, I_m)$, where I_m is the m x m identity matrix. Then, its fourth order moment N_4 and its sixth order moment N_6 are respectively given by

$$N_4 = E[uu^H \otimes uu^H] \tag{A.1}$$

and

$$N_6 = E[uu^H \otimes uu^H \otimes uu^H] \tag{A.2}$$

where $E[x]$ is the expected value of x, $\otimes$ is the Kronecker product and $\cdot^H$ is the complex transpose operator.

In order to derive (A.1) and (A.2) let us first remember that

$$E[u_i u_j^* u_k u_l^*] = \begin{cases} 2 & \text{if } i = j = k = l; \\ 1 & \text{if } i = j,\ k = l,\ i \neq k; \\ 0 & \text{if } i \neq j \text{ or } k \neq l. \end{cases} \tag{A.3}$$

Therefore, it is straightforward to note that

$$E[u_i u_j^* \cdot uu^H] = E_{ji} + \delta_{ij} I_m \tag{A.4}$$

where $E_{ij} = e_i e_j$ is a m x m matrix with e_i being the ith column of the identity matrix I_m and δ_{ij} is the Kronecker delta, given by

$$\delta_{ij} = \begin{cases} 1 & \text{if } i = j; \\ 0 & \text{if } i \neq j. \end{cases} \tag{A.5}$$

Hence, the fourth order moment of u is given by

$$E[uu^H \otimes uu^H] = \sum_{ij} [E_{ij} \otimes (E_{ji} + \delta_{ij} I_m)] \tag{A.6}$$

Note that (A.6) can be rewritten as

$$E[uu^H \otimes uu^H] = \sum_{ij} E_{ij} \otimes E_{ji} + \sum_{i} E_{ii} \otimes I_m \tag{A.7}$$

Finally, according to the properties of commutation matrices reported in [66], (A.7) reduces to

$$E[uu^H \otimes uu^H] = K_{mm} + I_m \otimes I_m \tag{A.8}$$

where K_{mm} is an m x m commutation matrix [66].

The derivation of N_6 is carried out in a similar fashion. Let

$$E[u_i u_j^* u_k u_l^* \cdot uu^H] = \begin{cases} 0 & \text{if } i \neq j \neq k \neq l; \\ E_{lk} & \text{if } i = j,\ k \neq l; \\ I_m + E_{ii} + E_{kk} & \text{if } i = j,\ k = l,\ i \neq k; \\ 2E_{li} & \text{if } i = j,\ k \neq l; \\ 2I_m + 4T_{ii} & \text{if } i = j = k = l. \end{cases} \tag{A.9}$$

where $T_{ij} = E_{ij} + E_{ji}$

Hence,

$$E\left[u_i u_j^*(uu^H \otimes uu^H)\right] = \begin{cases} \sum_{kl}(E_{kl} \otimes E_{lk}) + I_m \otimes E_{ii} + I_m \otimes I_m + E_{ii} \otimes I_m + \\ \sum_{l}(E_{il} \otimes E_{li} + E_{li} \otimes E_{il}) & \text{if } i = j; \\ I_m \otimes E_{ji} + E_{ji} \otimes I_m + \sum_{l}(E_{li} \otimes E_{jl} + E_{jl} \otimes E_{li}) & \text{if } i \neq j. \end{cases}$$

Therefore, it is possible to write

$$E\left[u_i u_j^*(uu^H \otimes uu^H)\right] = \delta_{ij}\left[\sum_{kl}(E_{kl} \otimes E_{lk}) + I_m \otimes I_m\right] + I_m \otimes E_{ji} + E_{ji} \otimes I_m + \sum_{l}(E_{li} \otimes E_{jl} + E_{jl} \otimes E_{li}) \tag{A.10}$$

Finally, knowing that $E[uu^H \otimes uu^H \otimes uu^H] = \sum_{ij}\left[E_{ij} \otimes \left(E\left[u_i u_j^*\left(uu^H \otimes uu^H\right)\right]\right)\right]$, the sixth order moment of complex normal random vectors with zero mean and identity covariance matrix is given by

$$N_6 = I_m \otimes I_m \otimes I_m + I_m \otimes K_{mm} + \sum_{ij} E_{ij} \otimes I_m \otimes E_{ji} + \sum_{ij} E_{ij} \otimes E_{ji} \otimes I_m + \sum_{ijl} E_{ij} \otimes (E_{li} \otimes E_{jl} + E_{jl} \otimes E_{li}) \tag{A.11}$$

Appendix B

Derivation of the vectorised version of the standardised quadricovariance

In order to derive a simplified vectorised form of $\widehat{[M]}_{4*}$ it is necessary to expand (3.11) accordingly. Let us assume that $A = \widehat{[M]} - [M]$, $C = \widehat{[M]}_4 - [M]_4$, and that it is possible to write

$$[M]^{-1/2^H} A [M]^{-1/2} = B^H [M]^{-1/2} + [M]^{-1/2^H} B \tag{B.1}$$

where $B = [M]^{-1/2} - \widehat{[M]}^{-1/2} + O_p(n^{-1/2})$. Hence, expanding (3.11), it comes down to

$$\begin{aligned}\widehat{[M]}_{4*} = &\left[\left([M]^{-\frac{1}{2}^H} - B^H\right) \otimes \left([M]^{-\frac{1}{2}^H} - B^H\right)\right] [M]_4 \left[\left([M]^{-\frac{1}{2}} - B\right) \otimes \left([M]^{-\frac{1}{2}} - B\right)\right] + \\ &\left[\left([M]^{-\frac{1}{2}^H} - B^H\right) \otimes \left([M]^{-\frac{1}{2}^H} - B^H\right)\right] C \left[\left([M]^{-\frac{1}{2}} - B\right) \otimes \left([M]^{-\frac{1}{2}} - B\right)\right]\end{aligned} \tag{B.2}$$

Let S_2 denote the second term in (B.2). Note that it is given by

$$\begin{aligned} S_2 &= \left[\left([M]^{-\frac{1}{2}^H} - B^H\right) \otimes \left([M]^{-\frac{1}{2}^H} - B^H\right)\right] C \left[\left([M]^{-\frac{1}{2}} - B\right) \otimes \left([M]^{-\frac{1}{2}} - B\right)\right] \\ &= \left([M]^{-\frac{1}{2}^H} \otimes [M]^{-\frac{1}{2}^H}\right) C \left([M]^{-\frac{1}{2}} \otimes [M]^{-\frac{1}{2}}\right) + O_p(n^{-1/2}) \end{aligned} \tag{B.3}$$

Likewise, let us refer to the first term as S_1, then, expanding S_1, knowing (3.9), we get

$$\begin{aligned} S_1 = (1+\omega) \Big\{ &\left([M]^{-\frac{1}{2}^H} \otimes [M]^{-\frac{1}{2}^H}\right) \left[\left(I_{m^2} + K_{mm}\right) \left([M] \otimes [M]\right)\right] \left([M]^{-\frac{1}{2}} \otimes [M]^{-\frac{1}{2}}\right) + \\ &\left([M]^{-\frac{1}{2}^H} \otimes [M]^{-\frac{1}{2}^H}\right) \left[\left(I_{m^2} + K_{mm}\right) \left([M] \otimes [M]\right)\right] \left[-B \otimes [M]^{-\frac{1}{2}} - [M]^{-\frac{1}{2}} \otimes B\right] + \\ &\left[-B^H \otimes [M]^{-\frac{1}{2}^H} - [M]^{-\frac{1}{2}^H} \otimes B^H\right] \left[\left(I_{m^2} + K_{mm}\right) \left([M] \otimes [M]\right)\right] \left([M]^{-\frac{1}{2}} \otimes [M]^{-\frac{1}{2}}\right) + O_p(n^{-1/2}) \Big\} \end{aligned} \tag{B.4}$$

The distributions of both terms (B.3) and (B.4) do not depend on $[M]$ [90], therefore it can be assumed for the sake of simplicity and without loss of generality that $[M] = I_m$,

yielding $S_2 = C$ and

$$S_1 = (1+\omega)\Big\{(I_{m^2} + K_{mm}) + (I_{m^2} + K_{mm})\left[-B \otimes I_m - I_m \otimes B\right] + \left[-B^H \otimes I_m - I_m \otimes B^H\right](I_{m^2} + K_{mm}) + O_p(n^{-1/2})\Big\} \tag{B.5}$$

Using basic properties of the commutation matrix, the commutation property of the Kronecker product [66], and (B.1), (B.5) reduces to

$$S_1 = (1+\omega)\left\{N_4 - (I_{m^2} + K_{mm})\left[I_m \otimes A + A \otimes I_m\right]\right\} \tag{B.6}$$

Finally, using (B.3) and (B.6), (B.2) can be rewritten as

$$\widehat{[M]}_{4*} = (1+\omega)N_4 + C - (1+\omega)(I_{m^2} + K_{mm})\left[I_m \otimes A + A \otimes I_m\right] \tag{B.7}$$

where $[N]_4$ is what $[M]_4$ simplifies to when $k_i \sim CN_m(0, I_m)$, derived in the previous section (see (A.8)).

The vectorised version of (B.7) is then obtained in a straightforward manner as

$$\mathrm{vec}(\widehat{[M]}_{4*}) = (1+\omega)\mathrm{vec}([N]_4) + \mathrm{vec}(C) - (1+\omega)H\mathrm{vec}(A) + O_p(n^{-1/2}) \tag{B.8}$$

where $\mathrm{vec}(\cdot)$ is the operator that transforms a matrix into a column vector [66], and H is an operator given by

$$H = [I_{m^2} \otimes (I_{m^2} + K_{mm})] \cdot \{I_m \otimes [(K_{mm} \otimes I_m) \cdot (I_m \otimes \mathrm{vec}(I_m))] + [(I_m \otimes K_{mm}) \cdot (\mathrm{vec}(I_m) \otimes I_m)] \otimes I_m\} \tag{B.9}$$

Appendix C

Rank of the covariance matrix Φ

According to [90], the degrees of freedom of the proposed Wald test is equal to the rank of Φ (see (3.16)) and is set according to the unknowns of the quadricovariance matrix (3.9), being the latter minus 1. For the sake o completeness, we derive the degrees of freedom for $m > 3$, m being the dimension of the mulivariate random variable k and show that it also applies to $m = 3$, more suited to PolSAR applications where the reciprocity theorem applies.

Note that when performing $kk^H \otimes kk^H$ one can get seven different unknowns, which, along with their number of occurrences are given in Table C.1.

Table C.1: Unknowns of the quadricovariance matrix and respective number of occurrences

Unknown	**Number of occurrences**
$k_i k_i^* \cdot k_i k_i^*$	m
$k_i k_j^* \cdot k_i k_j^*$	$\binom{m}{2}$
$k_i k_j^* \cdot k_j k_i^*$	$\binom{m}{2}$
$k_i k_i^* \cdot k_i k_j^*$	$m(m-1)$
$k_i k_i^* \cdot k_j k_i^*$	$m(m-1)$
$k_i k_i^* \cdot k_j k_p^*$	$m\binom{m-1}{2}$
$k_i k_j^* \cdot k_i k_p^*$	$m\binom{m-1}{2}$
$k_i k_j^* \cdot k_p k_q^*$	$\binom{m}{4}$

Therefore, since the degrees of freedom f is the total number of unknowns minus 1, it can be shown to be

$$f = m^2 + \frac{m(m-1)(m^2+19m+6)}{24} - 1 \tag{C.1}$$

Note that if $m = 3$, the last unknown in Table C.1 does not exist, corresponding to a zero number of occurrences, while if $m = 2$ (dual pol configuration), the last three terms are discarded (nulls) and for both cases (C.1) still holds.

Appendix D

Touzi's TSVM estimation for special cases

Let the estimated mixing matrix be given, in Pauli basis, by

$$\mathbf{A} = \begin{bmatrix} |a_1|e^{\gamma_1} \\ |a_2|e^{\gamma_2} \\ |a_3|e^{\gamma_3} \end{bmatrix} = \begin{bmatrix} a_{r_1} + a_{i_1} \\ a_{r_2} + a_{i_2} \\ a_{r_3} + a_{i_3} \end{bmatrix} \tag{D.1}$$

The intuitive flow of an estimation algorithm of Touzi's parameters described in (4.3) would be first the derivation of m and $|e_T|_m$ from the Graves matrix and the norm of the mixing matrix, respectively. Then, the estimation of ϕ_s taken as the phase argument of the first element of the mixing matrix $\mathbf{A}$, γ_1. Next, the rotation angle ψ is addressed, and removed by multiplying the mixing matrix by the matrix $\mathbf{W}$, described in (D.2), leading finally to the estimation of the roll-invariant parameters τ_m, α_s and ϕ_{α_s}. Even though the described procedure seems straightforward, some specific cases need extra attention.

$$\mathbf{W} = \begin{bmatrix} 1 & 0 & 0 \\ 0 & \cos(-2\psi) & -\sin(-2\psi) \\ 0 & \sin(-2\psi) & \cos(-2\psi) \end{bmatrix} \tag{D.2}$$

Assuming that m and $|e_T|_m$ are correctly estimated, it is possible to write from (4.3) that

$$\begin{aligned} A' = \begin{bmatrix} a'_{r_1} + a'_{i_1} \\ a'_{r_2} + a'_{i_2} \\ a'_{r_3} + a'_{i_3} \end{bmatrix} = \\ \begin{bmatrix} \cos(\alpha_s)\cos(2\tau_m)\cos(\phi_s) \\ \cos(2\psi)\sin(\alpha_s)\cos(\phi_s + \phi_{\alpha_s}) - \sin(2\psi)\cos(\alpha_s)\sin(2\tau_m)\sin(\phi_s) \\ \sin(2\psi)\sin(\alpha_s)\cos(\phi_s + \phi_{\alpha_s}) + \cos(2\psi)\cos(\alpha_s)\sin(2\tau_m)\sin(\phi_s) \end{bmatrix} + \\ j \cdot \begin{bmatrix} \cos(\alpha_s)\cos(2\tau_m)\sin(\phi_s) \\ \cos(2\psi)\sin(\alpha_s)\sin(\phi_s + \phi_{\alpha_s}) + \sin(2\psi)\cos(\alpha_s)\sin(2\tau_m)\cos(\phi_s) \\ \sin(2\psi)\sin(\alpha_s)\sin(\phi_s + \phi_{\alpha_s}) - \cos(2\psi)\cos(\alpha_s)\sin(2\tau_m)\cos(\phi_s) \end{bmatrix} \end{aligned} \tag{D.3}$$

where $A' = \frac{A}{m|e_T|_m}$.

Note from (D.3) that if the first element of A' is zero, then ϕ_s is undetermined. This can occur if either $\tau_m = \pm 45^\circ$ or if $\alpha_s = \pm 90^\circ$. Since ϕ_s is a parameter only used in interferometric applications, this conclusion could be, at first, neglected, nevertheless an incorrect estimation of ϕ_s can lead to incorrect estimation of other parameters. Let us analyse the consequences of this misestimation of ϕ_s for each of the described situations. Taking $\tau_m = \pm 45^\circ$, (D.3) reduces to

$$\begin{aligned} A' = \begin{bmatrix} a'_{r_1} + a'_{i_1} \\ a'_{r_2} + a'_{i_2} \\ a'_{r_3} + a'_{i_3} \end{bmatrix} = \\ \begin{bmatrix} 0 \\ \cos(2\psi)\sin(\alpha_s)\cos(\phi_s + \phi_{\alpha_s}) \mp \sin(2\psi)\cos(\alpha_s)\sin(\phi_s) \\ \sin(2\psi)\sin(\alpha_s)\cos(\phi_s + \phi_{\alpha_s}) \pm \cos(2\psi)\cos(\alpha_s)\sin(\phi_s) \end{bmatrix} + \\ j \cdot \begin{bmatrix} 0 \\ \cos(2\psi)\sin(\alpha_s)\sin(\phi_s + \phi_{\alpha_s}) \pm \sin(2\psi)\cos(\alpha_s)\cos(\phi_s) \\ \sin(2\psi)\sin(\alpha_s)\sin(\phi_s + \phi_{\alpha_s}) \mp \cos(2\psi)\cos(\alpha_s)\cos(\phi_s) \end{bmatrix} \end{aligned} \tag{D.4}$$

Even thought the helicity (τ_m), and the scattering type parameters (α_s and ϕ_{α_s}) are roll invariant, it is imperative that the rotation angle is correctly estimated. Let us write (D.4) in terms of linear equations, neglecting a'_{r_1} and a'_{i_1} that are zero.

$$\begin{aligned} a'_{r_2} &= \cos(2\psi)\sin(\alpha_s)\cos(\phi_s + \phi_{\alpha_s}) \mp \sin(2\psi)\cos(\alpha_s)\sin(\phi_s) \\ a'_{r_3} &= \sin(2\psi)\sin(\alpha_s)\cos(\phi_s + \phi_{\alpha_s}) \pm \cos(2\psi)\cos(\alpha_s)\sin(\phi_s) \\ a'_{i_2} &= \cos(2\psi)\sin(\alpha_s)\sin(\phi_s + \phi_{\alpha_s}) \pm \sin(2\psi)\cos(\alpha_s)\cos(\phi_s) \\ a'_{i_3} &= \sin(2\psi)\sin(\alpha_s)\sin(\phi_s + \phi_{\alpha_s}) \mp \cos(2\psi)\cos(\alpha_s)\cos(\phi_s) \end{aligned} \tag{D.5}$$

Note that (D.5) can only be solved for ψ in three special cases: i. $\alpha_s = 0^\circ$; ii. $\alpha_s = 45^\circ$ and $\phi_{\alpha_s} = 0^\circ$ and iii. $\alpha = \pm 90^\circ$, the latter, independently of the value of τ_m.

If $\alpha_s = 0^\circ$, as in Dihedral 45° type of targets, the following equality holds for ψ

$$2\psi = \begin{cases} \arctan\left(-\frac{a'_{r_2}}{a'_{r_3}}\right) = \arctan\left(-\frac{a'_{i_2}}{a'_{i_3}}\right) & \phi_s \neq 0^\circ, 90^\circ \\ \arctan\left(-\frac{a'_{i_2}}{a'_{i_3}}\right) & \phi_s = 0^\circ \\ \arctan\left(-\frac{a'_{r_2}}{a'_{r_3}}\right) & \phi_s = 90^\circ \end{cases} \tag{D.6}$$

If $\alpha_s = 45^\circ$ and $\phi_{\alpha_s} = 0^\circ$, the target is either a left oriented or a right oriented helix, depending on the sign of the elicity. The orientation angle is estimated with an error equals

to $\phi_s/2$ and it can be shown that

$$\phi_s \pm 2\psi = \arctan\left(\frac{a'_{r_3}}{a'_{r_2}}\right) = \arctan\left(-\frac{a'_{i_2}}{a'_{i_3}}\right) \tag{D.7}$$

If $\alpha_s = \pm 90°$, like in Dihedral type of targets, the analysis is performed independently of the value of τ_m, even because the latter is undetermined in this configuration.

$$2\psi = \begin{cases} \arctan\left(\frac{a'_{r_3}}{a'_{r_2}}\right) = \arctan\left(\frac{a'_{i_3}}{a'_{i_2}}\right) & \phi_s + \phi_{\alpha_s} \neq 0°, 90° \\ \arctan\left(\frac{a'_{r_3}}{a'_{r_2}}\right) & \phi_s + \phi_{\alpha_s} = 0° \\ \arctan\left(\frac{a'_{i_3}}{a'_{i_2}}\right) & \phi_s + \phi_{\alpha_s} = 90° \end{cases} \tag{D.8}$$

Note from (D.6) and (D.8) that Dihedral and Dihedral 45 type of targets can not be simultaneously identified.

Now let us investigate some special situations when ϕ_s is known, meaning that $\tau_m \neq 45°$ and $\alpha_s \neq 90°$. After removing ϕ_s, we get

$$\begin{aligned} a''_{r_1} &= \cos(\alpha_s)\cos(2\tau_m) \\ a''_{r_2} &= \cos(2\psi)\sin(\alpha_s)\cos(\phi_{\alpha_s}) \\ a''_{r_3} &= \sin(2\psi)\sin(\alpha_s)\cos(\phi_{\alpha_s}) \\ a''_{i_1} &= 0 \\ a''_{i_2} &= \cos(2\psi)\sin(\alpha_s)\sin(\phi_{\alpha_s}) + \sin(2\psi)\cos(\alpha_s)\sin(2\tau_m) \\ a''_{i_3} &= \sin(2\psi)\sin(\alpha_s)\sin(\phi_{\alpha_s}) - \cos(2\psi)\cos(\alpha_s)\sin(2\tau_m) \end{aligned} \tag{D.9}$$

where $a'' = a' \cdot e^{-j\phi_s}$.

If $\alpha_s \neq 0°$ and $\phi_{\alpha_s} \neq 90°$ then

$$\psi = \frac{1}{2}\arctan\left(\frac{a''_{r_3}}{a''_{r_2}}\right) \tag{D.10}$$

Now, let $\phi_{\alpha_s} = 90°$, then (D.9) is given by

$$\begin{aligned} a''_{r_1} &= \cos(\alpha_s)\cos(2\tau_m) \\ a''_{r_2} &= 0 \\ a''_{r_3} &= 0 \\ a''_{i_1} &= 0 \\ a''_{i_2} &= \cos(2\psi)\sin(\alpha_s) + \sin(2\psi)\cos(\alpha_s)\sin(2\tau_m) \\ a''_{i_3} &= \sin(2\psi)\sin(\alpha_s) - \cos(2\psi)\cos(\alpha_s)\sin(2\tau_m) \end{aligned} \tag{D.11}$$

Therefore, ψ, α_s and τ_m can not be determined, meaning that, for instance, Quarter Wave scatters can not be automatically identified.

Now, let $\alpha_s = 0°$, configuration of targets as Trihedrals for instance. The mixing matrix components are given by

$$\begin{aligned} a''_{r_1} &= \cos(2\tau_m) \\ a''_{r_2} &= 0 \\ a''_{r_3} &= 0 \\ a''_{i_1} &= 0 \\ a''_{i_2} &= \sin(2\psi)\sin(2\tau_m) \\ a''_{i_3} &= \cos(2\psi)\sin(2\tau_m) \end{aligned} \tag{D.12}$$

The orientation angle is then estimated as

$$\psi = \frac{1}{2}\arctan\left(-\frac{a''_{i_2}}{a''_{i_3}}\right) \tag{D.13}$$

Nevertheless since it is impossible (unless $\tau_m = 0$) to know in advance from the mixing matrix elements a'' if $\alpha_s = 0°$ or $\phi_{\alpha_s} = 90°$, the algorithm can not precisely estimates ψ, and consequently the others parameters in both cases as well.

Appendix E

Datasets employed throughout the thesis

The conduction of SAR data acquisition campaigns is a task that involves many distinct aspects, both related to the logistics of the acquisition as well as related to the system design. Therefore, it is a process that involves a large number of people from varied fields and generally takes several months between planning and execution. Furthermore, if in situ measurements are also carried out, then the complexity of the mission grows substantially, requiring specialized personnel (geologists, biologists and physicists, among others) to achieve the desired goals.

In the present work, no specific campaign was performed. Instead, we choose to employ in our study datasets already available that matched the scenarios we wanted to investigate. Therefore, all our analysis starts after the image formation process (see Chapter 2) and we assume that all aspects related to the latter are correctly addressed. The drawback of such approach is that in situ measurements (related to ground truth) are not always available or not in the desired format, somehow limiting final conclusions.

Three datasets are primarily used throughout this thesis. We have selected distinct scenarios illuminated by sensors with different characteristics. The areas under investigation are mainly composed by tropical forest, snow and an agricultural site with human constructions and canonical scatters. The following sections briefly describe each dataset employed, along with their acquiring sensors features. It is important to highlight that the information presented below is extracted, as is, from the given campaign reports and, as previously mentioned, are assumed to be true.

E.1 SETHI sensor - French Guiana region

SETHI is a new generation airborne SAR developed by the French Aerospace Research Agency ONERA [9]. SETHI is a full polarimetric, multi-band system which can be operated with four radar front ends simultaneously. In P-band mode, the bandwidth is 200MHz, the range resolution 1.2m and the azimuth resolution 1.5m [32].

The acquisition campaign of the dataset used in this thesis took place in August 2009 in French Guiana under the denomination TropiSAR. The main objective in acquiring a

large amount, good quality tropical forest dataset was to provide enough information that could help answering specific questions to support the Phase A of the 7th Earth Explorer candidate mission, BIOMASS [32]. Multi temporal and multi baseline P-band and L-band full polarimetric images were produced.

In the present work, we focus our analyses in the dataset acquired over the Paracou test site in French Guiana. The SLC images were processed using the ONERA SAR processor [13], based on a modified version of the range-migration algorithm [92]. The postprocessing includes crosstalk removal, radiometric, and polarimetric calibration [32]. Figure E.1 presents the RGB image of the referred area. Since the dataset contemplates a high amount of pixels, throughout this thesis we performed the analyses using sub-regions of the aforementioned data, which are always within the marked rectangles.

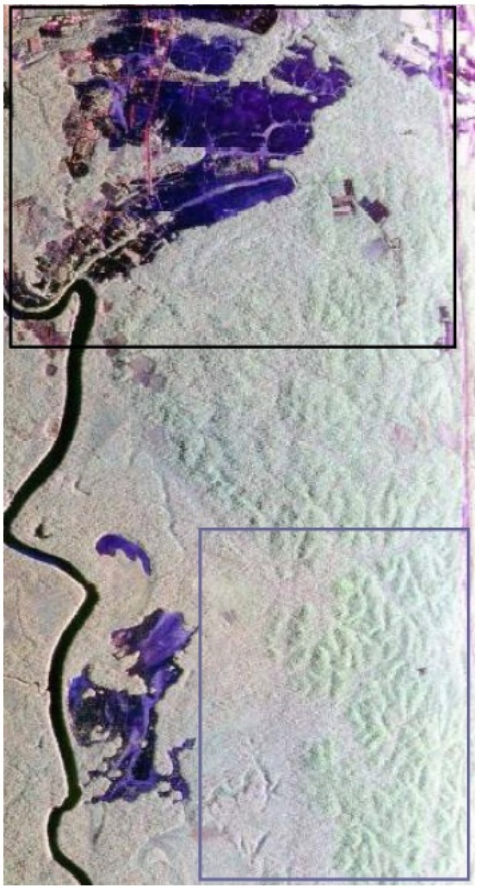

Figure E.1: French Guiana area under study: RGB image, Red (HH), Green (HV), Blue (VV).The north is toward the top of the image and the river on the west side is the Sinnamary river.

E.2 RAMSES sensor - Brétigny region

The RAMSES (Radar Aéroporté Multi-spectrald'Etudes des Signatures) is a full polarimetric, multi-band, very high resolution Synthetic Aperture Radar system developed by the French Aerospace Research Agency (ONERA) [10]. Being a flexible SAR system conceived to serve as an experimental test bench for new technologies, is in constant evolution, like for instance the increase in the range resolution when in X-band configuration. When operating in X-band, the central transmit frequency is 9.5GHz, the bandwidth is 1200MHz and the range resolution 11cm. Furthermore, it can be flown in a polarimetric interferometric mode [31]. The motion compensation is based on an integrated inertial system coupled to a post-processing stage [13], a fast frequency domain synthesis algorithm associated with an auto-focus method [31].

The dataset employed in the present thesis corresponds to a set of polarimetric-interferometric images acquired in a campaign that flew over a Brétigny region composed by industrial buildings, trees, a parking lot, and four canonical trihedrals used for calibration. Figure E.2 presents the RGB image of the referred area.

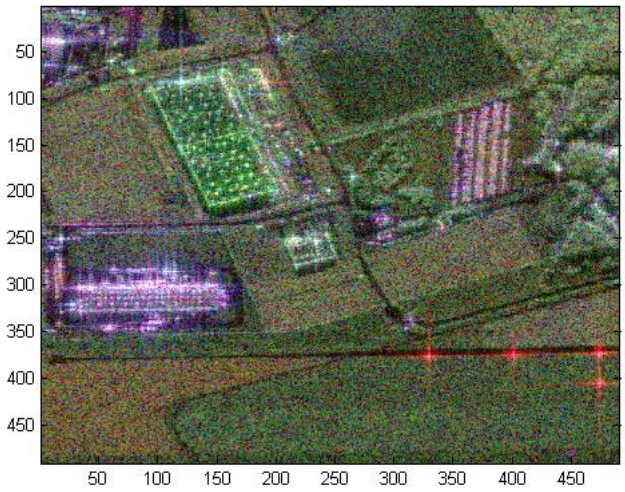

Figure E.2: Brétigny area under study: RGB image, Red (HH+VV), Green (HV), Blue (HH-VV).

E.3 E-SAR sensor - Tacul Glacier region

The DLR's airborne Experimental Synthetic Aperture Radar System, E-SAR, is also a full polarimetric, multi-band system [46]. The first images acquired with this sensor date back to 1988, since then the system experienced several improvements in order to continuously upgraded its performance. When in L-band, the central transmit frequency is 1.3GHz, the bandwidth is either 100MHz or 50MHz and the range resolution, consequently is either 2m

or 4m, respectively. Finally, the azimuth resolution is 0.4m. An Extended Chirp Scaling (ECS) algorithm based processor converts the SAR data to calibrated image data products. Radiometric and polarimetric calibration are also implemented [46].

The acquisition campaign of the dataset used in this thesis took place in October 2006 over two well known glaciers located in the Mont-Blanc area in the Alps: the Argentiere and the Mer de Glace glaciers. The main objective of the given mission was to measure temperate glacier velocities and surface characteristics. The polarimetric data have been acquired by the collaboration between the DLR Microwaves and Radar Institute and the MEGATOR group.

Even though repeat-pass data (for interferometric applications) and multi-band data were available from both sites, in the present work, we are mainly interested in the full polarization L-band images acquired during the flights in direction SE-NW on the upper parts of the Mer de Glace (Tacul and Leschaux glaciers). Specially suited motion compensation algorithms [83] were employed in the focusing stage (image formation) to comply with the large topographic variation in elevation in the given Alpine region (2000 m) [54]. Figure E.3 presents the RGB image of the referred area.

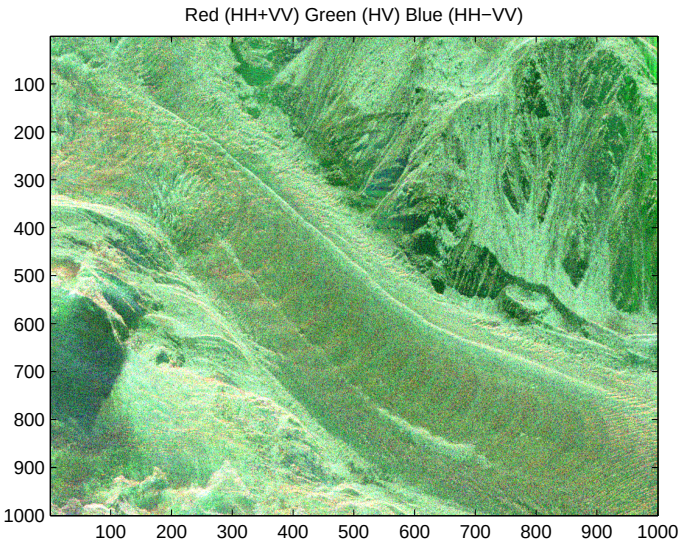

Figure E.3: Tacul glacier area under study: RGB image, Red (HH+VV), Green (HV), Blue (HH-VV).

Bibliography

[1] Ludwig Baringhaus. "Testing for spherical symmetry of a multivariate distribution." In: *The Annals of Statistics* (1991), pp. 899–917 (cit. on p. 29).

[2] J-M Beaulieu and Ridha Touzi. "Segmentation of textured scenes using polarimetric SARs." In: *Geoscience and Remote Sensing Symposium, 2003. IGARSS'03. Proceedings. 2003 IEEE International*. Vol. 1. IEEE. 2003, pp. 446–448 (cit. on p. 28).

[3] Nikola Besic, Gabriel Vasile, Jocelyn Chanussot, and Stevan Stankovic. "Polarimetric incoherent target decomposition by means of independent component analysis." In: *Geoscience and Remote Sensing, IEEE Transactions on* 53.3 (2015), pp. 1236–1247 (cit. on pp. 3, 4, 21, 44, 52–54, 56–58, 63, 70, 81, 90, 133–135, 139, 147).

[4] Rajendra Bhatia and John Holbrook. "Riemannian geometry and matrix geometric means." In: *Linear Algebra and its applications* 413.2 (2006), pp. 594–618 (cit. on p. 75).

[5] Ella Bingham and Aapo Hyvärinen. "A fast fixed-point algorithm for independent component analysis of complex valued signals." In: *International journal of neural systems* 10.01 (2000), pp. 1–8 (cit. on p. 53).

[6] Lionel Bombrun. "Développement d'outils et de méthodes de télédétection spatiale optique et radar nécessaires à la haute résolution spatiale." PhD thesis. Institut National Polytechnique de Grenoble-INPG, 2008 (cit. on p. 47).

[7] Lionel Bombrun, Gabriel Vasile, Michel Gay, and Felix Totir. "Hierarchical segmentation of polarimetric SAR images using heterogeneous clutter models." In: *Geoscience and Remote Sensing, IEEE Transactions on* 49.2 (2011), pp. 726–737 (cit. on pp. 2, 27, 123, 124).

[8] Lionel Bombrun, Gabriel Vasile, Michel Gay, Jean-Philippe Ovarlez, and Frédéric Pascal. "Roll invariant target detection based on POLSAR clutter models." In: *IEEE International Geoscience and Remote Sensing Symposium (IGARSS 2010)*. 2010, p. 4 (cit. on pp. 47, 48).

[9] Gregory Bonin, Pascale Dubois-Fernandez, Philippe Dreuillet Olivier Ruault du Plessis, Sebastien Angelliaume, Hubert Cantalloube, Helene Oriot, and Colette Coulombeix. "The new ONERA multispectral airborne SAR system in 2009." In: *2009 IEEE Radar Conference*. IEEE. 2009, pp. 1–3 (cit. on p. 103).

[10] JM Boutry. *ONERA airborne SAR facilities*. Tech. rep. Environmental Research Institute of Michigan (ERIM), Ann Arbor, MI (United States), 1996 (cit. on p. 105).

[11] William L Cameron and Houra Rais. "Conservative polarimetric scatterers and their role in incorrect extensions of the Cameron decomposition." In: *Geoscience and Remote Sensing, IEEE Transactions on* 44.12 (2006), pp. 3506–3516 (cit. on p. 20).

[12] William L Cameron, Nazih N Youssef, and Ling K Leung. "Simulated polarimetric signatures of primitive geometrical shapes." In: *Geoscience and Remote Sensing, IEEE Transactions on* 34.3 (1996), pp. 793–803 (cit. on p. 20).

[13] H-MJ Cantalloube and P Dubois-Fernandez. "Airborne X-band SAR imaging with 10 cm resolution-technical challenge and preliminary results." In: *Geoscience and Remote Sensing Symposium, 2003. IGARSS'03. Proceedings. 2003 IEEE International*. Vol. 1. IEEE. 2003, pp. 185–187 (cit. on pp. 104, 105).

[14] A.B. Carlson, P. Crilly, and J. Rutledge. "Communication systems: An introduction to signals and noise in electrical communication." In: *Guía Académica* (1986), p. 129 (cit. on p. 11).

[15] Jacques E Cilliers and Johan C Smit. "Pulse compression sidelobe reduction by minimization of L p-norms." In: *IEEE Transactions on Aerospace and Electronic Systems* 43.3 (2007), pp. 1238–1247 (cit. on p. 10).

[16] Shane R Cloude. "Dual-baseline coherence tomography." In: *IEEE Geoscience and Remote Sensing Letters* 4.1 (2007), pp. 127–131 (cit. on p. 21).

[17] Shane R Cloude and Konstantinos P Papathanassiou. "Polarimetric SAR interferometry." In: *IEEE Transactions on Geoscience and Remote Sensing* 36.5 (1998), pp. 1551–1565 (cit. on pp. 84, 86).

[18] Shane Robert Cloude and Eric Pottier. "A review of target decomposition theorems in radar polarimetry." In: *Geoscience and Remote Sensing, IEEE Transactions on* 34.2 (1996), pp. 498–518 (cit. on pp. 2, 21, 28, 40, 45, 46, 56, 131).

[19] Shane Robert Cloude and Eric Pottier. "An entropy based classification scheme for land applications of polarimetric SAR." In: *Geoscience and Remote Sensing, IEEE Transactions on* 35.1 (1997), pp. 68–78 (cit. on pp. 41, 45, 46, 48–50, 55, 71, 85, 90, 132, 134, 141, 142, 148).

[20] SR Cloude. "Polarimetry: the characterization of polarimetric effects in EM scattering." PhD thesis. University of Birmingham, England-UK, 1986 (cit. on p. 20).

[21] Elise Colin, Cécile Titin-Schnaider, and Walid Tabbara. "An interferometric coherence optimization method in radar polarimetry for high-resolution imagery." In: *IEEE Transactions on Geoscience and Remote Sensing* 44.1 (2006), pp. 167–175 (cit. on p. 84).

[22] Elise Colin, Mohamed Tria, Cécile Titin-Schnaider, Jean Philippe Ovarlez, and Messaoud Benidir. "SAR imaging using multidimensional continuous wavelet transform and applications to polarimetry and interferometry." In: *International journal of imaging systems and technology* 14.5 (2004), pp. 206–212 (cit. on p. 84).

[23] Pierre Comon. "Independent component analysis, a new concept?" In: *Signal processing* 36.3 (1994), pp. 287–314 (cit. on p. 52).

[24] Ernesto Conte, Antonio De Maio, and Giuseppe Ricci. "Recursive estimation of the covariance matrix of a compound-Gaussian process and its application to adaptive CFAR detection." In: *Signal Processing, IEEE Transactions on* 50.8 (2002), pp. 1908–1915 (cit. on pp. 63, 138).

[25] Ernesto Conte and Maurizio Longo. "Characterisation of radar clutter as a spherically invariant random process." In: *Communications, Radar and Signal Processing, IEEE Proceedings* 134.2 (1987), pp. 191–197 (cit. on p. 27).

[26] Ernesto Conte, Marco Lops, and Giuseppe Ricci. "Asymptotically optimum radar detection in compound-Gaussian clutter." In: *Aerospace and Electronic Systems, IEEE Transactions on* 31.2 (1995), pp. 617–625 (cit. on p. 27).

[27] DG Corr and AF Rodrigues. "Alternative basis matrices for polarimetric decomposition." In: *Proc. of EUSAR 2002, Cologne, Germany* (2002) (cit. on pp. 46, 47).

[28] J-P Dedieu, Nikola Besic, Gabriel Vasile, J Mathieu, Yves Durand, and Frederic Gottardi. "Dry snow analysis in alpine regions using RADARSAT-2 full polarimetry data: Comparison with in situ measurements." In: *Geoscience and Remote Sensing Symposium (IGARSS), 2014 IEEE International*. IEEE. 2014, pp. 3658–3661 (cit. on pp. 80, 81, 146).

[29] R.H. Dicke. *Object detection system*. US Patent 2,624,876. 1953 (cit. on p. 11).

[30] Anthony P Doulgeris and Torbjorn Eltoft. "Can higher-order statistics add information in model-based polarimetric decompositions?" In: *Proc. POLinSAR*. 2015, p. 6 (cit. on pp. 21, 87).

[31] Pascale Dubois-Fernandez, O Ruault du Plessis, D Le Coz, J Dupas, B Vaizan, X Dupuis, H Cantalloube, C Coulombeix, C Titin-Schnaider, P Dreuillet, et al. "The onera ramses sar system." In: *Geoscience and Remote Sensing Symposium, 2002. IGARSS'02. 2002 IEEE International*. Vol. 3. IEEE. 2002, pp. 1723–1725 (cit. on p. 105).

[32] Pascale C Dubois-Fernandez, Thuy Le Toan, Sandrine Daniel, Hélène Oriot, Jerôme Chave, Lilian Blanc, Ludovic Villard, Malcolm WJ Davidson, and Michel Petit. "The TropiSAR airborne campaign in French Guiana: Objectives, description, and observed temporal behavior of the backscatter signal." In: *IEEE Transactions on Geoscience and Remote Sensing* 50.8 (2012), pp. 3228–3241 (cit. on pp. 38, 103, 104).

[33] Walter G Egan. *Optical remote sensing: science and technology*. Vol. 84. CRC Press, 2003 (cit. on pp. 1, 121).

[34] Charles Elachi and Jakob J Van Zyl. *Introduction to the physics and techniques of remote sensing*. Vol. 28. John Wiley & Sons, 2006 (cit. on pp. 1, 121).

[35] Torbjørn Eltoft, Stian Normann Anfinsen, and Anthony P Doulgeris. "A multitexture model for multilook polarimetric synthetic aperture radar data." In: *Geoscience and Remote Sensing, IEEE Transactions on* 52.5 (2014), pp. 2910–2919 (cit. on pp. 2, 3, 28, 43, 44, 55, 81, 87, 90, 124, 133, 147).

[36] Torbjorn Eltoft, Anthony P Doulgeris, and Jakob Grahn. "Model-based polarimetric decomposition of Arctic sea ice." In: *EUSAR 2014 - 10th European Conference on Synthetic Aperture Radar, Berlin, Germany*. 2014 (cit. on p. 87).

[37] Jan Eriksson and Visa Koivunen. "Complex random vectors and ICA models: Identifiability, uniqueness, and separability." In: *Information Theory, IEEE Transactions on* 52.3 (2006), pp. 1017–1029 (cit. on pp. 3, 57).

[38] Kai-Tai Fang and Jia-Juan Liang. "Tests of spherical and elliptical symmetry." In: *Encyclopedia of statistical sciences* (1999) (cit. on p. 29).

[39] A Ferrari and G Alengrin. "Estimation of the frequencies of a complex sinusoidal noisy signal using fourth order statistics." In: *Acoustics, Speech, and Signal Processing, 1991. ICASSP-91., 1991 International Conference on*. IEEE. 1991, pp. 3457–3460 (cit. on pp. 30, 125).

[40] Roger Fjørtoft and Armand Lopès. "Estimation of the mean radar reflectivity from a finite number of correlated samples." In: *IEEE transactions on geoscience and remote sensing* 39.1 (2001), pp. 196–199 (cit. on p. 27).

[41] Pierre Formont, Frédéric Pascal, Gabriel Vasile, Jean-Philippe Ovarlez, and Laurent Ferro-Famil. "Statistical classification for heterogeneous polarimetric sar images." In: *Selected Topics in Signal Processing, IEEE Journal of* 5.3 (2011), pp. 567–576 (cit. on pp. 2, 27, 39, 123, 131).

[42] Pierre Formont, Frédéric Pascal, Gabriel Vasile, Jean-Philippe Ovarlez, and Laurent Ferro-Famil. "Statistical classification for heterogeneous polarimetric sar images." In: *Selected Topics in Signal Processing, IEEE Journal of* 5.3 (2011), pp. 567–576 (cit. on pp. 61, 69, 74, 138, 139, 143).

[43] Corina C Freitas, Alejandro C Frery, and Antonio H Correia. "The polarimetric G distribution for SAR data analysis." In: *Environmetrics* 16.1 (2005), pp. 13–31 (cit. on pp. 2, 27, 124).

[44] Alejandro Céesar Frery, Häns-Jürgen Müller, Corina da Costa Freitas Yanasse, and Sidnei João Siqueira Sant' Anna. "A model for extremely heterogeneous clutter." In: *Geoscience and Remote Sensing, IEEE Transactions on* 35.3 (1997), pp. 648–659 (cit. on pp. 2, 27, 124).

[45] S.S. Haykin and M. Moher. *Modern wireless communication*. Prentice Hall, 2004 (cit. on p. 9).

[46] Ralf Horn. "The dlr airborne sar project e-sar." In: *Geoscience and Remote Sensing Symposium, 1996. IGARSS'96.'Remote Sensing for a Sustainable Future.', International*. Vol. 3. IEEE. 1996, pp. 1624–1628 (cit. on pp. 105, 106).

[47] Aapo Hyvärinen. "Fast and robust fixed-point algorithms for independent component analysis." In: *Neural Networks, IEEE Transactions on* 10.3 (1999), pp. 626–634 (cit. on pp. 53, 56).

[48] Aapo Hyvärinen, Juha Karhunen, and Erkki Oja. *Independent component analysis*. Vol. 46. John Wiley & Sons, 2004 (cit. on pp. 3, 44, 52, 57, 90, 134, 148).

[49] Hajnsek Irena. "Inversion of surface parameters using Polarimetric SAR." PhD thesis. Ph. D. thesis, 2001, Germany, 2001 (cit. on pp. 20, 46, 48, 49).

[50] Hermann Karcher. "Riemannian center of mass and mollifier smoothing." In: *Communications on pure and applied mathematics* 30.5 (1977), pp. 509–541 (cit. on p. 75).

[51] Gerhard Krieger and Alberto Moreira. "Spaceborne bi-and multistatic SAR: potential and challenges." In: *IEE Proceedings-Radar, Sonar and Navigation* 153.3 (2006), pp. 184–198 (cit. on p. 21).

[52] E Krogager. "New decomposition of the radar target scattering matrix." In: *Electronics Letters* 26.18 (1990), pp. 1525–1527 (cit. on p. 20).

[53] Ernst Krogager. "Aspects of polarimetric radar imaging." PhD thesis. Danish Defence Research Establishment, 1993 (cit. on p. 47).

[54] Tania Landes, Michel Gay, Emmanuel Trouvé, J-M Nicolas, Lionel Bombrun, Gabriel Vasile, and Irena Hajnsek. "Monitoring temperate glaciers by high resolution Pol-InSAR data: First analysis of Argentière E-SAR acquisitions and in-situ measurements." In: *2007 IEEE International Geoscience and Remote Sensing Symposium*. IEEE. 2007, pp. 184–187 (cit. on pp. 78–80, 106, 144, 145).

[55] Tom Rune Lauknes, Yngvar Larsen, Harald Johnsen, and Torbjorn Eltoft. "Characterization of coherent scatterers in natural terrain using SAR polarimetry." In: *ESA Special Publication*. Vol. 644. 2007 (cit. on p. 51).

[56] Jong-Sen Lee, Mitchell R Grunes, and Gianfranco De Grandi. "Polarimetric SAR speckle filtering and its implication for classification." In: *IEEE Transactions on Geoscience and remote sensing* 37.5 (1999), pp. 2363–2373 (cit. on p. 25).

[57] Jong-Sen Lee and Eric Pottier. *Polarimetric radar imaging: from basics to applications*. CRC press, 2009 (cit. on pp. 8, 10, 14, 16, 23, 122).

[58] Jong-Sen Lee, Thomas L Ainsworth, John P Kelly, and Carlos Lopez-Martinez. "Evaluation and bias removal of multilook effect on entropy/alpha/anisotropy in polarimetric SAR decomposition." In: *Geoscience and Remote Sensing, IEEE Transactions on* 46.10 (2008), pp. 3039–3052 (cit. on pp. 38, 56, 59, 73, 131, 136, 137).

[59] Jong-Sen Lee, Karl W Hoppel, Stephen A Mango, and Allen R Miller. "Intensity and phase statistics of multilook polarimetric and interferometric SAR imagery." In: *IEEE Transactions on Geoscience and Remote Sensing* 32.5 (1994), pp. 1017–1028 (cit. on p. 26).

[60] Jong-Sen Lee, Karl W Hoppel, Stephen A Mango, and Allen R Miller. "Intensity and phase statistics of multilook polarimetric and interferometric SAR imagery." In: *Geoscience and Remote Sensing, IEEE Transactions on* 32.5 (1994), pp. 1017–1028 (cit. on p. 57).

[61] Jong-Sen Lee, L Jurkevich, P Dewaele, Pl Wambacq, and A Oosterlinck. "Speckle filtering of synthetic aperture radar images: A review." In: *Remote Sensing Reviews* 8.4 (1994), pp. 313–340 (cit. on p. 25).

[62] Jong-Sen Lee, Mitchell R Grunes, Thomas L Ainsworth, Li-Jen Du, Dale L Schuler, and Shane R Cloude. "Unsupervised classification using polarimetric decomposition and the complex Wishart classifier." In: *Geoscience and Remote Sensing, IEEE Transactions on* 37.5 (1999), pp. 2249–2258 (cit. on p. 52).

[63] Nicolas Longepe, Sophie Allain, Laurent Ferro-Famil, Eric Pottier, and Yves Durand. "Snowpack characterization in mountainous regions using C-band SAR data and a meteorological model." In: *Geoscience and Remote Sensing, IEEE Transactions on* 47.2 (2009), pp. 406–418 (cit. on pp. 80, 146).

[64] Armand Lopes, E Nezry, R Touzi, and H Laur. "Structure detection and statistical adaptive speckle filtering in SAR images." In: *International Journal of Remote Sensing* 14.9 (1993), pp. 1735–1758.

[65] Carlos Lopez-Martinez, Eric Pottier, and Shane R Cloude. "Statistical assessment of eigenvector-based target decomposition theorems in radar polarimetry." In: *Geoscience and Remote Sensing, IEEE Transactions on* 43.9 (2005), pp. 2058–2074 (cit. on pp. 26, 38, 57, 59, 73, 131, 137).

[66] Jan R Magnus and Heinz Neudecker. "The commutation matrix: some properties and applications." In: *The Annals of Statistics* (1979), pp. 381–394 (cit. on pp. 29, 93, 94, 96, 125).

[67] Mélanie Mahot, Frédéric Pascal, Philippe Forster, and J Ovarlez. "Asymptotic properties of robust complex covariance matrix estimates." In: *Signal Processing, IEEE Transactions on* 61.13 (2013), pp. 3348–3356 (cit. on pp. 29, 125).

[68] Audrey Martini, Laurent Ferro-Famil, Eric Pottier, and J Dedieu. "Dry snow discrimination in alpine areas from multi-frequency and multi-temporal SAR data." In: *Radar Sonar and Navigation, IEEE Poceedings* 153.3 (2006), p. 271 (cit. on pp. 80, 146).

[69] Hamish Meikle. *Modern radar systems*. Artech House, 2008 (cit. on p. 12).

[70] Maher Moakher. "A differential geometric approach to the geometric mean of symmetric positive-definite matrices." In: *SIAM Journal on Matrix Analysis and Applications* 26.3 (2005), pp. 735–747 (cit. on p. 75).

[71] JJ Mohr. *SAR Light an introduction to Synthetic Aperture Radar*. NB 238. 2005 (cit. on p. 14).

[72] Matteo Nannini, Rolf Scheiber, and Alberto Moreira. "Estimation of the minimum number of tracks for SAR tomography." In: *IEEE Transactions on Geoscience and Remote Sensing* 47.2 (2009), pp. 531–543 (cit. on p. 21).

[73] Abraao DC Nascimento, Renato J Cintra, and Alejandro C Frery. "Hypothesis testing in speckled data with stochastic distances." In: *Geoscience and Remote Sensing, IEEE Transactions on* 48.1 (2010), pp. 373–385 (cit. on pp. 2, 27, 124).

[74] Leslie M Novak and Michael C Burl. "Optimal speckle reduction in polarimetric SAR imagery." In: *Aerospace and Electronic Systems, IEEE Transactions on* 26.2 (1990), pp. 293–305 (cit. on pp. 2, 27, 124).

[75] Mike Novey and Tülay Adali. "On extending the complex FastICA algorithm to noncircular sources." In: *Signal Processing, IEEE Transactions on* 56.5 (2008), pp. 2148–2154 (cit. on p. 53).

[76] Esa Ollila, David E Tyler, Visa Koivunen, and H Vincent Poor. "Complex elliptically symmetric distributions: Survey, new results and applications." In: *Signal Processing, IEEE Transactions on* 60.11 (2012), pp. 5597–5625 (cit. on pp. 2, 26–30, 124, 125).

[77] Konstantinos P Papathanassiou and Shane R Cloude. "Single-baseline polarimetric SAR interferometry." In: *IEEE Transactions on Geoscience and Remote Sensing* 39.11 (2001), pp. 2352–2363 (cit. on p. 86).

[78] B Picinbono. "Spherically invariant and compound Gaussian stochastic processes (Corresp.)" In: *Information Theory, IEEE Transactions on* 16.1 (1970), pp. 77–79 (cit. on p. 27).

[79] Leandro Pralon, Bruno Pompeo, and Jose Mauro Fortes. "Stochastic analysis of random frequency modulated waveforms for noise radar systems." In: *IEEE Transactions on Aerospace and Electronic Systems* 51.2 (2015), pp. 1447–1461 (cit. on p. 11).

[80] Leandro Pralon, Gabriel Vasile, Mauro Dalla Mura, Jocelyn Chanussot, and Nikola Besic. "Evaluation of ICA based ICTD for PolSAR data analysis in tropical forest scenario." In: *Geoscience and Remote Sensing Symposium (IGARSS), 2015 IEEE International*. IEEE. 2015, pp. 3786–3789 (cit. on pp. 51, 70).

[81] Leandro Pralon, Gabriel Vasile, Mauro Dalla Mura, Jocelyn Chanussot, and Nikola Besic. "Evaluation of ICA-Based ICTD for PolSAR Data Analysis Using a Sliding Window Approach: Convergence Rate, Gaussian Sources, and Spatial Correlation." In: *IEEE Transactions on Geoscience and Remote Sensing* 54.7 (2016), pp. 4262–4271 (cit. on p. 73).

[82] Leandro Pralon, Nikola Besic, Gabriel Vasile, Mauro Dalla Mura, and Jocelyn Chanussot. "Evaluation of Multilook Effect in ICA Based ICTD for PolSAR Data Analysis." In: *International Workshop on Science and Applications of SAR Polarimetry and Polarimetric Interferometry*. 2015 (cit. on pp. 38, 131).

[83] Pau Prats, Karlus A Câmara de Macedo, Andreas Reigber, Rolf Scheiber, and Jordi J Mallorqui. "Comparison of topography-and aperture-dependent motion compensation algorithms for airborne SAR." In: *IEEE Geoscience and Remote Sensing Letters* 4.3 (2007), pp. 349–353 (cit. on p. 106).

[84] Muralidhar Rangaswamy. "Spherically invariant random processes for modeling non-Gaussian radar clutter." In: *Signals, Systems and Computers, 1993. 1993 Conference Record of The Twenty-Seventh Asilomar Conference on*. IEEE. 1993, pp. 1106–1110 (cit. on p. 27).

[85] Muralidhar Rangaswamy, Donald Weiner, and Aydin Öztürk. "Computer generation of correlated non-Gaussian radar clutter." In: *Aerospace and Electronic Systems, IEEE Transactions on* 31.1 (1995), pp. 106–116 (cit. on pp. 2, 27, 124).

[86] Andreas Reigber and Alberto Moreira. "First demonstration of airborne SAR tomography using multibaseline L-band data." In: *IEEE Transactions on Geoscience and Remote Sensing* 38.5 (2000), pp. 2142–2152 (cit. on p. 21).

[87] John Alan Richards et al. *Remote sensing with imaging radar*. Vol. 1. Springer, 2009 (cit. on pp. 1, 7, 14, 16, 20, 22, 23, 121).

[88] A Rodrigues, D Corr, K Partington, E Pottier, and L Ferro-Famil. "Unsupervised wishart classifications of sea-ice using entropy, Alpha and Anisotropy Decompositions." In: *Applications of SAR Polarimetry and Polarimetric Interferometry*. Vol. 529. 2003, p. 17 (cit. on p. 87).

[89] Bernd Scheuchl, Ian Cumming, and Irena Hajnsek. "Classification of fully polarimetric single-and dual-frequency SAR data of sea ice using the Wishart statistics." In: *Canadian Journal of Remote Sensing* 31.1 (2005), pp. 61–72 (cit. on p. 87).

[90] James R Schott. "Testing for elliptical symmetry in covariance-matrix-based analyses." In: *Statistics & probability letters* 60.4 (2002), pp. 395–404 (cit. on pp. 29, 31, 32, 95, 97, 125, 127, 128).

[91] M.I. Skolnik. "Introduction to Radar." In: *Radar Handbook* (1962), p. 1990 (cit. on pp. 9–11).

[92] Mehrdad Soumekh. *Synthetic aperture radar signal processing*. New York: Wiley, 1999 (cit. on p. 104).

[93] Stefano Tebaldini. "Polarimetric SAR Tomography of forest scenarios." In: () (cit. on p. 86).

[94] Stefano Tebaldini. "Single and multipolarimetric SAR tomography of forested areas: A parametric approach." In: *IEEE Transactions on Geoscience and Remote Sensing* 48.5 (2010), pp. 2375–2387 (cit. on p. 21).

[95] RJA Tough, D Blacknell, and S Quegan. "A statistical description of polarimetric and interferometric synthetic aperture radar data." In: *Proceedings of the Royal Society of London A: Mathematical, Physical and Engineering Sciences*. Vol. 449. 1937. The Royal Society. 1995, pp. 567–589 (cit. on p. 26).

[96] RJA Tough, D Blacknell, and S Quegan. "A statistical description of polarimetric and interferometric synthetic aperture radar data." In: *Proceedings of the Royal Society of London A: Mathematical, Physical and Engineering Sciences*. Vol. 449. 1937. The Royal Society. 1995, pp. 567–589 (cit. on p. 57).

[97] R Touzi, WM Boerner, JS Lee, and E Lueneburg. "A review of polarimetry in the context of synthetic aperture radar: concepts and information extraction." In: *Canadian Journal of Remote Sensing* 30.3 (2004), pp. 380–407 (cit. on pp. 2, 28, 55, 81, 124).

[98] Ridha Touzi. "Target scattering decomposition in terms of roll-invariant target parameters." In: *Geoscience and Remote Sensing, IEEE Transactions on* 45.1 (2007), pp. 73–84 (cit. on pp. 2, 20, 21, 33, 45–47, 55, 59, 81, 129, 134).

[99] Ridha Touzi, Armand Lopes, and Pierre Bousquet. "A statistical and geometrical edge detector for SAR images." In: *IEEE Transactions on geoscience and remote sensing* 26.6 (1988), pp. 764–773 (cit. on p. 84).

[100] John Tyndall. *The Glaciers of the Alps: Being a Narrative of Excursions and Ascents, an Account of the Origin and Phenomena of Glaciers and an Exposition of the Physical Principles to which They are Related*. Cambridge University Press, 2011 (cit. on pp. 78, 144).

[101] Fawwaz T Ulaby, W Herschel Stiles, and Mohamed AbdelRazik. "Snowcover influence on backscattering from terrain." In: *Geoscience and Remote Sensing, IEEE Transactions on* 2 (1984), pp. 126–133 (cit. on pp. 80, 146).

[102] Fawwaz T Ulaby, F Kouyate, B Brisco, and TH Lee Williams. "Textural infornation in SAR images." In: *Geoscience and Remote Sensing, IEEE Transactions on* 2 (1986), pp. 235–245 (cit. on pp. 2, 27, 124).

[103] Roberto Vaccaro, Paul C Smits, and Silvana G Dellepiane. "Exploiting spatial correlation features for SAR image analysis." In: *Geoscience and Remote Sensing, IEEE Transactions on* 38.3 (2000), pp. 1212–1223 (cit. on p. 64).

[104] Gabriel Vasile, Jean-Philippe Ovarlez, Frederic Pascal, and Céline Tison. "Coherency matrix estimation of heterogeneous clutter in high-resolution polarimetric SAR images." In: *Geoscience and Remote Sensing, IEEE Transactions on* 48.4 (2010), pp. 1809–1826 (cit. on pp. 2–4, 27, 28, 52, 56, 70, 123, 135).

[105] Gabriel Vasile, Frédéric Pascal, Jean-Philippe Ovarlez, Pierre Formont, and Michel Gay. "Optimal parameter estimation in heterogeneous clutter for high-resolution polarimetric SAR data." In: *Geoscience and Remote Sensing Letters, IEEE* 8.6 (2011), pp. 1046–1050 (cit. on pp. 2, 27, 123).

[106] Hiroyoshi Yamada, Rynosuke Takizawa, Yoshio Yamaguchi, and Ryoichi Sato. "Polsar/pol-insar data analysis by using ica." In: *Synthetic Aperture Radar (EUSAR), 2010 8th European Conference on*. VDE. 2010, pp. 1–4 (cit. on p. 54).

[107] Kung Yao. "A representation theorem and its applications to spherically-invariant random processes." In: *Information Theory, IEEE Transactions on* 19.5 (1973), pp. 600–608 (cit. on pp. 2, 27, 123).

Publications

Journal papers:

1. Pralon L., Vasile G., Dalla Mura M., Chanussot J., Besic N., *"Evaluation of ICA Based ICTD for PolSAR Data Analysis Using a Sliding Window Approach: Convergence Rate, Gaussian Sources and Spatial Correlation"*, IEEE Transactions on Geoscience and Remote Sensing, Vol. 54, No. 7, 2016, pp. 4262-4271, doi 10.1109/TGRS.2016.2538900

2. Pralon L., Vasile G., Dalla Mura M., Anghel A., Chanussot J., *"Spherical Symmetry of Complex Stochastic Models in Multivariate High-Resolution PolSAR Images"*, IEEE Transactions on Geoscience and Remote Sensing, Vol. 54, No. 7, 2016, pp. 4250-4261, doi 10.1109/TGRS.2016.2538820

Journal papers outside of the scope of the thesis:

3. L. Pralon, B. Pompeo, J.M. Fortes, *"Stochastic Analysis of Random Frequency Modulated Waveforms for Noise Radar Systems"*, IEEE Transactions on Aerospace and Electronic Systems, Vol. 51, No. 2, 2015, pp. 1447 - 1461, doi 10.1109/TAES.2014.140072.

Journal papers undergoing review:

4. Pralon L., Vasile G., Dalla Mura M., Chanussot J., *"Evaluation of the new information in the H/α feature space provided by ICA in PolSAR data analysis"*, IEEE Transactions on Geoscience and Remote Sensing, submitted March 2016.

Conference papers:

5. Vasile G., Pralon L., *"Blind Source Separation in Polarimetric SAR Interferometry"*, IEEE International Geoscience and Remote Sensing Symposium, special session on Advanced Methods for Polarimetric SAR Information Extraction, Beijing, China, pp. 1-4, 2016

6. Pralon L., Pralon M.G., Pompeo B., Vasile G., *"On a Probabilistic Approach to Detect Noise Radar Random Transmit Waveforms Based on a Simple Circularity Test"*, IEEE Radar Conference, Philadelphia, PA, USA, pp. 1-4, 2016

7. Pralon L., Vasile G., Anghel A., Besic N., *"On the Robustness of the ICA Based ICTD with respect to the Spherical Symmetry of the POLSAR Data"*, IEEE International Geoscience and Remote Sensing Symposium, special session on SAR Polarimetry: Theory and Applications, Milan, Italy, pp. 1570-1573, 2015

8. Pralon L., Vasile G., Dalla Mura M., Chanussot J., Besic N., *"Evaluation of ICA Based ICTD for POLSAR Data Analysis in Tropical Forest Scenario"*, IEEE International Geoscience and Remote Sensing Symposium, Milan, Italy, pp. 3786-3789, 2015

9. Pralon L., Besic N., Vasile G., Dalla Mura M., Chanussot J., *"Evaluation of Multilook Effect in ICA Based ICDT for POLSAR Data Analysis"*, International Workshop on Science and Applications of SAR Polarimetry and Polarimetric Interferometry, European Space Agency, special publication SP-729, Franscati, Italy, 6 pages, January 2015

Abstract

Abstract — Polarimetric SAR (PolSAR) systems characterize a sensed area based on the analysis of the interaction between the latter and the transmitted waveform, considering different polarimetric states. One of the most employed techniques for PolSAR image interpretation is the Polarimetric Target Decomposition (TD), that enables the description of an image cell as a sum of canonical scattering mechanisms, making it more intuitive to understand the behaviour of the clutter and therefore to analyse it. There are key aspects that underpin effective PolSAR TD techniques. Stochastic clutter modelling, in case of distributed targets (e.g. vegetation, forests and snow) and the correct retrieval of quantitative information from the estimated scattering mechanisms (parametrization) are examples of such topics that directly influence the performance of applied algorithms. Within this context, this thesis comprises two research axes. First, a new methodological framework to assess the conformity of multivariate high-resolution SAR data with respect to the product model (Spherically Invariant Random Vector model) in terms of asymptotic statistics is proposed. More precisely, spherical symmetry is investigated by applying statistical hypotheses testing on the structure of the quadricovariance matrix. Both simulated and real data are taken into consideration to investigate the performance of the derived test by a detailed qualitative and quantitative analysis. The most important conclusion drawn, regarding the methodology employed in analysing SAR data, is that, depending on the scenario under study, a considerable portion of high heterogeneous data may not fit the aforementioned model. Therefore, traditional detection and classification algorithms developed based on the latter become sub-optimal when applied in such kind of regions. This assertion highlights for the need of the development of model independent algorithms, like the Independent Component Analysis, what leads to the second part of the thesis. A Monte Carlo approach is performed in order to investigate the bias in estimating the Touzi's Target Scattering Vector Model (TSVM) parameters when ICA is employed using a sliding window approach under different scenarios. Finally, the performance of the algorithm is also evaluated under Gaussian clutter assumption and when spatial correlation is introduced in the model. These theoretical assessment of ICA based ICTD enables a more efficient analysis of the potential new information provided by the ICA based ICTD. Both Touzi TSVM as well as Cloude and Pottier H/α feature space are then taken into consideration for that purpose. The combined use of ICA and Touzi TSVM is straightforward, indicating new, but not groundbreaking information, when compared to the Eigenvector approach. Nevertheless, the analysis of the combined use of ICA and Cloude and Pottier H/α feature space revealed a potential aspect of the Independent Component Analysis based ICTD, which can not be matched by the Eigenvector approach. ICA does not introduce any unfeasible region in the H/α plane, increasing the range of possible natural phenomenons depicted in the aforementioned feature space.

Keywords: Synthetic Aperture Radar, Multiplicative model, Spherical symmetry test, Polarimetric Incoherent Target Decomposition, Independent Component Analysis.

Résumé — Cette thèse comprend deux axes de recherche. D'abord, un nouveau cadre méthodologique pour évaluer la conformité des données RSO (Radar à Synthèse d'Ouverture) multivariées à haute résolution spatiale est proposé en termes de statistique asymptotique par rapport au modèle produit. Plus précisément, la symétrie sphérique est étudiée en appliquant un test d'hypothèses sur la structure de la matrice de quadri-covariance. Deux jeux de données, simulées et réelles, sont prises en considération pour étudier la performance du test obtenu par l'analyse qualitative et quantitative des résultats. La conclusion la plus importante, en ce qui concerne la méthodologie employée dans l'analyse des données RSO multivariées, est que, selon les différents cas d'usages, une partie considérable de données hétérogènes peut ne pas s'ajuster asymptotiquement au modèle produit. Par conséquent, les algorithmes de classification et/ou détection conventionnels développés sur la base de celui-ci deviennent sub-optimaux. Cette observation met en évidence la nécessité de développer de modèles plus sophistiqués comme l'Analyse en Composantes Indépendantes, ce qui conduit à la deuxième partie de cette thèse qui consiste en l'étude du biais d'estimation des paramètres TSVM (Target Scattering Vector Model) lorsque l'ACP est utilisée. Enfin, les performances de l'algorithme sont également évaluées sous l'hypothèse du bruit gaussien corrélé spatialement. L'évaluation théorique de l'ACI comme un outil de type ICTD (InCoherent Target Decomposition) polarimétrique permet une analyse plus efficace de l'apport d'information fourni. A ce but, deux espaces de représentation sont utilisé, notamment H /alpha et TSVM.

Mots clés : Polarimétriques radar à ouverture synthétique, Modèle Multiplicatif (SIRV), Test de Symétrie Sphérique, Polarimétriques Incoherent cible de Décomposition, Analyse en Composantes Indépendantes, Évaluation Bias, H/α Fonctionnalité espace.

GIPSA-lab, laboratoire de recherche Grenoble, Images, Parole, Signal, Automatique, 11 Rue des Mathématiques
38400 Saint-Martin-d'Hères, France

Résumé étendu

Sommaire

Les systèmes de télédétection fournissent un moyen unique de faire à grande échelle et de manière non-intrusive des observations de la surface de la Terre [87, 34, 33]. Parmi de nombreuses applications, il est possible de mettre en évidence l'analyse de peuplement urbain, le suivi de l'environnement et des cultures, l'évaluation des dommages, estimation de la biomasse et les applications générales de surveillance liées.

Radars d'ouverture synthétique sont souvent employés à cette fin. Les capteurs SAR sont des systèmes actifs qui caractérisent la surface en détectant la rétrodiffusion d'impulsions électromagnétiques envoyées par la plate-forme vers l'ancien [34]. Plusieurs caractéristiques des cibles/scènes éclairées peuvent être dérivées en fonction du choix approprié des paramètres du système et de l'interprétation correcte du signal retourné. Cette affirmation est en quelque sorte intuitive, puisque chaque objet sur la surface de la Terre diffuse une onde électromagnétique incidente d'une manière unique, généralement en fonction de sa forme et de sa composition.

E.4 Principes de base du SAR

Généralement, en télédétection la zone analysée est extensif, ce qui empêche l'utilisation de configurations d'antennes fixes pour ce type d'applications. Par conséquent, côté en regardant

antennes sont intégrées sur une plate-forme mobile (avion, satellite, UAV), produisant des images 2D à grande échelle de zones sur le terrain avec une résolution spatiale considérablement élevée, comme illustré sur la Figure E.4. Cette architecture est référencée dans la littérature sur le radar à ouverture synthétique (SAR).

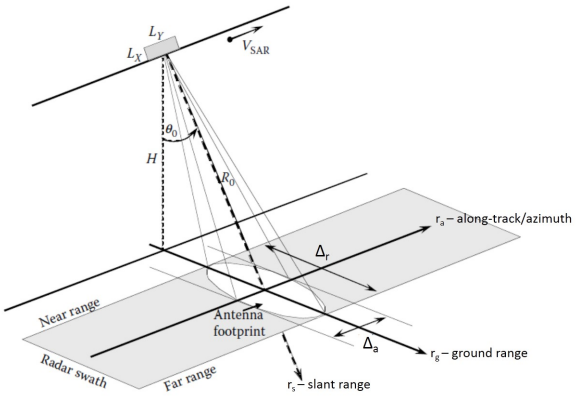

Figure E.4: Géométrie strip map de le radar à ouverture synthétique (modifiée de [57]).

Tandis que la plate-forme se déplace, toute la región indiqué comme zone de radar est détecté. Le processus de formation d'image commence en associant à chaque point sur la surface éclairée une information spécifique. Les informations pertinentes qui peuvent être extraites du signal reçu sont sa puissance moyenne et sa phase. La résolution spatiale joue un rôle clé dans la performance des radars d'ouverture synthétique. Le principe de base sous-jacent à la télédétection par micro-ondes est que toutes les dispersions dans une cellule de résolution contribuent au signal retourné. Quand la cellule de résolution ne considère pas une forte dispersion élémentaire, la distribution est dite distribuée et sa caractérisation doit être effectuée sur la base du comportement moyen de divers mécanismes de diffusion présents dans la composition. Cette analyse est pas simple, comprenant l'emploi des outils probabilistes obtenue sur la base des statistiques asymptotiques et des modèles stochastiques.

E.5 Radar polarimétrique

Des informations supplémentaires peuvent être extraites lors de l'analyse de la dépendance du signal réfléchissant à l'état de polarisation des signaux d'émission. Le concept de polarisation est lié à l'orientation du champ électrique par rapport à la direction de propagation de l'onde électromagnétique.

Dans ce contexte, afin de mieux interpréter les comportements géophysiques, les Radars à Ouverture Synthétique ont donné naissance à des systèmes Polarimétriques SAR (PulSAR). Les données PolSAR décrivent l'interaction entre les ondes électromagnétiques et les dispersions à l'intérieur d'une cellule de résolution, pour chaque état polarimétrique de l'ancienne. Comparativement à l'analyse univariée des systèmes de polarisation unique, la nature multivariée des données Polarimétriques SAR (PolSAR) permet une meilleure prédiction des

propriétés physiques des cibles illuminées, conduisant à une classification plus efficace, à la détection et à des algorithmes d'inversion de paramètres géophysiques.

En ce qui concerne le système décrit dans la section 2.1, la seule différence est que les formes d'onde sont transmises horizontalement et verticalement polarisées, alternativement, et les signaux sont reçus dans les deux antennes simultanément. Par conséquent, quatre images SLC sont formées, une pour chaque paire transmis / reçu d'états de polarization.

Les quatre composantes du vecteur cible PolSAR multivarié, $\mathbf{k}$, décrivant les caractéristiques polarimétriques d'un seul mécanisme de diffusion cohérent à l'intérieur de chaque cellule de résolution sont les éléments de la matrice de Sinclair: S_{hh}, S_{hv}, S_{vh} et S_{vv}. Pour les configurations monostatiques, où le théorème de réciprocité s'applique (c'est-à-dire, $S_{hv} = S_{vh}$) il ne reste que trois composantes: S_{hh}, S_{hv} et S_{vv}. Dans ce cas, la dimension du vecteur cible $\mathbf{k}$ devient $m = 3$ et elle est écrite en base de Pauli comme suit

$$\mathbf{k} = \frac{1}{\sqrt{2}}[S_{hh} + S_{vv} \quad S_{hh} - S_{vv} \quad 2S_{hv}]^T \tag{E.1}$$

E.6 Evaluation Stochastic de clutter PolSAR

L'étude des clutters composées uniquement par des cibles distribués (par exemple, la végétation, des forêts et de la neige), exige une analyse habituellement basée sur les propriétés stochastiques des données SAR ciblés dans l'extraction d'informations sur leur composition. Comparativement à l'analyse univariée des systèmes de polarisation unique, la nature multivariée des données PolSAR permet de mieux prédire les propriétés physiques des cibles illumines. Néanmoins, la caractérisation de données multivariées basées sur des statistiques asymptotiques est considérablement plus complexe.

Lorsque les systèmes SAR de basse résolution font l'objet d'une étude, le nombre de mécanismes de diffusion dans une cellule de résolution est si grand que le théorème de limite centrale peut être pris en considération. Par conséquent, les signaux reçus peuvent être localement modélisés par un processus stochastique Gaussien circulaire à moyenne nulle multivariée, étant complètement caractérisés par leur matrice de covariance. Avec la résolution améliorée des plates-formes SAR modernes, le nombre de diffusions dans chaque cellule de résolution a diminué considérablement. L'hétérogénéité de la scène élevée peut éventuellement conduire à une modélisation non encombrante gaussienne, nécessitant des modèles stochastiques plus complexes pour l'analyse. Les vecteurs aléatoires invariant sphériquement (SIRV) [107], ont été fréquemment utilisés pour la modélisation de haute résolution des données PolSAR [104, 7, 41, 105].

E.7 Modèle de vecteur aléatoire invariant sphérique (SIRV)

Le SIRV est un modèle multiplicatif qui exprime le signal SAR comme un produit entre la racine carrée d'une grandeur scalaire positive (texture) et la description d'une surface homogène équivalente (speckle) [102]. Il est important de noter que dans la définition du SIRV, la fonction de densité de probabilité de texture n'est pas explicitement spécifiée. En conséquence, les SIRV décrivent une classe entière de processus stochastiques [85], incluant le gaussien (multivarié) modèle (texture déterministe), la distribution de Kummer U (texture de Fisher) [7], la distribution $\mathcal{K}$ multivariée (texture gamma) [74] et la distribuition $\mathcal{G}^0$ distribution (texture Gamma inverse) [73], Les deux derniers étant des cas spéciaux de la famille $\mathcal{G}$ multivariée plus générale, spécialement adaptés aux grappes extrêmement hétérogènes [44, 43]. Chaque vecteur d'observation m-dimensionnel $\mathbf{k}$ est défini comme

$$\mathbf{k} = \sqrt{\boldsymbol{\tau}} \cdot \mathbf{z} \tag{E.2}$$

où $\mathbf{z}$ est un vecteur Gaussien circulaire complexe et indépendant, caractérisant le speckle, Avec moyenne nulle et matrice de covariance de la forme $[T] = \sigma_0 \cdot [M]$, tel que $\mathrm{Tr}\{|M|\} = 1$ et σ_0 est la puissance totale (span). Dans (E.2), $\boldsymbol{\tau}$ représente la texture, une variable aléatoire positive caractérisant les variations spatiales de la rétrodiffusion radar, statistiquement indépendante du speckle.

De nombreux procédés ont été proposés dans la littérature à la fois pour dériver la matrice de covariance tachée $[M]$ ainsi que les caractéristiques de texture sous des hypothèses de modèle stochastique spécifiques. Habituellement, les solutions optimales reposent sur des estimateurs de maximum de vraisemblance, qui dépendent fortement du modèle adopté [76]. À l'exception de la matrice de covariance de l'échantillon qui, outre l'estimateur du maximum de vraisemblance sous l'hypothèse gaussienne, présente une signification géométrique / physique pour son estimation (c'est-à-dire qu'il peut être considéré comme le centre de masse des matrices de covariance estimées pour chaque pixel), d'autres estimateurs perdent leur signification si le modèle supposé ne tient pas, devenant sub-optimal.

En dépit de son utilisation répandue dans la communauté, de nombreux auteurs ont soulevé la question si considérer la polarisation de texture indépendante est le modèle le plus approprié pour toutes sortes d'encombrement [35, 97]. En particulier, dans les scénarios forestiers, où le signal retourné peut probablement contenir des contributions de la surface, double rebond et volume de scatters, chacun étant issu de différentes sources et donc potentiellement de textures différentes, on s'attend à une déviation plus élevée de ce modèle [35], démontrant la criticité des hypothèses faites avec le modèle avant toute opération de traitement d'images SAR (segmentation, classification, filtrage des mouchetures). Dans ce contexte, un cadre général est dérivé pour évaluer quantitativement l'ajustement des modèles stochastiques SIRV par rapport à un ensemble de données SAR multidimensionnel donné.

E.8 Test de Wald sur la distribution complexe symétrique elliptique

La procédure adoptée ici pour dériver le test sur la symétrie elliptique complexe est analogue à ce qui a été fait par Schott avec des vecteurs aléatoires à valeur réelle [90]. Par conséquent, quelques étapes sont délibérément laissé implicite étant leur dérivation directe en raison de leur conformité avec le cas réel. Comme mentionné précédemment, le modèle SIR est une sous-classe spécifique de Distributions Elliptiques Simplifiées Complexes (CES), également appelé Gaussien Composé [76]. Les distributions CES présentent une propriété importante qui affirme que leurs matrices de moments d'ordre supérieur sont des scalaires multiples de leur correspondante Distribution normale complexe (CN) [90]. Par conséquent, un moyen facile de vérifier si un ensemble de données suit une distribution de CES est simplement de vérifier si la structure de son quatrième ordre moment (quadri covariance matrice) conserve cette propriété.

Soit $\mathbf{k}$ le vecteur d'observation un ensemble de données $m \times n$ où $m \leq 4$ est le nombre de canaux de polarisation utilisés par le système et n le nombre d'échantillons acquis à partir d'une région homogène, qui partagent les mêmes propriétés statistiques. De plus, supposons que cet ensemble de données est extrait d'une distribution elliptique de moments finis de second ordre avec vecteur moyen nul et matrice de covariance $[M]$. La distribution asymptotique normale du vecteur aléatoire $n^{1/2}\text{vec}(\widehat{[M]} - [M])$, où $\text{vec}(\cdot)$ est l'opérateur qui transforme une matrice en vecteur de colonne [66] et $\widehat{[M]}$ est la matrice de covariance non biaisée, est nulle avec matrice de covariance Ω et matrice de pseudo-covariance P, respectivement donnée par

$$\begin{aligned} \Omega &= \sigma_1([M]^* \otimes [M]) + \sigma_2 \text{vec}([M])\text{vec}([M])^H \\ P &= \sigma_1([M]^* \otimes [M])K_{mm} + \sigma_2 \text{vec}([M])\text{vec}([M])^T \end{aligned} \tag{E.3}$$

où K_{mm} est une matrice de commutation [66], $\cdot^*$ et $\cdot^H$ sont le complex et les opérateurs de transpositions complex respectivement, $\cdot^T$ représente l'opération de transposition, $\otimes$ est l'opérateur du produit Kroneckeret et σ_1 et σ_2 sont des fonctions de la dimensionnalité m et du générateur de fonctions caractéristiques CES ψ [67].

La matrice de moment de quatrième ordre $[M]_4 = E\left[\mathbf{k}\mathbf{k}^H \otimes \mathbf{k}\mathbf{k}^H\right]$ est donnée par (voir l'appendice A)

$$[M]_4 = (1+\omega)\left[\left(I_{m^2} + K_{mm}\right)\left([M] \otimes [M]\right)\right] \tag{E.4}$$

où I_q est les $q \times q$ identity matrix .

Selon [39], l'échantillon de l'estimateur de covariance quadratique complexe peut être exprimé en termes de produit Kronecker comme

$$\widehat{[M]}_4 = \frac{1}{n}\sum_{i=1}^{n} \mathbf{k}_i\mathbf{k}_i^H \otimes \mathbf{k}_i\mathbf{k}_i^H \tag{E.5}$$

Sa forme normalisée correspondante est donnée par

$$\widehat{[M]}_{4*} = \left(\widehat{[M]}^{-\frac{1}{2}^H} \otimes \widehat{[M]}^{-\frac{1}{2}^H}\right) \widehat{[M]}_4 \left(\widehat{[M]}^{-\frac{1}{2}} \otimes \widehat{[M]}^{-\frac{1}{2}}\right) \tag{E.6}$$

where $\widehat{[M]}^{-\frac{1}{2}} \cdot \widehat{[M]}^{-\frac{1}{2}^H} = \widehat{[M]}^{-1}$.

En supposant que $A = \widehat{[M]} - [M]$ et $C = \widehat{[M]}_4 - [M]_4$, l est indiqué dans l'Appendice B qu'en ce qui concerne l'efficacité de l'essai, concernant l'efficacité du test, nous pouvons supposer ci-après, sans perte de généralité, que $[M] = I_m$, où I_m est la matrice d'identité m x m et que

$$\text{vec}(\widehat{[M]}_{4*}) = (1+\omega)\text{vec}([N]_4) + \text{vec}(C) - (1+\omega)H\text{vec}(A) + O_p(n^{-1/2}) \tag{E.7}$$

où $[N]_4$ est ce $[M]_4$ simplifie à quand $k_i \sim CN_m(0, I_m)$ et H est un opérateur donné par

$$H = [I_{m^2} \otimes (I_{m^2} + K_{mm})] \cdot \{I_m \otimes [(K_{mm} \otimes I_m) \cdot (I_m \otimes \text{vec}(I_m))] + [(I_m \otimes K_{mm}) \cdot (\text{vec}(I_m) \otimes I_m)] \otimes I_m\} \tag{E.8}$$

Notez que (E.7) est asymptotiquement égal à

$$\text{vec}(\widehat{[M]}_{4*}) = (1+\omega)\text{vec}([N]_4) + O_p(n^{-1/2}) \tag{E.9}$$

Par conséquent, en définissant $G = \rho^{-1}\text{vec}(N_4)\text{vec}(N_4)^T$, avec $\rho = \text{vec}(N_4)^T\text{vec}(N_4)$, Il est possible d'affirmer que $G\text{vec}(\widehat{[M]}_{4*})$ est un estimateur cohérent de $[M_4]$ si et seulement si $[M_4]$ a la structure définie dans (E.4). Par conséquent, en supposant que ce dernier est vrai, il est de connaissance commune que

$$n^{1/2}v = n^{1/2}(I_{m^4} - G)\text{vec}(\widehat{[M]}_{4*}) \tag{E.10}$$

est asymptotiquement normale avec une moyenne nulle et une matrice de covariance

$$\Phi = (I_{m^4} - G)\Xi(I_{m^4} - G) \tag{E.11}$$

où Ξ désigne la matrice de covariance asymptotique de $n^{1/2}\text{vec}(\widehat{[M]}_{4*})$.

Le test de Wald pour les signaux à valeurs complexes indique que

$$T = nv^H\Gamma v \tag{E.12}$$

il y a une distribution asymptotique du chi carré avec des degrés de liberté f égal au rang de Φ si Γ est un estimateur cohérent d'un inverse généralisé de ce dernier. En d'autres termes, si les échantillons testés sont elliptiquement symétriques (hypothèse H_0), alors

$$T \to \chi^2_f \text{ in distribution} \tag{E.13}$$

Par conséquent, le test décrit dans (E.12) rejette H_0 lorsque T dépasse $\chi^2_{f,1-p}$, où p est souvent appelé niveau asymptotique et $1-p$ est la probabilité de fausse alarme.

Abordons ensuite la formulation de Ξ. Notez de (E.7) que Ξ peut être écrit comme

$$\Xi = [M]_C - (1+\omega)[M]_{C,A}H^H - (1+\omega)H[M]_{A,C} + (1+\omega)^2 H[M]_A H^H \tag{E.14}$$

où $[M]_C$ est la matrice de covariance de vec(C), $[M]_A$ est la matrice de covariance de vec(A), et $[M]_{Q,R}$ est la matrice de covariance croisée entre Q et R.

Notez de (E.14) que pour construire le test, il est nécessaire de dériver des matrices de moments de sixième et huitième ordre, ce qui pourrait considérablement accroître la complexité de l'ancien. Néanmoins, en supposant qu'ils existent tous les deux et que la structure momentanée de notre population est la même que celle d'une distribution elliptique jusqu'aux moments de huit ordres [90], puis $[M]_4 = (1+\omega)N_4$, $[M]_6 = (1+\eta)N_6$ et $[M_8] = (1+\theta)N_8$, avec η, θ et ω, apportent des fonctions du générateur de fonctions caractéristiques. En outre, il est possible d'écrire (voir (E.3))

$$[M]_C = (1+\theta)(1+\omega)^2(N_4^T \otimes N_4) + \theta(1+\omega)^2 \text{vec}(N_4)\text{vec}(N_4)^T \tag{E.15}$$

$$[M]_{C,A} = (1+\eta)\sum_i (e_i \otimes I_{m^3}) N_6 (e_i \otimes I_{m^2}) - (1+\omega)\text{vec}(N_4)\text{vec}(I_m)^T \tag{E.16}$$

où e_i est la ith ième colonne de la matrice d'identité I_m, et

$$[M]_A = (1+\omega)(I_m \otimes I_m) + \omega\left(\text{vec}(I_m)\text{vec}(I_m)^T\right) \tag{E.17}$$

Pour conclure la dérivation du test, le seul point manquant est de spécifier un estimateur cohérent de l'inverse généralisé de Φ. Notez que la spécification de $\hat{\omega}$, $\hat{\eta}$, $\hat{\theta}$ comme estimateurs cohérents de ω, η et θ, respectivement, est une condition suffisante pour atteindre cet objectif. Un estimateur cohérent de ω est derivée de (3.14)

$$\hat{\omega} = \frac{1}{nm(m+1)} \sum_{i=1}^{n} \left[k_i^H \widehat{[M]}^{-1} k_i \right]^2 \tag{E.18}$$

De façon analogue, on peut montrer que

$$\hat{\eta} = \frac{1}{nm(m+1)(m+2)} \sum_{i=1}^{n} \left[k_i^H \widehat{[M]}^{-1} k_i \right]^3 \tag{E.19}$$

et

$$\hat{\theta} = \frac{1}{nm(m+1)(m+2)(m+3)} \sum_{i=1}^{n} \left[k_i^H \widehat{[M]}^{-1} k_i \right]^4 \tag{E.20}$$

En résumé, le cadre proposé pour la symétrie elliptique complexe commence par l'estimation de (E.18), (E.19) et (E.20). Ensuite, (E.15), (E.16) et (E.17) sont calculés et

par conséquent, (E.14) est dérivé. Puis (E.11) est utilisé avec (E.10) dans (E.12) et le test est finalement terminé. Le degré de liberté du test est égal au rang de Φ [90] et est donné par (voir l'appendice C)

$$f = m^2 + \frac{m(m-1)(m^2+19m+6)}{24} - 1 \tag{E.21}$$

Notez que pour $m = 3$, (3.26) se réduit à $f = 26$.

E.9 Analyse du rendement

Afin d'accéder à la performance et à la robustesse du test propose, données simulées, les données de l'ensemble de données aéroportées de la bande P acquises par l'Office national d'études et de recherches aérospatiales (ONERA) sur la Guyane française en 2009 dans le cadre de la campagne de l'Agence spatiale européenne TropiSM et d'une image RAMSES X acquise sur Bretigny, France (voir l'appendice E) sont prises en considération.

E.9.1 Analyse des données synthétiques

Les données synthétiques utilisées dans la présente analyse sont divisées en 9 régions, chacune contenant 100 x 100 échantillons d'un type spécifique d'encombrement hétérogène. A l'exception du premier, supposé gaussien et le dernier supposé un modèle dépendant de la polarisation, tous les autres sont modélisés comme SIRVs (voir (**??**)), avec des paramètres différents. Puisque la fonction de densité de probabilité de la variable aléatoire de texture n'est pas spécifiée explicitement par le modèle, sans perte de généralité, nous avons généré l'ensemble de données synthétiques en supposant qu'il ait une distribution Gamma. Les paramètres de forme et d'échelle de distribution gamma qui caractérisent la variable aléatoire de texture pour chaque région sont tels que leur moyenne est fixe et fixée à 1 et leurs variances sont données comme dans la Figure E.5.

Une fois que la distribution Gamma est paramétrée pour chaque région c, un vecteur de texture simulé $\tilde{\boldsymbol{\tau}}^c$, $2 \leq c \leq 8$ est généré aléatoirement. Ensuite, on génère un vecteur aléatoire distribué normal complexe $\tilde{\mathbf{z}}$, c'est-à-dire, $\tilde{\mathbf{z}}^c \sim CN(\mathbf{0}, \mathbf{I})$. Enfin, le vecteur d'observation simulé pour chaque région est alors donné par

$$\tilde{\mathbf{k}}^c = [\mathbf{M}]^{\mathbf{1/2}} \sqrt{\tilde{\boldsymbol{\tau}}^c} \cdot \tilde{\mathbf{z}}^c \tag{E.22}$$

où $[M]$ est la matrice de covariance speckle, gardé le même pour toutes les régions et donné par

$$[M]^{1/2} = \begin{bmatrix} 0.2236 & 0 & 0.5477 \\ 0.2236 & 0.3873 & 0.5477j \\ 0 & -0.3873j & 0 \end{bmatrix} \tag{E.23}$$

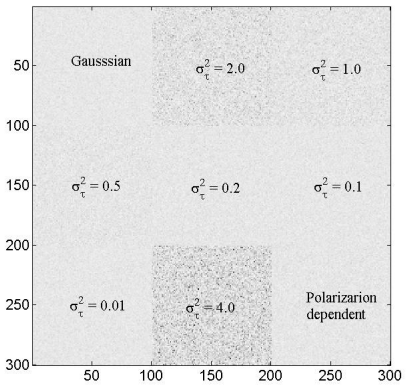

Figure E.5: Données synthétiques avec une indication de la variance de la distribution gamma qui caractérise la variable aléatoire de texture pour chaque région.

où $j = \sqrt{-1}$ est l'unité imaginaire. Selon [98] cette matrice de covariance décrit un encombrement hétérogène composé de 60% de quart d'onde, de 30% d'hélice à gauche et de 10% de dipôle, avec une entropie égale à 0.8.

Puisque les données synthétiques utilisées dans la présente étude sont composées de régions homogènes, une approche par fenêtre coulissante est suffisante pour la définition de l'ensemble des échantillons utilizes. Néanmoins, la taille de cette fenêtre coulissante peut avoir un impact direct sur la performance du test, soit si elle est sous-estimée ou surestimée. La figure E.6 présente en vert un surplot des points où le test indique des échantillons symétriques non sphériques avec la plage de données synthétiques comme arrière-plan pour différentes tailles de fenêtres coulissantes. Le niveau asymptotique p (voir (**??**)) a été fixé à 0.99.

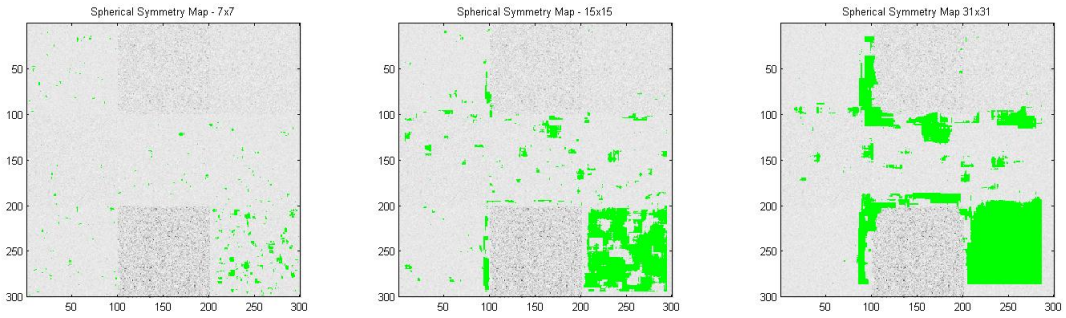

(a) (b) (c)

Figure E.6: Échantillons rejetés par le test proposé en vert sur fond d'onde de données synthétiques. Essai répété avec différentes tailles de fenêtre: (a) 7 x 7; (B) 15 x 15; (C) 31 x 31.

Notez que la performance de test proposée est extrêmement dépendante de la taille de la fenêtre. Il est évident dans la Figure E.6 que plus la taille de la fenêtre est élevée, meilleure est la probabilité de détection (vu dans l'efficacité du test en rejetant le modèle multiplicatif

pour les pixels dans la région "Polarisation Dépendante"). Néanmoins, la probabilité de fausse alarme peut être vue sous deux angles. D'une part, la quantité de fausses alarmes isolées (valeurs aberrantes) diminue à mesure que la taille de la fenêtre augmente, d'autre part, même si le nombre de pixels de fausses alarmes reste pratiquement le même, leur taille augmente avec une augmentation de la taille de la fenêtre. Ce dernier point à la dépendance de la performance d'essai sur le degré d'hétérogénéité dans l'ensemble des échantillons utilisés dans la dérivation des statistiques.

Par conséquent, il est possible de conclure que le test proposé a une très bonne performance dans la discrimination entre SIRV et non SIRV encombrement hétérogène, indiquant où le modèle de produit traditionnel (texture indépendante de polarisation) échoue. Néanmoins, en fonction du degré de non-stationnarité des échantillons utilisés dans le test, ça rejette le modèle aussi, ce qui peut être mieux vu dans les frontières de quelques régions sur le jeu de données. Il est important de souligner qu'il n'est pas obligatoire que, lorsque des échantillons de différents modèles SIRV sont utilisés pour extraire les statistiques, le test échouera, Si tel était le cas, toutes les frontières de l'ensemble de données synthétiques auraient des pixels défaillants et pourtant, seules les frontières de quelques régions présentent ce comportement.

La performance du test est également vérifiée en fonction du niveau de confiance p. De façon analogue, la Figure E.7 présente en vert un surplot des points où le test indique des échantillons symétriques non sphériques avec la plage de données synthétiques comme arrière-plan pour différents niveaux asymptotiques p. La taille de la fenêtre a été choisie pour être 23×23.

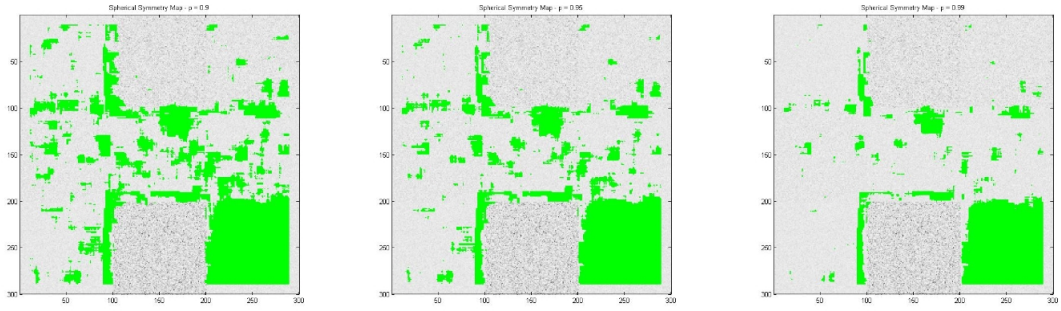

(a) (b) (c)

Figure E.7: Échantillons rejetés par le test proposé en vert sur fond d'onde de données synthétiques. Essai répété avec différentes niveaux asymptotiques p: (a) 90%; (b) 95%; (c) 99%.

Notez que la probabilité de détection, telle que définie ci-dessus, reste pratiquement inchangée, tandis que la probabilité de fausse alarme augmente considérablement à mesure que le niveau asymptotique diminue. Par souci d'exhaustivité, nous vérifions la cohérence du test en fonction de la taille de la fenêtre. La Figure E.8 montre la distribution chi-carré ajustée à l'histogramme de l'essai effectué (voir (E.12)), utilisant l'approche par fenêtre coulissante (tailles de fenêtres 7×7, 15×15 et 23×23) et en tenant compte de la région où les pixels

présentent une distribution Gamma avec une variance $\sigma_\tau^2 = 0.5$.

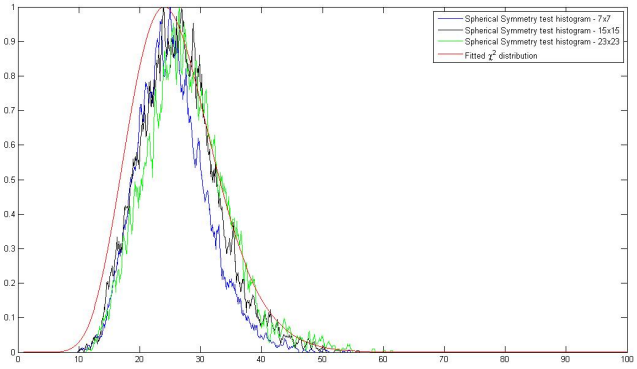

Figure E.8: Distribution chi-carrée ajustée (rouge) à l'histogramme du test effectué avec différentes tailles de fenêtre : 7×7 (bleu), 15×15 (noir) et 23×23 (vert). Il a été pris en compte la région avec distribution gamma et variance $\sigma_\tau^2 = 0.5$.

Notez de la figure E.8 que la distribution du chi-carré avec des degrés de liberté donnés par (3.26) fournit un bon ajustement pour le test de symétrie sphérique présenté dans (E.12) pour les tailles de fenêtres 15×15 et 23×23, conformément à la théorie décrite dans la section précédente. Néanmoins, l'ajustement n'est pas bien vérifiée pour les tailles de fenêtres faibles, ce qui peut être vu dans la courbe correspondant à une taille de fenêtre 7×7. Cela met en évidence une autre indication de la dépendance des performances d'essai à la taille de la fenêtre.

E.9.2 Analyse de données réel

Une fois que le test est validé avec des données synthétiques, nous avons poursuivi notre enquête en utilisant des données réelles. Plus précisément, dans le présent travail, nous prenons en considération les données de la bande P dataset aéroporté par acquis l'Office National d'Etudes et de Recherches A'erospatiales (ONERA) sur la Guyane française en 2009 dans le cadre de la campagne de l'Agence spatiale européenne Tropisar, caractérisant une zone principalement composée par des cibles distribuées.

La taille de la fenêtre coulissante a ensuite été choisi pour être 15×15, qui a présenté une bonne performance en ce qui concerne la probabilité de détection et la probabilité de fausse alerte et est conforme à ce qui est décrit comme nécessaire par d'autres auteurs lors de l'application de nombreux algorithmes SAR [58, 65, 82].

Comme un outil supplémentaire pour le reste de l'analyse, l'algorithme de classification statistique est encore employé pour segmenter la scène à l'étude en 8 classes différentes. À cette fin, le classificateur statistique développé pour les données POLSAR fortement texturées [41] a été utilisé. Contrairement à la classification classique H/α non surveillée [18], le fouillis

hétérogène non gaussien est pris en compte.

Abordons d'abord le jeu de données Tropisar. La figure E.9 présente la région à l'étude de la zone concernée (différente de l'utilisation dans l'analyse temporelle en raison de son plus grande hétérogénéité), La sortie de l'algorithme de classification et la carte de symétrie sphérique où, en vert, sont indiqués des échantillons symétriques non sphériques en arrière-plan par l'étendue du jeu de données.

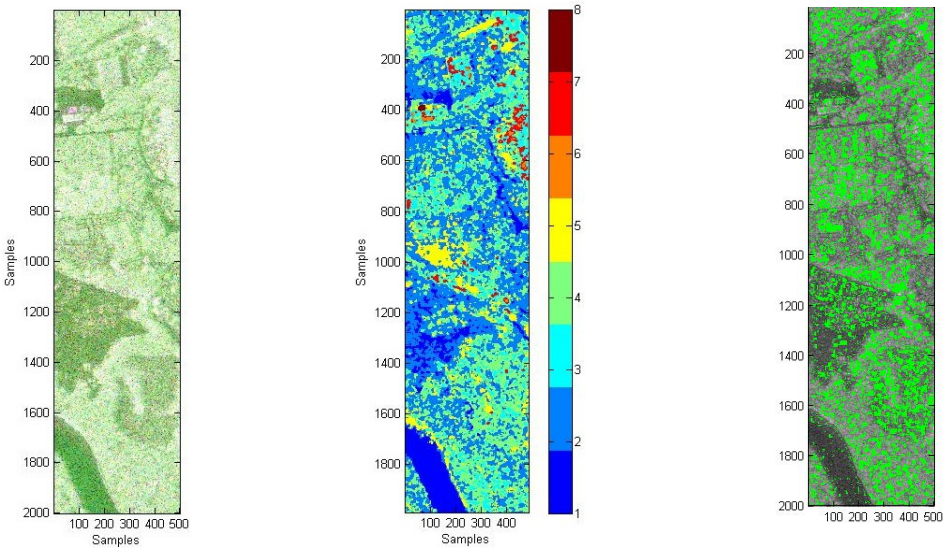

Figure E.9: Guyane française à l'étude: (a) Image RGB, Rouge (HH + VV), Vert (HV), Bleu (HH-VV); (B) sortie de l'algorithme de classification statistique; (C) carte de symétrie sphérique.

Notez que la rivière constitue la classe 1, ainsi que certaines zones présumées flottantes alors que la classe 8 est principalement représentée par une petite région probablement avec une certaine structure faite par l'homme. En utilisant un espace de fonctions H/α (Figure E.10), il est possible de percevoir le haut degré d'hétérogénéité dans les données qui contient des pixels qui peuvent être classés comme Volume, Double-Bounce et Type de surface de scatters [19].

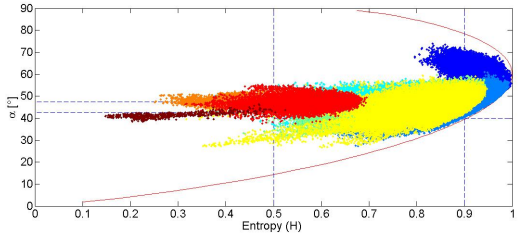

Figure E.10: Guyane française à l'étude: H/α espace de fonctionnalité.

Notez que l'incidence des pixels rejetés dans ce type d'ensemble de données n'est pas négligeable (30%). Cela indique qu'une partie considérable des données ne correspond pas

au modèle vectoriel aléatoire invariant sphérique (modèle de produit). De plus, il faut noter que le test permet d'identifier correctement les régions à indice élevé de non-stationnarité, plus accentuées entre les classes, comme on peut le voir clairement dans ce qui semble être le rivage. Les intervalles [200: 300, 200: 300] et [400: 500, 400: 600] de l'ensemble de données, tous deux composés de pixels de plusieurs classes différentes, présentent également une forte concentration d'échantillons qui échouent au test et ne correspondent donc pas au modèle du produit. Le pourcentage de pixels rejetés pour chaque classe est donné dans le tableau E.1.

Table E.1: Pourcentage de pixels symétriques non sphériques par classe dans la Guyane française à l'étude.

Class	**Percentage of non spherical symmetric pixels**
1	13.76%
2	25.46%
3	45.30%
4	33.20%
5	32.19%
6	30.99%
7	48.76%
8	55.12%

Notez que les classes 3, 7 et 8 ne sont pas de très bons représentants du modèle de produit, tandis que d'autre part, les classes 1, 2, 4, 5 et 6 sont bien décrites comme SIRVs. Une étude plus poussée des données a révélé que la plupart des pixels déclarés non sphériques symétriques par le test proposé (98,62%) avaient leur statistique dérivée d'un ensemble d'échantillons contenant des pixels de différentes classes, plus précisément, 3 (38,79%) ou 4 (30,51%) classes. Cela indique l'importance de considérer la haute hétérogénéité des données, spécialement dans des scénarios forestiers, dans la dérivation d'algorithmes de traitement d'image SAR. Ce dernier devient critique si une approche par fenêtre coulissante est directement adoptée sans étape supplémentaire pour éviter la contamination de pixel avec des caractéristiques différentes, compromettre le modèle statistique considéré bon d'ajustement.

Une partie considérable de données hétérogènes élevées peut ne pas correspondre au modèle vectoriel aléatoire invariant sphérique (modèle de produit). Par conséquent, les algorithmes traditionnels de détection et de classification développés à partir de ces derniers deviennent sub-optimaux lorsqu'ils sont appliqués dans ce type de régions, en mettant en évidence la nécessité de mettre à jour le modèle pour associer une variable de texture individuelle à chaque canal polarimétrique [35], ou le développement d'algorithmes indépendants du modèle, comme l'Analyse de composantes indépendantes (ICA), proposée dans [3].

Le premier, introduit un haut degré de complexité dans la modélisation des données PolSAR et, par conséquent, en dérivant des algorithmes adaptés à ces modèles. En outre, fournir des modèles uniques lorsque l'hypothèse multi-texture est pris en considération est un défi très difficile à trouver. L'ICA, d'autre part, étant une technique de séparation de sources aveugles, basée sur des moments statistiques d'ordre supérieur, vise à récupérer des sources

statistiques indépendantes sans avoir aucun fond physique du processus de mélange [48]. Par conséquent, il s'agit d'une stratégie indépendante de modèle pour analyser le comportement des clones hétérogènes non gaussiens (inhérents aux systèmes SAR à haute résolution) qui s'est avérée très utile et introduit une autre manière d'interpréter physiquement une image SAR polarimétrique. Dans la section suivante, cette technique est traitée plus en détail.

E.10 ICTD basée sur ICA - Aspects théoriques

Dans le contexte de la décomposition de la cible incohérente de PolSAR, de nombreux procédés ont été proposés dans la littérature pour décomposer un pixel d'image (composé de dispersions distribuées) en vecteurs de base et récupérer correctement des informations quantitatives (paramétrisation). En ce qui concerne ces derniers, les paramètres de Cloude et Pottier (entropie, alpha et anisotropie) [19] et le modèle de vecteur de diffusion cible de Touzi [98] sont les plus employés, dont l'utilité a déjà été démontrée par plusieurs auteurs. Concernant le premier, l'évaluation des propriétés statistiques des données PolSAR (dérivée à l'aide de pixels voisins) est un facteur clé pour dériver les mécanismes de diffusion moyenne ou dominante dans une cellule de résolution composée de cibles stochastiques distribuées.

Le Eigenvector basée sur ICTD parvient à décomposer un pixel d'image dans les trois dispersions les plus dominantes à partir de la matrice de cohérence moyenne. En outre, il a une propriété intrinsèque que les dispersions dérivées sont orthogonales et non corrélées, ce qui pour les cloches gaussiennes signifie également l'indépendance. L'inconvénient de ce type de méthode émerge lorsque l'encombrement n'est pas gaussien ou n'est pas composé par des mécanismes orthogonaux, des situations où la performance de l'algorithme pourrait être compromise.

L'Analyse de Composants Indépendants, étant un algorithme indépendant modèle, est décrit comme une alternative potentielle pour les données PolSAR très hétérogènes. Cette méthode est brièvement résumée en trois étapes principales: la sélection des données, basée sur la classification statistique de l'image POLSAR; estimation des composantes indépendantes et paramétrage des vecteurs cibles dérivés. Comme indiqué dans [3], l'inconvénient majeur de la méthode proposée est la taille de l'ensemble de données d'observation, qui doit être un peu plus grand que la taille de la fenêtre coulissante utilisée dans les méthodes bien établies. Cette contrainte a conduit les auteurs dans [3] à utiliser un algorithme de classification non supervisé plutôt que de s'appuyer sur une très grande fenêtre coulissante, compromettant l'efficacité de la méthode.

L'utilisation d'un algorithme de classification limite la performance du méthode dans le sens où l'image est segmentée en un nombre défini a priori de classes de tailles variables, ce qui peut compromettre l'estimation des paramètres des vecteurs cibles et, par conséquent, l'interprétation correcte des dispersions présentes dans la zone à l'étude. L'emploi d'un algorithme de classification introduit quelques implications. Par exemple, une classe peut contenir plus d'échantillons qu'il n'en a besoin pour une estimation correcte des paramètres de la cible, ce qui signifie que la résolution spatiale, fortement dégradée par l'utilisation de cette approche,

est pire qu'elle ne pourrait l'être. D'autre part, si une classe ne contient pas suffisamment d'échantillons, les paramètres estimés peuvent présenter une grande variance, indiquant que les valeurs dérivées ne sont pas toujours conformes à la vérité au sol.

Dans ce contexte, on utilise dans la présente section une approche de simulation Monte Carlo pour évaluer la taille optimale d'une fenêtre coulissante pour différents supports, les simples composés de diffractomètres de base tels que l'hélice, le dipôle, le dièdre et le trièdre et les plus complexes comme Surface, Double rebond et retour de volume. Un algorithme de classification non supervisé est utilisé pour identifier dans une image RAMSES X-band acquise sur Br'etigny, France (voir Appendice E), ensembles d'échantillons caractérisant les mécanismes de diffusion moyenne, de surface, de double rebond et de volume. La matrice de mélange et la matrice de covariance pour chacun des types de diffraction complexes susmentionnés sont estimées à l'aide d'algorithmes appropriés (algorithme ICA non-circulaire complexe et algorithme de point fixe [104], respectivement) et utilisé pour bootstrap échantillons aléatoires pour la simulation Monte Carlo approche. Il est important de souligner que, comme indiqué dans [3], la matrice de mélange et la matrice de covariance sont potentiellement différentes, donc l'ensemble des échantillons aléatoires utilisés dans l'analyse de décomposition ICA et Eigenvector ne sont pas les mêmes. En ce qui concerne l'analyse avec les dispersions de base, les paramètres précités sont définis manuellement.

Dans le présent travail, l'encombrement hétérogène est décrit par une variante du modèle SIRV (Spherically Invariant Random Vectors) [104], en supposant une texture dépendant de la polarisation, caractérisée par un vecteur aléatoire. Analogiquement à ce qui a été fait aux matrices de mélange et de covariance, les paramètres de distribution de texture, pour chacun des types de dispersions complexes susmentionnés, sont estimés à partir de l'ensemble de données réels alors que pour les diffusions de base, ils sont définis manuellement.

E.11 Approche de simulation Monte Carlo

Les auteurs de [3] ont prouvé l'utilité de l'Analyse de Composante Indépendante dans ICTD par son emploi en données réelles, laissant quelques questions ouvertes comme la performance de l'algorithme sous une implémentation de fenêtres coulissantes et sous un encombrement contenant des scénarios de composants gaussiens. Dans le présent travail, une approche de simulation Monte Carlo est réalisée afin de compléter les résultats obtenus dans [3] et d'établir empiriquement un contexte théorique qui permettra une utilisation plus efficace de l'ICA dans d'autres applications de PolSAR.

E.11.1 Estimation de la taille optimale des fenêtres coulissantes

L'encombrement hétérogène est décrit ici par une variation du modèle SIRV (Spherically Invariant Random Vectors), avec une matrice de covariance normalisée et une texture dépendant de la polarization. On suppose différentes hypothèses quant à sa composition: les diffractions

de base (orthogonales et non orthogonales) représentant les mécanismes de diffusion moyenne ou dominante dans la cellule d'imagerie et les dispersions complexes (surface, double rebond et volume).

Chaque procédure de simulation, pour une taille de fenêtre et un type d'encombrement donnés, est répétée 1000 fois et les paramètres estimés sont alors moyennés. Pour le premier ensemble de simulations, les mécanismes de diffusion moyenne ou dominante dans la cellule d'imagerie sont considérés comme des dispersions de base et deux scénarios sont établis: l'un contenant des cibles orthogonales et l'autre contenant des mécanismes non orthogonaux. La forme de distribution gamma et les paramètres d'échelle qui caractérisent la texture sont fixés et fixés à 1.95 et 0.51, respectivement. Ils sont utilisés pour générer un vecteur de texture simulé $\tilde{\boldsymbol{\tau}}^c$. Ensuite, on génère un vecteur aléatoire distribué normal complexe $\tilde{\mathbf{z}}$, c'est-à-dire, $\tilde{\mathbf{z}} \sim CN(\mathbf{0}, \mathbf{I})$. Enfin, le vecteur d'observation simulé pour chaque classe est alors donné, analogue à (E.22), par

$$\tilde{\mathbf{x}}^c = \mathbf{A}\sqrt{\tilde{\boldsymbol{\tau}}^c} \cdot \tilde{\mathbf{z}} \tag{E.24}$$

L'ensemble de données simulées (E.24) est ensuite utilisé comme entrée pour la décomposition de vecteur propre et la décomposition ICA.

Nous allons d'abord étudier le comportement de décomposition de vecteur propre, ci-après également désigné sous le nom de PCA (Analyse de Composants Principaux) pour simplifier et ICA sous l'hypothèse que l'encombrement hétérogène est composé par des cibles orthogonales. Il est important de souligner que des précautions particulières doivent être prises dans le choix approprié des mécanismes de diffusion simulés, puisque Touzi TSVM présente des ambiguités pour certains scatters spécifiques, comme indiqué à l'appendice D. Dans la présente analyse, la composition d'encombrement est de 60% d'hélice à gauche, 30% d'hélice à droite et 10% de trièdre. L'entropie d'un tel encombrement est de 0.8 alors que les paramètres invariants de Touzi sont affichés dans le tableau E.2.

Table E.2: Mécanismes orthogonaux - Paramètres de Touzi

	τ_m [°]	α_s [°]	ϕ_{α_s} [°]
Helix left screw	45	45	0
Helix right screw	−45	45	0
Trihedral	0	0	0

La Figure E.11 présente les paramètres estimés de l'invariant du rouleau de Touzi et l'entropie obtenue en utilisant la décomposition ICA et Eigenvector. Il est à noter que la décomposition en Eigenvector, telle qu'anticipée par [58], et ICA dérivent correctement les paramètres de Touzi correspondant aux trois composantes ainsi que l'entropie. La troisième composante est plus problématique à la fois pour la décomposition, présentant un taux de convergence plus faible. En ce qui concerne l'Entropie et les première et deuxième composantes, le comportement de la décomposition d'Eigenvector et de l'ICA sont très similaires, et la même taille de fenêtre peut être utilisée pour les deux.

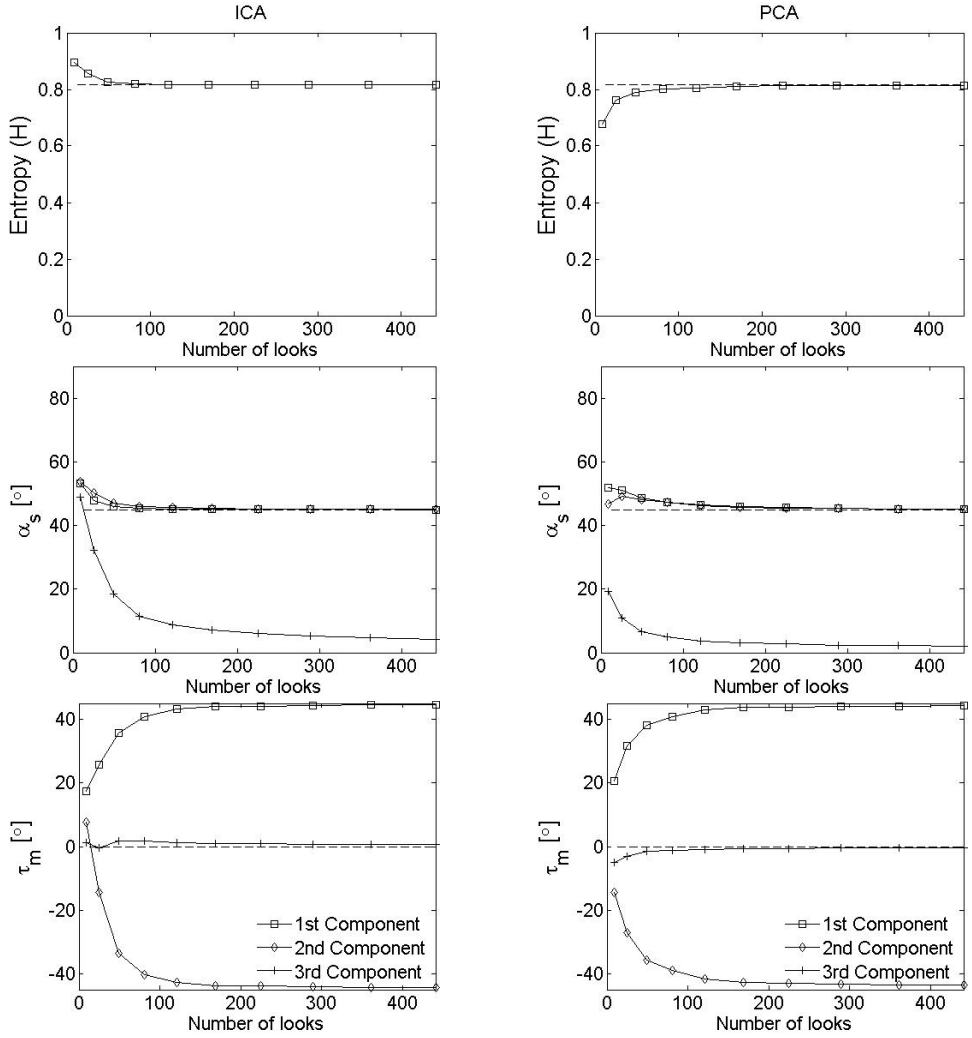

Figure E.11: Paramètres de TSVM d'entropie et de Touzi dérivés de la décomposition polarimétrique ICA et Eigenvector cible, PCA, pour un encombrement composé de mécanismes orthogonaux de base.

Le choix de la taille des fenêtres coulissantes est une préoccupation constante dans la communauté SAR puisque les valeurs élevées diminuent considérablement la résolution spatiale du système et que des valeurs basses peuvent éventuellement introduire un biais dans l'estimation de quelques paramètres. De nombreux auteurs ont soulevé la question de savoir quelle serait la taille de fenêtre optimale pour plusieurs applications différentes, p. Ex [58, 65]. Notez dans la Figure E.11 qu'une taille de fenêtre 11×11 fournit une bonne estimation des premier et second composants des paramètres TSVM ainsi que l'entropie à biais négligeable, ce qui représente un bon choix en termes de compromis de performance.

Ensuite, un scénario avec des cibles non orthogonales est abordé. L'encombrement est alors composé de 60% de vis hélicoidale gauche, 30% de dipôle et 10% de dièdre. Comme prévu, puisque la décomposition de vecteur propre a une contrainte intrinsèque que les composantes

estimées sont mutuellement orthogonales, il est incapable de dériver correctement la matrice de mélange initiale, en omettant d'estimer le contenu de l'encombrement hétérogène. D'autre part, ICA n'est pas contraint à l'orthogonalité donc il réussit à estimer les trois composantes paramètres.

Passons maintenant à des types plus complexes de cibles, composées soit de surface, Double-Bounce ou de volume. La première étape de la procédure de simulation consiste à définir le jeu d'observations à partir duquel la matrice de covariance, la matrice de mélange et les paramètres de texture seront estimés pour chacun des mécanismes susmentionnés. Un algorithme de classification non supervisé développé pour les données POLSAR hautement texturées [42] est utilisé pour identifier au sein d'une image de bande X RAMSES acquise sur Br'etigny, France (voir appendice E), ensembles d'échantillons caractérisant les mécanismes de diffusion moyenne, de surface, de double rebond et de volume. Plus de détails sur l'algorithme de classification sont fournis dans la section suivante, où il est supposé un rôle plus crucial dans l'analyse. Même si elle a déjà été démontrée tout au long de cette thèse, dans un souci d'exhaustivité, la Figure E.12 présente la zone référencée en rouge (HH + VV), Vert (HV) et Bleu (HH-VV), la sortie de l'algorithme de classification et un espace caractéristique H/α.

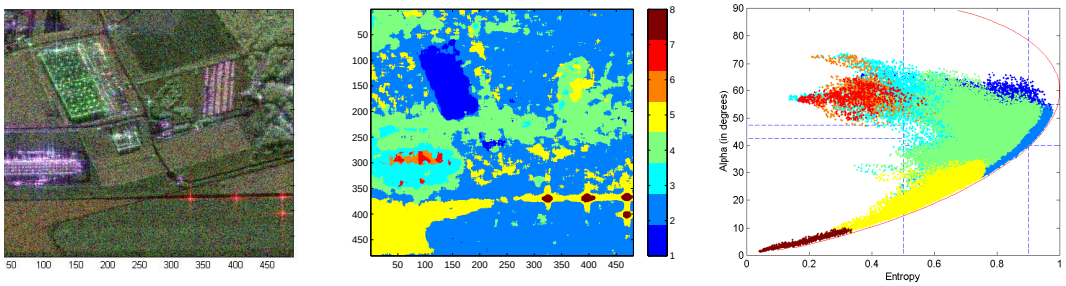

(a) (b) (c)

Figure E.12: Région de Br'etigny à l'étude: (a) image RGB, Rouge (HH + VV), Verte (HV), Bleu (HH-VV); (b) sortie de l'algorithme de classification statistique; (c) H/α espace de fonctionnalité.

En analysant l'espace des traits H/α on peut conclure que la classe 1 est principalement composée de dispersions de volume, la classe 5 est principalement composée de surface et la classe 6 est principalement composée de diffractures double rebond. Par conséquent, des échantillons correspondant à chaque classe ont été extraits de l'ensemble visé et la matrice de mélange, $\hat{\mathbf{A}}^c$, et matrice de covariance, $[\hat{M}]^c_{FP}$, ont été estimées pour chacune des classes décrites ($c = 1, 2, 3$) de mécanismes. Un algorithme décrit dans [24], initialisé avec la matrice identité, est utilisé pour ce dernier. Ensuite, la texture est également estimée pour chaque vecteur d'observation correspondant à l'une des trois classes précitées (surface, double rebond et volume).

En estimant le paramètre de texture pour chaque pixel, on obtient un ensemble de réalisations à partir desquelles il est possible de retrouver ses paramètres de distribution. Puisque la fonction de densité de probabilité du vecteur aléatoire de texture n'est pas spécifiée

explicitement par le modèle, ainsi que dans l'ensemble précédent de simulations, nous analyserons les paramètres de convergence en supposant qu'il ait une distribution Gamma. Les paramètres de la distribution sont ensuite extraits de la $\hat{\tau}_i^c$ déjà estimée et utilisés pour générer des vecteurs de texture simulés à des échantillons aléatoires bootstrap pour l'approche de simulation Monte Carlo. Les étapes restantes de la génération de données simulées sont les mêmes que celles décrites précédemment. Il est important de souligner que, comme indiqué dans [3], la matrice de mixage et la matrice de covariance sont potentiellement différentes, l'ensemble des échantillons aléatoires utilisés dans l'analyse de décomposition ICA et Eigenvector ne sont pas identiques.

La Figure E.13 présente les résultats de la décomposition polarimétrique en utilisant à la fois la décomposition ICA et Eigenvector (PCA). Notez que, malgré le faible taux de convergence de ϕ_{α_s} pour le type de surface de dispersion, le comportement de taux de convergence atteint à la fois par ICA et PCA sont pratiquement les mêmes que ceux obtenus dans les simulations avec des dispersions de base que les mécanismes de diffusion moyenne ou dominante. Cette conclusion conduit à la possibilité d'utiliser la même taille de fenêtre que celle rapportée précédemment de 11×11 échantillons.

E.12 ICTD basée sur ICA - Aspects pratiques

Réduire l'écart théorique impliquant l'ICA basée sur ICTD, permet une augmentation considérable de son utilisation. Néanmoins, puisqu'il s'agit d'une approche ICTD récemment introduite pour l'analyse d'images PolSAR, Il est encore difficile d'affirmer s'il existe des scénarios spécifiques où la performance de l'ICA est supérieure à celle de l'APC (ETIC basée sur un Eigenvector). Alternativement, nous pensons que les informations supplémentaires introduites par l'ICA peuvent être combinées avec les informations fournies par la décomposition des vecteurs propres afin de mieux proposer, parmi d'autres, algorithmes de classification et d'inversion de paramètres géophysiques. Dans ce contexte, la présente section, en plus de détails, les résultats obtenus lorsque l'ICA basée sur l'ICCTD est réalisée sur des jeux de données variés, en les comparant aux informations fournies par l'approche Eigenvector.

E.13 Cloude et Pottier H/α analyse de l'espace des fonctions

L'analyse de Cloud et Pottier H/α caractérise l'espace résultat lors de l'ICTD basée ICA est d'abord considérée une image RAMSES X-band acquis sur Bretigny, en France. L'augmentation des possibilités H/α pairs a provoqué le ICA basé sur ICTD peut être explorée de plusieurs aspects. Dans le présent travail, nous concentrons notre investigation en pixels qui tombent dans la région 3 dans le plan H/α. Dans ce but, nous abordons d'abord les résultats d'un algorithme de classification non supervisé développé pour les données POLSAR fortement texturées [42] afin d'identifier les pixels qui basculent entre les classes initialement affectées aux régions 6 et 2 lorsque l'approche Eigenvector est appliquée.

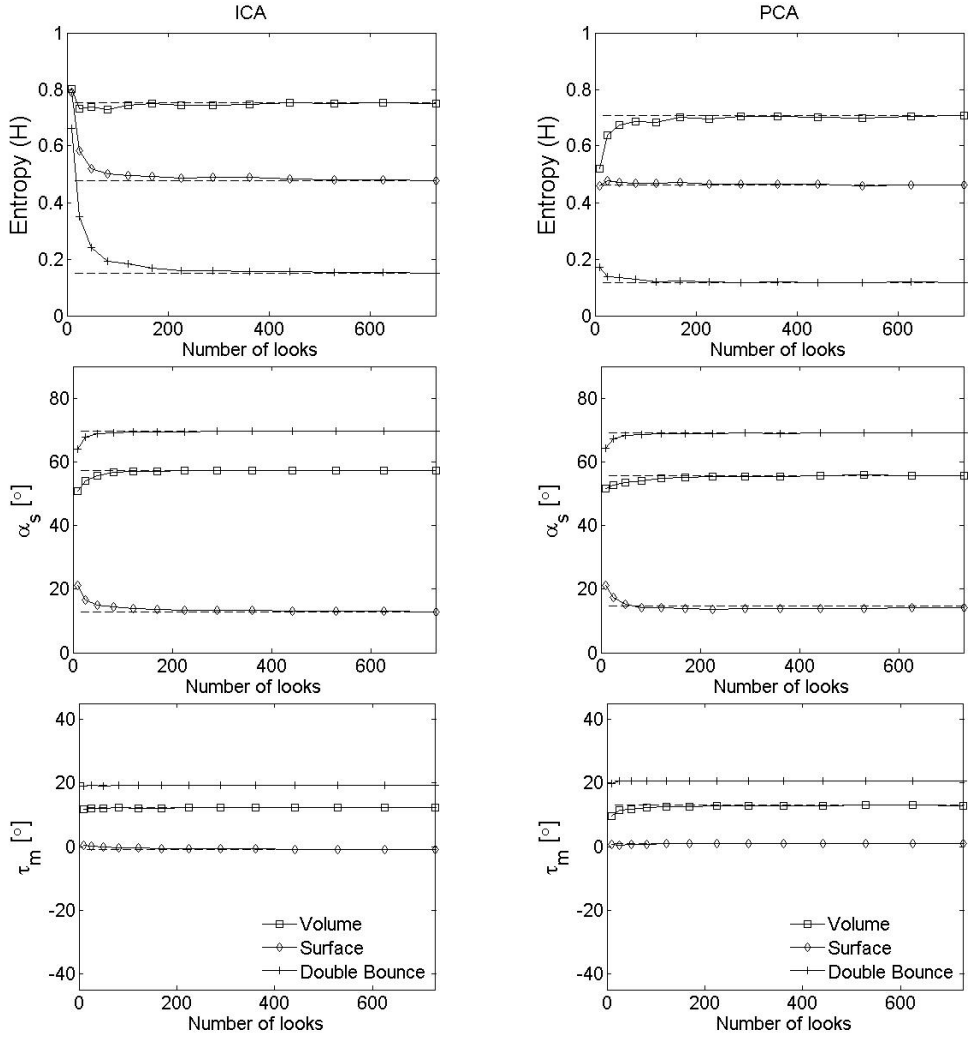

Figure E.13: Paramètres TSVM d'entropie et de Touzi dérivés avec la décomposition polarimétrique de la cible ICA et Eigenvector, PCA, pour un type d'encombrement complexe: surface, double-rebond et volume.

La méthode susmentionnée repose sur un test statistique sur les matrices de covariance estimées pour chaque pixel en considérant ses voisins dans une fenêtre coulissante. Une mesure de distance, dérivée basée sur le modèle probabiliste de données adopté, est utilisée pour vérifier à quelle classe correspond un pixel donné. La mesure de distance utilisée dans le présent travail suppose que l'encombrement hétérogène est décrit par le modèle Spherically Invariant Random Vectors (SIRV), avec une matrice de covariance normalisée.

La première étape avant l'emploi de l'algorithme de classification est d'évaluer la conformité des données par rapport au modèle statistique considéré. Comme conclu précédemment, seule une petite partie des pixels de la zone étudiée échoue au test (18%), indiquant que le modèle SIRV est un bon représentant du comportement stochastique des données. L'algorithme de classification est ensuite brièvement décrit en 4 étapes: génération de la pop-

ulation initiale basée sur la classification H/α, où les pixels correspondant à la même région forment un cluster unique; calculer chaque centre de cluster; calculer la distance mesurée entre chaque pixel et tous les centres de cluster; associer le pixel à la grappe correspondant à la plus petite distance dérivée à l'étape précédente.

La nature adaptative de l'algorithme de classification cherche à grouper des pixels ayant un comportement statistique similaire, dans une tentative de mieux regrouper des phénomènes physiques similaires. La grande quantité de pixels qui basculent entre les classes prouve que la classification H/α ne parvient pas à expliquer pleinement certains types de mécanismes de diffusion. La figure E.14 présente la sortie H/α de classification initiale, l'algorithme de classification statistique sorti après 4 itérations et les espaces de fonction H/α correspondant.

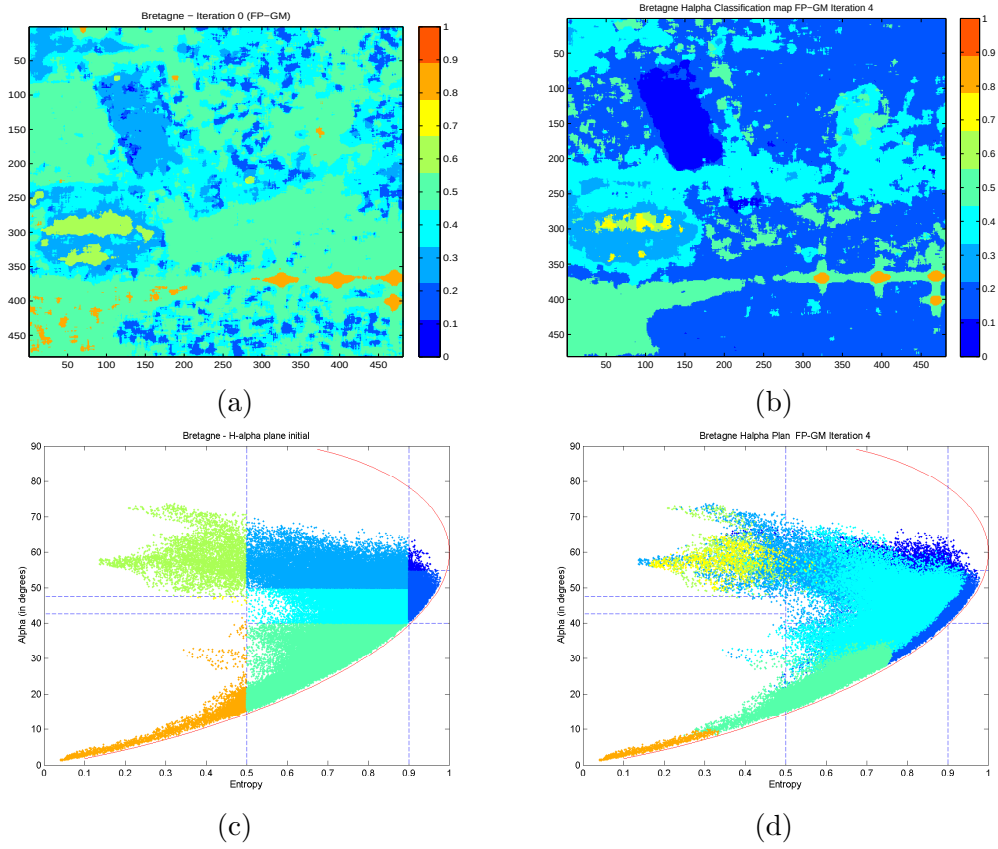

Figure E.14: Superficie de Br'etigny à l'étude: (a) H/α production de la classification; (b) Sortie de l'algorithme de classification statistique, 4e itération; (c) H/α espace de caractéristique initial; (d) H/α espace de caractéristique après la 4e itération.

Examinons maintenant les évidences que les limitations inhérentes à l'approche des vecteurs propres dans l'espace des traits H/α peuvent compromettre l'interprétation correcte de l'image SAR. Dans le présent travail, nous nous concentrons sur l 'analyse de pixels dont le comportement polarimétrique se situe dans les régions 2,3 et 6. Selon les auteurs de [19], la région 6 représente une dispersion de surface d'entropie moyenne. En comparaison avec le comportement attendu des mécanismes de surface, il est indiqué que l'augmentation

de l'entropie peut être liée soit à une augmentation de la rugosité de la surface, soit à des effets de propagation de la canopée. Si l'entropie augmente encore et l'intervalle de α est resté inchangé, les pixels tombent dans la région 3 et seront classés comme une surface d'entropie élevée. Néanmoins, en raison de la contrainte mathématique, aucun mécanisme de diffusion ne peut être identifié comme appartenant à cette région. Enfin, la région 2, signifie une dispersion de la végétation d'entropie élevée, y compris le type de volume de scatters. Le comportement naturel des couvertures des forêts et de certains types de surfaces végétalisées avec des éléments de diffusion aléatoire hautement anisotropes peut tomber dans cette région [19]. Notez que les phénoménologies physiques représentées par la région 6 et la région 2 sont très différentes. Par conséquent, il devrait être très peu douteux pour déterminer si un pixel est mieux représenté par la région 6 ou par la région 2. Néanmoins, la quantité totale de pixels qui basculent entre les régions 6 et 2 représente 62,36% de l'ensemble initialement classé dans la région 6.

Maintenant, nous allons aborder les nouvelles informations fournies par l'ICA basée ICTD. Une comparaison avec la classification H/α en prenant en considération l'ICA basée sur ICTD (représentée sur la figure 6.4) indique qu'un pourcentage élevé des pixels qui basculent entre les classes initialement affectées aux régions 6 et 2 sont classés comme appartenant à la région 3. Plus précisément, 69,23%. Furthermore, only 10% of the pixels classified in region 3 where not originally classified in region 6 when the Eigenvector approach was employed. Ces résultats indiquent que le comportement physique des pixels de commutation est mieux représenté par la région 3, diffusion de surface à entropie élevée, ce qui est inviable lorsque l'approche d'Eigenvector est utilisée.

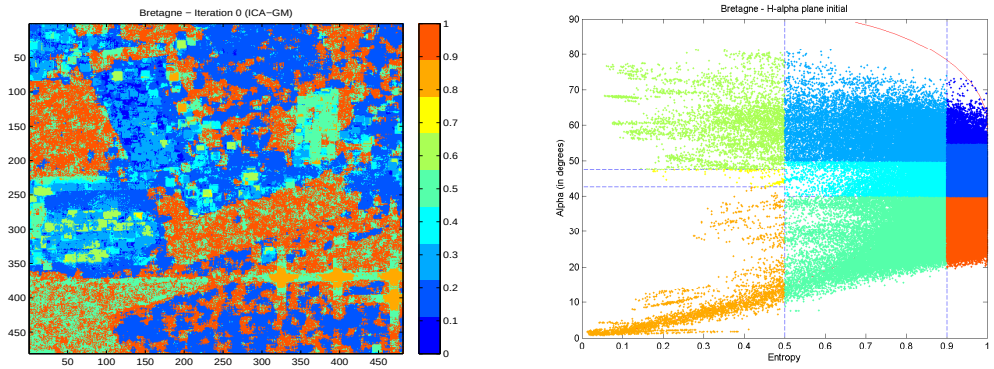

(a) (b)

Figure E.15: (a) H/α sortie de classification, (b) H/α espace de caractéristique.

Un bon indicateur de la robustesse des nouvelles informations fournies par l'ICA basée sur l' ICTD par rapport à l'espace des fonctionnalités H/α est le taux de fausses alertes qu'il fournit. Un scénario de forêt tropicale est pris en considération pour vérifier si les pixels sont incorrectement classés comme appartenant à la région 3 lorsque leur phénoménologie naturelle indique clairement qu'ils devraient être représentés par la région 2. Les données de l'ensemble de données aéroportées de la bande P acquises par l'Office National d'Etudes et de Recherches Aérospatiales (ONERA) sur la Guyane en 2009 dans le cadre de la campagne

de l'Agence spatiale européenne TropiSAR sont abordées.

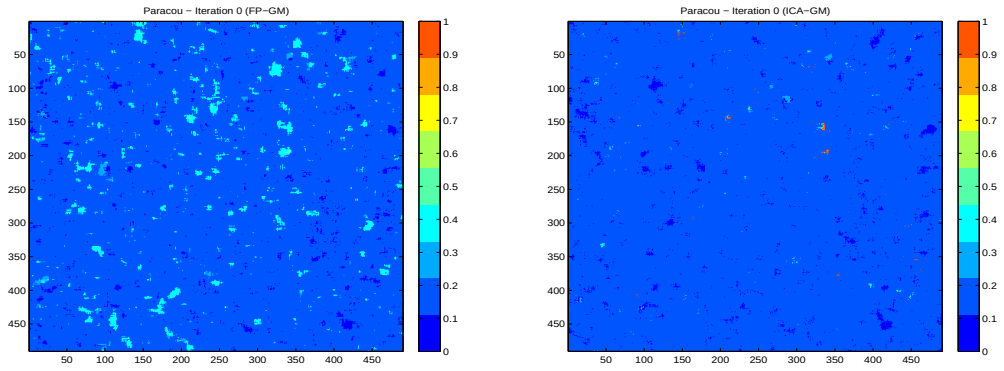

(a) (b)

Figure E.16: Guyane française à l'étude: (a) H/α production de classification lorsque l'approche Eigenvector est employée et (b) H/α classification lorsque l'ICA basée sur ICTD est prise en considération.

Notez dans la Figure E.16 que l'ICA associe correctement la plus grande partie du comportement physique des forêts tropicales à la région 2, les dispersions de volume, comme prévu, compte tenu de l'effet des couvertures forestières. Néanmoins, les entropies estimées sont plus élevées par rapport à l'approche Eigenvector.

Enfin, nous concluons l 'étude des nouvelles informations fournies par l' ACI en ce qui concerne l 'espace des fonctions en analysant les résultats d' une utilisation combinée de l'ICA basée sur l'ICTD et de l 'algorithme de classification statistique décrit. L'ICA peut être utilisée comme population initiale, compte tenu de la sortie de classification H/α résultant de l'ICA basée sur ICTD. Dans [42] les auteurs indiquent que la population initiale n'affecte pas la production de la classification, en présentant une comparaison des résultats obtenus lorsque la classification Eigenvector H/α est utilisée à cette fin et lorsqu'une population aléatoire est employée. Néanmoins, l'introduction d'une nouvelle classe de mécanismes, représentée par la région 3 dans le plan H/α peut en effet influencer le résultat de l'algorithme de classification. Il est important de souligner qu'aucune autre modification n'est nécessaire dans cette approche. Comme les données sont essentiellement composées d'échantillons SIRV, et nous vérifions la ressemblance statistique entre les pixels en fonction de leurs matrices de covariance, la mesure de distance employée jusqu'ici peut être maintenue inchangée, ainsi que le reste du code.

Examinons maintenant les résultats en tenant compte de l'ensemble de données POLSAR acquises en octobre 2006 par le système E-SAR sur la partie supérieure du glacier Tacul du site d'essai "Chamonix-Mont-Blanc", France. La figureE.17 présente la zone référencée en rouge (HH + VV), Vert (HV) et Bleu (HH-VV) et la sortie du test de symétrie sphérique où en vert sont représentés des pixels symétriques non sphériques.

Notez que seule une petite partie des pixels de la zone étudiée échoue au test (29%), ce qui indique que le modèle SIRV est également un bon représentant de ce comportement stochastique de jeu de données. La figure E.18 présente la sortie H/α de classification initiale

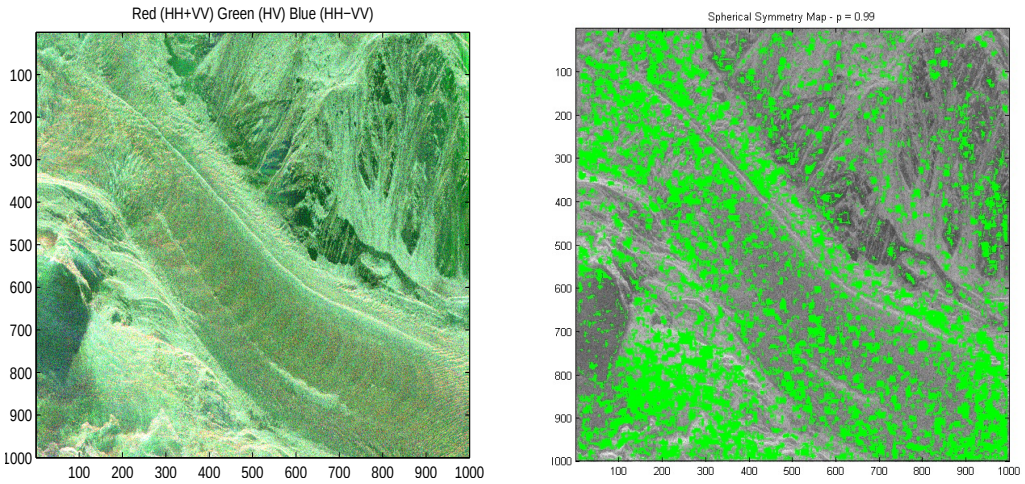

(a) (b)

Figure E.17: Superficie du glacier du Tacul à l'étude: (a) Image RVB, rouge (HH + VV), verte (HV), bleue (HH-VV); (b) Carte de symétrie sphérique.

pour l'approche Eigenvector et l'ICA basée sur ICTD, l'algorithme de classification statistique délivré après 4 itérations. La figure E.19 présente le corresponant H/α.

Notez que la région 3 caractérise principalement les pixels qui représentent les bandes incurvées en raison des phénomènes de "bandes de Forbes" [54, 100], une caractéristique périodique provoquée par un déplacement périodique récurrent du glacier Tacul au cours d'une année. La bande de Forbes peut être identifiée sur la figure 6.8 comme la succession d'ondulations qui balaie transversalement la région détectée. Initialement définie en 1842 par le Prof. Forbes, en tant que bandes de saleté, les courbes pointant vers le bas le glacier sont principalement composés par l'accumulation de roches et de saleté qui tombent sur la glace, surtout pendant l'été. Ces impuretés affectent la taille des grains et les caractéristiques de cristallinité de la glace dans sa composition (par exemple, elles empêchent la formation de grands cristaux non perturbés). Par conséquent, son identification / caractérisation correcte est extrêmement pertinente dans l'analyse de la glace glaciaire.

Dans [54], les auteurs ont interprété les mécanismes de diffusion correspondants comme une rétrodiffusion de surface dominante avec de faibles entropie et des angles alpha. Ceci est conforme à ce qui est représenté à la 6.8 (voir également la figure 6.9). Néanmoins, notez qu'une partie considérable de pixels dans cette zone correspond à la classe 4 qui n'explique pas théoriquement le phénomène physique. L'approche ICA, d'autre part, indique que la région susmentionnée est initialement mieux caractérisée par une signature de rétrodiffusion de surface d'entropie élevée, ce qui est inviable dans un Eigenvector basée sur l'ICTD utilisant la paramétrisation de Cloude et Pottier. Alors que les angles alpha typiques estimés à l'aide des deux méthodes sont à peu près les mêmes, l'entropie dérivée avec ICA est plus élevée et l'existence de pixels caractérisés comme appartenant à la classe 4 est négligeable. Si aucun algorithme de classification n'a été utilisé, il serait déjà possible de caractériser les bandes sales et d'estimer les paramètres géophysiques qui les concernent, en prenant en considération

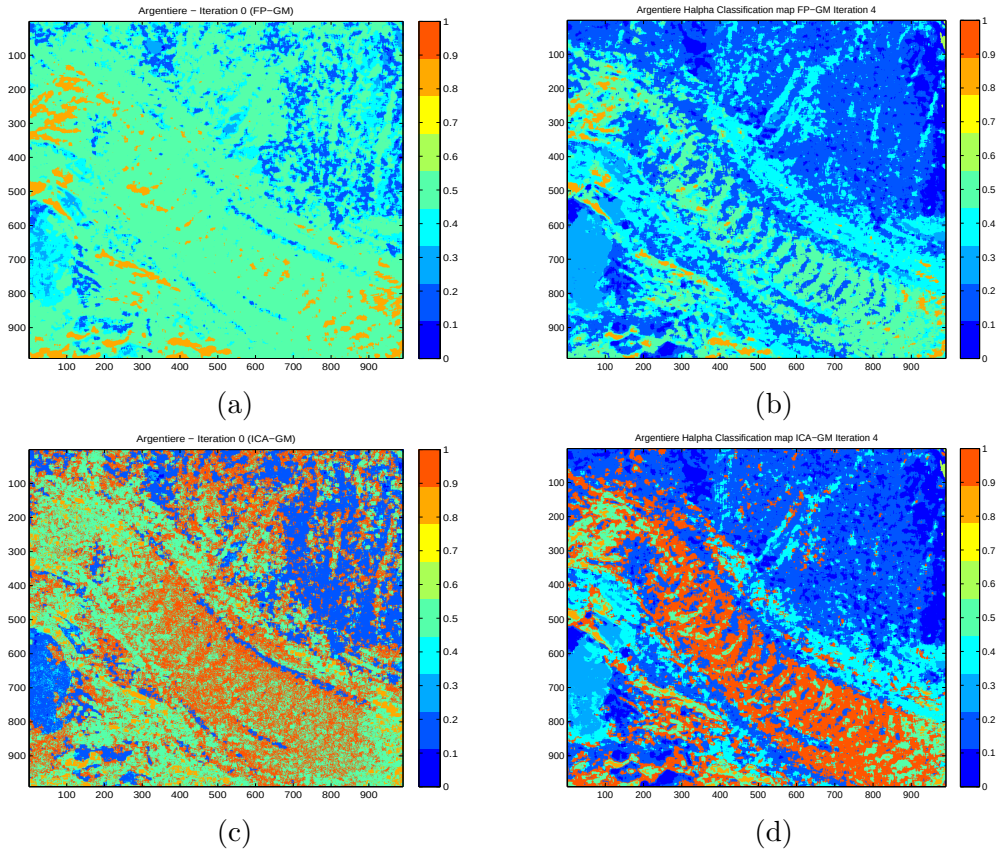

Figure E.18: Superficie du glacier du Tacul à l'étude: (a) H/α sortie de la classification Eigenvector approche ; (b) Sortie de l'algorithme de classification statistique, 4ème itération Eigenvector approche ; (c) H/α sortie de classification ICA basée sur ICTD ; (d) Sortie de l'algorithme de classification statistique, 4ème itération ICA basée sur l'ICTD.

uniquement la population initiale dérivée de l'ICA basée sur l'ICTD (en utilisant une approche par fenêtre coulissante).

Entre autres améliorations, la sortie de la classification statistique délimite clairement les régions susmentionnées, augmentant la capacité de mieux les caractériser. En outre, il est à noter que le comportement attendu des bandes de salissures lorsqu'elles s'approchent des fonds, est respecté dans l'approche ICA, c'est-à-dire, ils sont réduits comme le glacier descend jusqu'à disparaître, ce qui peut être observé par la plus grande quantité de pixels classés en classe 5 (surface d'entropie moyenne) dans le fond du glacier.

Enfin, il est intéressant de noter que les bandes de neige, sont également classées soit à l'aide de l'approche ICA ou de l'ICTD traditionnel basé sur un Eigenvector. Les mécanismes dominants des zones entourant les bandes de salissure, où la glace est plus propre, sont correctement identifiés comme une combinaison de mécanismes de surface et de volume (région 2 dans l'espace de caractéristique H/α), probablement due à une pénétration partielle de la surface de la glace dans la bande L [54]. Notez, encore une fois, que la transition entre les

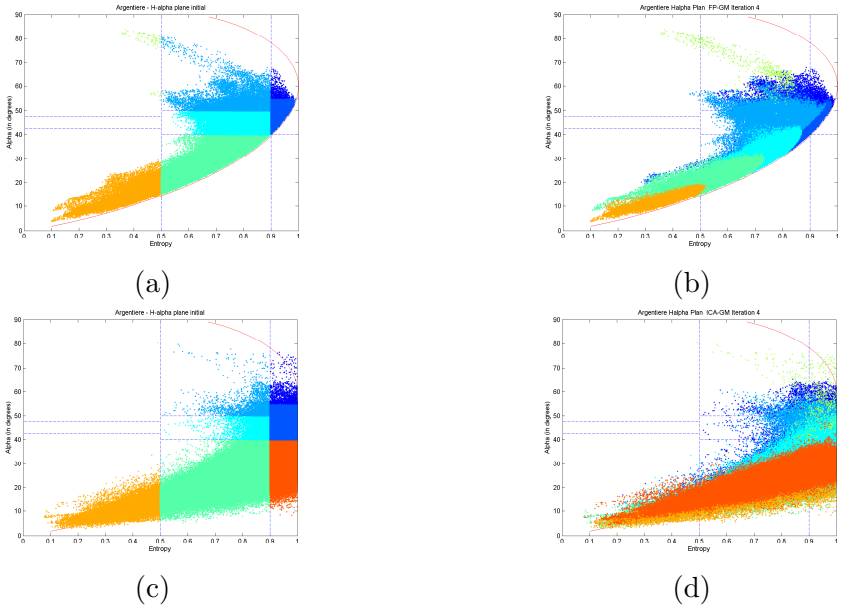

(a) (b)

(c) (d)

Figure E.19: Superficie du glacier de Tacul à l'étude: (a) H/α espace de caractéristique initial Eigenvector approche ; (b) H/α espace de caractéristique après la 4ème itération Eigenvector approche; (c) H/α espace caractéristique initial ICA basée sur ICA ; (d) H/α espace de caractéristique après la 4ème itération ICA basée ICTD.

deux régions (la saleté et la neige) est intuitivement mieux représentée par la région 3 dans l'espace caractéristique H/α, comme l'indique l'approche ICA basée sur ICTD.

La caractérisation des paramètres de la neige basée sur l'analyse des données SAR est une recherche active au sein de la communauté scientifique [68, 101, 28, 63]. La rétrodiffusion de la couche de neige peut contenir des contributions provenant de quatre mécanismes différents: la composante de la surface de la neige, la composante du volume de la neige, la composante de la surface du sol sous-jacente et la composante d'interaction du volume du sol. La signature polarimétrique complexe d'une telle cible est une fonction à la fois des paramètres du capteur d'imagerie (par exemple la fréquence et l'angle d'incidence) ainsi que des caractéristiques géophysiques de la neige (par exemple densité de neige et profondeur de neige). De nombreux auteurs ont abordé l'inversion des paramètres de la neige et la dérivation des modèles de neige sur la base du comportement des ensembles de données PolSAR acquis, en particulier dans les régions montagneuses. Récemment, l'entropie dérivée de un Eigenvector basée sur l'ICTD a été associée de façon prometteuse à la profondeur de neige sèche [28]. Les auteurs ont signalé que les petits paquets de neige sèche (par rapport à la fin de la saison hivernale) entraînaient une augmentation de l'entropie. La variation du comportement physique du mécanisme de diffusion de neige est liée à la réduction de la croûte de glace, qui représente principalement une forte diffusion de surface, entraînant une augmentation de la surface de la neige et des composantes de rétrodiffusion du volume. Comme nous l'avons souligné tout au long du présent ouvrage, principalement au chapitre 4), les cibles de type entropie élevée peuvent être interprétées de manière incorrecte lorsque un Eigenvector basée sur l'ICTD est utilisée. Par conséquent, l'approche ICA proposée apparaît comme un outil prometteur dans

l'étude de ces mécanismes de diffusion.

E.14 Conclusion

Dans le présent travail, plusieurs aspects de l 'analyse de l' encombrement PolSAR hautement hétérogène (inhérents aux systèmes SAR de polarimétrie haute résolution) ont été abordés. Premièrement, on a vérifié la validité du modèle de produit (SIRV) utilisé pour caractériser les données multivariées de PolSAR. Un nouveau cadre méthodologique pour évaluer la conformité du modèle de données multivarié à haute résolution PolSAR en termes de statistiques asymptotiques a été dérivé. Des hypothèses statistiques testant la structure de la matrice de quadricovariance ont été effectuées afin d'étudier si des échantillons d'une région homogène constituent un ensemble de données symétriques elliptiques, ce dernier étant vrai si le modèle susmentionné est valide. Des simulations avec des données synthétiques et une analyse détaillée des données réelles ont été effectuées.

L'analyse avec les données synthétiques affirme pour l'efficacité et la cohérence du test proposé dérivé, montrant que celui-ci est capable d'identifier correctement les régions dont les échantillons ne présentent pas de symétrie elliptique et, par conséquent, ne correspondent pas au modèle Spherically Invariant Vector. La performance du test a été vérifiée pour différents niveaux de confiance et de taille des fenêtres, indiquant l'importance de hoosing correctement ces paramètres pour des résultats meilleurs et non biaisés. Enfin, on a vérifié que selon l'hypothèse SIRV, la sortie d'essai est conforme aux régions rejetées attendues, composées d'échantillons présentant des indices élevés de non-stationnarité (frontières), en dehors des valeurs aberrantes.

Ensuite, l'étude du résultat du test avec des ensembles de données variés (voir figures (3.7) et (3.9)) a montré que le taux de pixels rejetés n'est pas négligeable dans des types de scénarios spécifiques. La zone forestière étudiée ici présentait 30% de pixels qui ne correspondent pas au modèle du produit. Même si l'absence de vérité au sol précise peut limiter l'assertion de ce qui provoque l'échec du modèle de produit, L'objectif principal de la présente analyse était de montrer que, en démontrant l'exactitude du test (au moyen d'une dérivation mathématique détaillée et d'une analyse avec un ensemble de données synthétiques) et en l'appliquant à des jeux de données réels avec différentes caractéristiques de détecteur, nous pourrions être en mesure d'indiquer que la quantité de pixels qui échouent le modèle peut être non négligeable, nécessitant une attention supplémentaire dans leur analyse.

Par conséquent, les algorithmes traditionnels de détection et de classification développés à partir de ces derniers deviennent sub-optimaux lorsqu'ils sont appliqués dans ce type de regions, en mettant en évidence la nécessité de mettre à jour le modèle à celui qui associe une variable de texture individuelle à chaque canal polarimétrique [35], ou le développement d'algorithmes indépendants du modèle, tels que l'Independent Component Analysis (ICA), proposé dans [3].

L'ICA étant une technique de séparation de source aveugle, basé sur des instants statis-

tiques d'ordre supérieur, vise à récupérer des sources statistiques indépendantes sans avoir aucun fond physique du processus de mélange [48]. Par conséquent, il s'agit d'une stratégie indépendante de modèle pour analyser le comportement des clones hétérogènes non gaussiens (inhérents aux systèmes SAR à haute résolution) qui s'est avérée très utile et introduit une autre manière d'interpréter physiquement une image SAR polarimétrique.

Dans le présent travail, nous nous sommes également concentrés sur l'adressage et la quantification des deux principaux inconvénients de l'emploi de l'Analyse de Composants Indépendants dans la décomposition polarimétrique cible: La quantité plus élevée d'échantillons nécessaires et l'hypothèse de l'encombrement non gaussien. Sur la base de données simulées nous avons réussi à mieux étudier les concepts théoriques et quantifier le biais sur l'entropie et les paramètres de Touzi causés par un nombre insuffisant d'échantillons utilisés dans leur estimation.

Il a été montré que lorsque les mécanismes de diffusion moyenne ou la plus dominante qui caractérisent l'encombrement hétérogène sont orthogonaux, Les paramètres de Touzi estimés à l'aide de l'ICA sont les mêmes que ceux estimés à l'aide de la décomposition des vecteurs propres et le taux de convergence de l'estimation est presque le même. Lorsque l'encombrement est composé par des mécanismes non orthogonaux, contrairement à la décomposition des Eigenvectors, ICA réussit à dériver les mécanismes de diffusion de base sans compromettre ses performances.

Simulations avec des types complexes de dispersion, Volume, Double-Bounce et Surface, dont la caractéristique a été extraite de données réelles, hétérogène avec des sources gaussiennes et avec corrélation spatiale a montré des résultats similaires, Ce qui donne force à la proposition d'utiliser une fenêtre coulissante de 11×11 dans l'approche ICA fondée sur ICTD.

Réduire l'écart théorique impliquant les ICA basées sur ICTD, permet une augmentation considérable de son utilisation. Dans ce contexte, on a vérifié les nouvelles informations potentielles fournies par l'ICA basée sur l'ICTD en termes de Cloude et Pottier H/α feature space. Une analyse théorique des courbes limites décrite dans [19], qui génèrent des régions non réalisables dans le plan précité, montrent qu'elles résultent de la contrainte d'orthogonalité inhérente aux Eigenvectors de la matrice de cohérence, Qui sont associés aux dispersions les plus dominantes présentes dans le pixel analysé. Puisque l'ICA basée sur l'ICTD n'introduit pas de telles contraintes, des exemples de compositions d'encombrement possibles avec des mécanismes non orthogonaux qui ne font pas partie des régions réalisables d'Eigenvector ont été abordés.

Une analyse détaillée avec des données réelles a révélé une propriété intéressante de ICTD basée sur ICA qui est inégalable par l'approche d'Eigenvector: la capacité de classer des cibles correspondant à la zone 9 dans l'espace de caractéristiques susmentionné. Performances ICA a également été vérifiée en vertu des scénarios boisées indiquant éparpillements moyennes similaires à l'approche Eigenvector, mais plutôt des mécanismes de diffusion supplémentaires lorsque Touzi TSVM a été pris en considération. Enfin, le présent travail a présenté un nouveau cadre pour l'application des techniques du SRS avec les données POLinSAR pour l'optimisation de la cohérence polarimétrique et l'estimation des phases interférométriques as-

sociées. Les résultats obtenus montrent des améliorations en termes de cohérences optimisées dérivées et, dans le même temps, ils restent cohérents avec la vérité au sol réelle.

La principale mise en garde liée à ICA est que, depuis qu'il a été récemment introduit comme une approche ICTD à l'analyse d'image SAR, Il est encore difficile d'affirmer s'il existe des scénarios spécifiques où la performance ICA est plus élevée que celle d'Eigenvector. Alternativement, les auteurs estiment que les informations supplémentaires introduites par l'ICA peuvent être combinées avec les informations fournies par la décomposition des vecteurs propres afin de mieux proposer, Entre autres, algorithmes de classification et d'inversion de paramètres géophysiques.

Enfin, en tant que sous-produit de ce travail, des expressions de forme fermée pour les quatrième et sixième moments d'ordre du vecteur aléatoire réparti complexe normal ont été dérivées et étendues à des distributions symétriques elliptiques complexes, avec des estimateurs cohérents.